

STUDY OF OPTOELECTRONIC PROPERTIES OF THIN FILM SOLAR CELL
MATERIALS $\text{Cu}_2\text{ZnSn}(\text{S},\text{Se})_4$ USING MULTIPLE CORRELATIVE SPATIALLY-
RESOLVED SPECTROSCOPY TECHNIQUES

by

Qiong Chen

A dissertation submitted to the faculty of
The University of North Carolina at Charlotte
in partial fulfillment of the requirements
for the degree of Doctor of Philosophy in
Electrical Engineering

Charlotte

2015

Approved by:

Dr. Yong Zhang

Dr. Abasifreke Ebong

Dr. Edward B. Stokes

Dr. Michael G. Walter

©2015
Qiong Chen
ALL RIGHTS RESERVED

ABSTRACT

QIONG CHEN. Study of optoelectronic properties of thin film solar cell materials $\text{Cu}_2\text{ZnSn}(\text{S},\text{Se})_4$ using multiple correlative spatially-resolved spectroscopy techniques.
(Under the direction of DR. YONG ZHANG)

Containing only earth abundant and environmental friendly elements, quaternary compounds $\text{Cu}_2\text{ZnSnS}_4$ (CZTS) and $\text{Cu}_2\text{ZnSnSe}_4$ (CZTSe) are considered as promising absorber materials for thin film solar cells. The best record efficiency for this type of thin film solar cell is now 12.6%. As a promising photovoltaic (PV) material, the electrical and optical properties of CZTS(Se) have not been well studied.

In this work, an effort has been made to understand the optoelectronic and structural properties, in particular the spatial variations, of CZTS(Se) materials and devices by correlating multiple spatially resolved characterization techniques with sub-micron resolution. Micro-Raman (μ -Raman) spectroscopy was used to analyze the chemistry compositions in CZTS(Se) film; Micro-Photoluminescence (μ -PL) was used to determine the band gap and possible defects. Micro-Laser-Beam-Induced-Current (μ -LBIC) was used to examine the photo-response of CZTS(Se) solar cell in different illumination conditions. Micro-reflectance was used to estimate the reflectance loss. And Micro-I-V measurement was used to compare important electrical parameters from CZTS(Se) solar cells with different device structure or absorber compositions. Scanning electron microscopy and atomic force microscopy were used to characterize the surface morphology. Successfully integrating and correlating these techniques was first demonstrated during the course of this work in our laboratory, and this level of integration and correlation has been rare in the field of PV research. This effort is significant not only for this particular project and

also for a wide range of research topics. Applying this approach, in conjunction with high-temperature and high-excitation-power optical spectroscopy, we have been able to reveal the microscopic scale variations among samples and devices that appeared to be very similar from macroscopic material and device characterizations, and thus serve as a very powerful tool to understand the underlying microscopic material structures and predict the potential of improvement in device performance.

First, by using an array of correlated aforementioned techniques, microscale inhomogeneity of the CdS layer thickness was found in CZTSe solar cells. Thicker CdS regions are found to cause more light-reflection loss thus yielding lower external quantum efficiencies (EQEs) than the general area. However, these regions show much less efficiency degradation at high illumination density, leading to an inversion of LBIC contrast between the CdS rich regions and general area. By improving the CdS layer uniformity, CZTSe device performance can be significantly boosted. And this finding also points out the possibility of operating thin-film photovoltaic device based on similar materials under substantially higher illumination density for concentrated photovoltaic and photo-detection. Second, Micro-Raman reveals multiple secondary phases such as ZnSe and SnSe within the CZTSe films, which are harmful for solar cell operation. In high-laser-power Raman study, CZTSe shows structural change and decomposition, which indicates poor thermal conductivity of the polycrystalline film. Different behaviors of CZTSe films prepared by different methods are observed in high-laser-power and high-temperature Raman studies, both of which offer effective approaches to examine microscopic structural variation of nominally similar CZTSe films. Because of the achieved high spatial resolution, applying μ -Raman and μ -LBIC, we are able to examine the depth variation of

the thin absorber film (in the order of 1 μm) in terms of chemical composition, photo-response, and deposition method dependence. In the third part, μ -I-V curves offer direct measurements of electrical parameters reflecting the effects of the device structure, absorber thickness and elemental ratio on the CZTSe cell performance. NaF precursor, low copper and high zinc content are demonstrated necessary for high performance CZTSe devices. However, one cell with higher copper and lower zinc content experiences slower EQE droop at high power density and part of the film shows better thermal conductivity, which suggests that the CdS/CZTSe heterojunction band alignment depends on the elemental ratio of the CZTSe film and CZTSe may have a potential in concentrated PV application if the elemental ratio can be optimized.

ACKNOWLEDGMENTS

First of all, I would like to express my deepest gratitude to my advisor, Prof. Yong Zhang, for continuous guidance and support during my Ph.D study. His knowledge and enthusiasm has inspired me to keep moving forward. Discussions with him have enlightened me with valuable aspects to my work. His affection for me will always be remembered.

I would like to thank my committee members, Profs. Abasifreke Ebong, Edward Stokes and Michael Walter, for their time and constructive comments to my dissertation.

I am also grateful to Dr. Ingrid Repins (NREL), Dr. Louis Grenet (CEA, LITEN, France), and Dr. Sergio Bernadi (CEA, LITEN, France) for generously offering me multiple samples used in this work, Dr. David Mitzi (IBM) for providing the very first CZTS device, and Dr. Suhuai Wei (NREL) for helpful discussions.

I have enjoyed working together with my current and previous labmates, Henan Liu, Liqin Su, Jason Marmon, Dr. Jianwei Wang, Dr. Naili Yue, Dr. Fengxiang Chen and Dr. Da Li. I feel lucky to have the opportunity to work with such friendly and thoughtful people. Productive discussions with them and their assistance in Raman and LBIC measurement have always been amazing help all the time.

I am thankful to Dr. Lou Deguzman, Dr. Rober Hudgins, Dr. Wattaka Sitaputra and John Hudak for clean room and instrument training.

My study at UNCC was supported by the GASP tuition award from UNCC Graduate School. I am thankful for the teaching assistantship provided by the Department of Electrical Engineering at UNCC and research assistantship offered by Prof. Yong Zhang's Material Research Laboratory.

I thank many of my close friends for their great accompany. I also take this opportunity to express my heartiest gratitude to my beloved parents and grandmother. All these would be impossible without them. I am indebted to my cousin, who has been taking care of them when I am away. Last, but certainly not least, I would like to thank my husband for his unconditional love. He has always been cheering me up, helping me to overcome my personal hurdles, and standing by me through the good times and bad.

TABLE OF CONTENTS

LIST OF FIGURES	x
CHAPTER 1: INTRODUCTION	1
1.1. Overview of Thin Film Solar Cell	1
1.2. $\text{Cu}_2\text{ZnSnS}_4$ and $\text{Cu}_2\text{ZnSnSe}_4$ Thin Film	4
1.3. Structure of CZTS(Se) Devices	11
1.4. Fabrication of CZTS(Se) Absorber	13
1.5. Samples Used in This Study	19
1.6. Summary	21
CHAPTER 2: SPATIALLY RESOLVED TECHNIQUES	23
2.1. Micro-Raman and Photoluminescence Spectroscopy	23
2.2. Laser-Beam-Induced-Current	28
2.3. Other Electrical and Optical Techniques	34
2.4. Summary	38
CHAPTER 3: ILLUMINATION DENSITY DEPENDENCE OF LBIC AND THE EFFECTS OF CdS LAYER THICKNESS	40
3.1. Introduction	40
3.2. PL and Raman Characterization of CZTS and CZTSe	43
3.3. CdS Rich Regions on CZTSe Devices	46
3.4. LBIC Contrast Reversal with Varying Illumination Density	51
3.5. Summary	61
CHAPTER 4: RAMAN STUDIES OF THE CZTSE SAMPLES PREPARED BY DIFFERENT METHODS	64
4.1. Introduction	64
4.2. Raman Studies of CZTSe Samples From Front Surface	67
4.3. Raman Studies of CZTSe Sample From Cleaved Edge	81
4.4. High Temperature Studies of CZTSe Samples	91

4.5. High Laser Power Illumination Effect on LBIC Current and Cleaved Edge LBIC Mapping	102
4.6. Summary	109
CHAPTER 5: LBIC STUDY OF CZTSE CELLS WITH DIFFERENT DEVICE STRUCTURE AND ELEMENTAL RATIOS IN ABSORBER	112
5.1. Introduction	112
5.2. I-V Curves of Different CZTSe Solar Cells	113
5.3. LBIC Comparison of Different CZTSe Solar Cells	117
5.4. Summary	130
CHAPTER 6: CONCLUSIONS AND OUTLOOK	132
REFERENCES	137

LIST OF FIGURES

FIGURE 1.1: Reported time line of solar cell energy conversion efficiencies [6].	2
FIGURE 1.2: Abundance of the chemical elements in Earth's upper continental [18].	5
FIGURE 1.3: Crystal structures of CZTS [29].	7
FIGURE 1.4: Calculated defect formation energy as a function of the Fermi energy at the thermodynamic chemical-potential point for CZTS and CZTSe. (Only the most stable charge state is plotted for each value of the Fermi energy) [55].	9
FIGURE 1.5: Schematic of the CZTSSe solar cell.	12
FIGURE 2.1: Energy-level diagram and relative location in frequency of Rayleigh, Stokes and anti-Stokes scattering.	24
FIGURE 2.2: Energy diagram of PL.	26
FIGURE 2.3: Schematic diagram of Raman system (simplified).	28
FIGURE 2.4: Schematic of electronic system to measure LBIC.	29
FIGURE 2.5: External quantum efficiency of a silicon solar cell [137].	33
FIGURE 2.6: Two types of reflection.	35
FIGURE 2.7: Microscope with high NA captures both specular and diffuse reflection.	35
FIGURE 2.8: I-V curve of a silicon solar cell.	36
FIGURE 2.9: Single diode model of a solar cell [138].	37
FIGURE 3.1: Two types of schematic energy band diagrams of window/CIGS structure [150].	41
FIGURE 3.2: Estimated band gap of three CZTS sample using absorption spectra.	45
FIGURE 3.3: PL spectrum of CZTS sample FSS 18 using Horiba system at room temperature.	45
FIGURE 3.4: Raman spectra of CZTS and CZTSe measured with 532 nm laser at $\sim 179 \mu\text{W}$.	46
FIGURE 3.5: Raman spectra from bright spot, dark spot and general spot of three CZTSe samples.	48
FIGURE 3.6: PL spectra from three types of spots on M3599_23 surface.	49

FIGURE 3.7: 2-Dimensional imaging and mapping result measured from M3599_23 device surface.	51
FIGURE 3.8: Reflectance and LBIC mapping with 532 nm laser at low and high power levels for CZTSe device M3599_23.	53
FIGURE 3.9: Reflectance and LBIC mapping with 633 nm laser at low and high power levels for CZTSe device M3599_23.	55
FIGURE 3.10: I-V curves of three types of regions with 532 nm laser at low and high power levels.	57
FIGURE 3.11: Corrected IV curves from three types of spots.	58
FIGURE 3.12: LBIC mapping with different 532 nm laser power levels obtained from M3602_22.	59
FIGURE 3.13: LBIC mapping with different 532 nm laser power levels obtained from a CIGS cell.	60
FIGURE 3.14: I-V curves of bright and general spot from a CIGS device with 532 nm laser at high power level.	61
FIGURE 4.1: (a) Calculated polyhedron of the chemical potential region where CZTS is stable against formation of four elements and six competitive compounds. (b) At $\mu_{\text{Cu}} = -0.2$ eV, SnS (green line), ZnS (blue line), CuS (red line), and Cu_2SnS_3 (navy line) defines the allowed chemical potential region (black). Point P locates the region where all intrinsic defects have positive formation energies. [54]	65
FIGURE 4.2: Pseudo-ternary phase diagram showing a very small central area where CZTS forms (marked as 1). [57]	65
FIGURE 4.3: Raman spectra of bare CZTSe film samples measured from front surface at 32.8 μW and 146 μW .	67
FIGURE 4.4: Raman spectra of three CZTSe samples measured from the front surface.	69
FIGURE 4.5: Raman spectra of three CZTSe samples after tested spots being illuminated by 2.47 mW.	71
FIGURE 4.6: Raman spectra of three CZTSe samples after tested spots being illuminated by 4.5 mW.	72
FIGURE 4.7: Si Raman spectra before and after high power illumination.	74
FIGURE 4.8: CZTSe_97 Raman mapping after one spot being illuminated by 2.47 mW for 100 s.	76
FIGURE 4.9: M3599_12 Raman mapping after one spot being illuminated by 2.47 mW for 100 s.	76

FIGURE 4.10: M3602_21 Raman mapping after one spot being illuminated by 2.47 mW for 100 s.	76
FIGURE 4.11: CZTSe_97 Raman mapping after one spot being illuminated by 4.5 mW for 36 s.	77
FIGURE 4.12: M3599_12 Raman mapping after one spot being illuminated by 4.5 mW for 36 s.	77
FIGURE 4.13: M3602_21 Raman mapping after one spot being illuminated by 4.5 mW for 36 s.	77
FIGURE 4.14: Raman spectra of another random spot measured from CZTSe_97 surface before and after high laser power illumination.	80
FIGURE 4.15: Raman spectra of another random spot measured from M3599_12 surface before and after high laser power illumination.	80
FIGURE 4.16: Raman spectra of CdS rich spot measured from M3602_21 surface before and after high laser power illumination.	81
FIGURE 4. 17: Raman spectra of three CZTSe samples measured from the cleaved edge.	82
FIGURE 4. 18: Raman spectra of three CZTSe samples measured from the cleaved edge after being illuminated by 1.47 mW.	84
FIGURE 4.19: Raman spectra of three CZTSe samples measured from the cleaved edge after being illuminated by 4.5 mW.	85
FIGURE 4.20: Optical image and Raman mapping of CZTSe_97 measured from cleaved edge with one x-line illuminated by ~ 2.45 mW.	87
FIGURE 4.21: Optical image and Raman mapping of M3599_12 measured from cleaved edge with one x-line illuminated by ~ 2.45 mW.	89
FIGURE 4.22: Optical image and Raman mapping centered at 261 cm^{-1} of M3599_12 measured from cleaved edge with one x-line illuminated by ~ 4.5 mW.	89
FIGURE 4.23: Raman mapping of M3602_21 measured from cleaved edge with 4.5 mW.	90
FIGURE 4.24: Raman spectra from multiple cleaved edge spots of M3602_21 measured with 6.5 mW.	90
FIGURE 4.25: Raman spectra of CZTSe_97 measured from front surface at different temperature and CZTSe main peak shift with temperature.	92
FIGURE 4.26: Raman spectrum of another random surface spot from CZTSe_97 measured at $460\text{ }^{\circ}\text{C}$.	93

FIGURE 4.27: Two types of Raman spectrum measured from CZTSe_97 surface at 480 °C.	93
FIGURE 4.28: Three different types of spots on CZTSe_97 surface when back to room temperature.	94
FIGURE 4.29: Raman spectra of three types of spots from CZTSe_97 surface after high temperature test.	94
FIGURE 4.30: Second test of Raman spectra of CZTSe_97 measured from front surface at different temperature and CZTSe main peak shift with temperature.	96
FIGURE 4.31: Raman spectra from CZTSe_97 surface after second high temperature test.	97
FIGURE 4.32: Raman spectra of M3599_12 measured from front surface at different temperature and CZTSe main peak shift with temperature.	98
FIGURE 4.33: Raman spectra of three types of spots from M3599_12 surface after high temperature test.	98
FIGURE 4.34: Raman spectra of M3602_21 measured from front surface at different temperature and CZTSe main peak shift with temperature.	99
FIGURE 4.35: Raman spectra of two types of spots from M3602_21 surface after high temperature test.	100
FIGURE 4.36: Raman spectra of different spots from M3601_21 surface after sample being heated to 400 °C.	101
FIGURE 4.37: LBIC mapping at lower laser power levels.	103
FIGURE 4.38: Raman mapping at ~ 169 μ W centered at 196 cm^{-1} .	104
FIGURE 4.39: LBIC at ~ 2.5 mW and ~ 2 μ W after ~ 2.5 mW illumination.	105
Figure 4.40: Raman mapping at ~ 169 μ W after center square being illuminated by ~ 2.5 mW.	105
FIGURE 4.41: LBIC and ~ 4.5 mW and ~ 2 μ W after ~ 4.5 mW illumination.	106
FIGURE 4.42: Raman mapping at ~ 169 μ W after center square being illuminated by ~ 4.5 mW.	106
FIGURE 4.43: Single spot LBIC at ~ 2 μ W after different illumination conditions.	107
FIGURE 4.44: LBIC mapping of M3602_21 measured from cleaved edge.	108
FIGURE 5.1: Macroscopic I-V curves from different CZTSe solar cells.	117
FIGURE 5.2: M3602_22 LBIC mapping with 532 nm laser at low and high power levels.	118

FIGURE 5.3: M3599_23 LBIC mapping with 532 nm laser at low and high power levels.	119
FIGURE 5.4: M3690_13 LBIC mapping with 532 nm laser at low and high power levels.	120
FIGURE 5.5: M3652_13 LBIC mapping with 532 nm laser at low and high power levels.	121
FIGURE 5.6: Raman spectra of random general spots from multiple CZTSe device surface.	123
FIGURE 5.7: M3652_13 LBIC mapping with 633 nm laser at low and high power levels.	125
FIGURE 5.8: M3690_13 LBIC mapping with 633 nm laser at low and high power levels.	126
FIGURE 5.9: Optical image and LBIC mapping of M3652_12 at $\sim 2 \mu\text{W}$ and $\sim 2.47 \text{ mW}$.	128
FIGURE 5.10: Raman spectra comparison of different spots from M3652_13 surface after 2.47 mW LBIC mapping.	129

CHAPTER 1: INTRODUCTION

1.1. Overview of Thin Film Solar Cell

People nowadays are faced with an energy-economy-environment dilemma. First, an affordable electricity supply is essential for meeting basic human needs and fueling economic growth, yet 30% of the world population remain without reliable or sufficient electricity [1]. Second, harvesting, transport, processing and conversion of energy using the resources and technologies relied upon today cause a large share of the most difficult and damaging environmental problems such as air pollution, ocean pollution, acid precipitation, radioactive wastes, greenhouse gases and so on [2]. Solar photovoltaics is frequently cited as a promising energy supply option for a low-carbon future. Since the first photovoltaic (PV) effect was observed in 1839 [3], PV industry has witnessed blooming of solar cell technology in the past few decades. Initially designed for space activities in 1950s by Bell Laboratories, solar cells are now seen on residential rooftops. Fig. 1.1 shows the reported timeline of solar cell energy conversion efficiencies recorded by National Renewable Energy Laboratory (NREL) since 1976 to August, 2015.

Solar cell technology can be roughly divided into three generations. The first generation is mainly based on silicon wafers. Over 90% solar cells on the market are silicon based. The second generation cells are referred to as thin film solar cells. They are made of semiconductor materials such as amorphous silicon (a-Si), cadmium telluride (CdTe) and CuInGaS₂ (CIGS) with thickness in micrometers layer. Commercial thin film solar products were available in early 2006 [4]. Till 2014, it takes about 9% of the market share

[5]. A lot of research are going on for the third generation solar cells involving a variety of materials and some emerging technologies, for example: organic, conductive polymers, nanostructured and quantum dot PV, photoelectrochemical cells and so on.

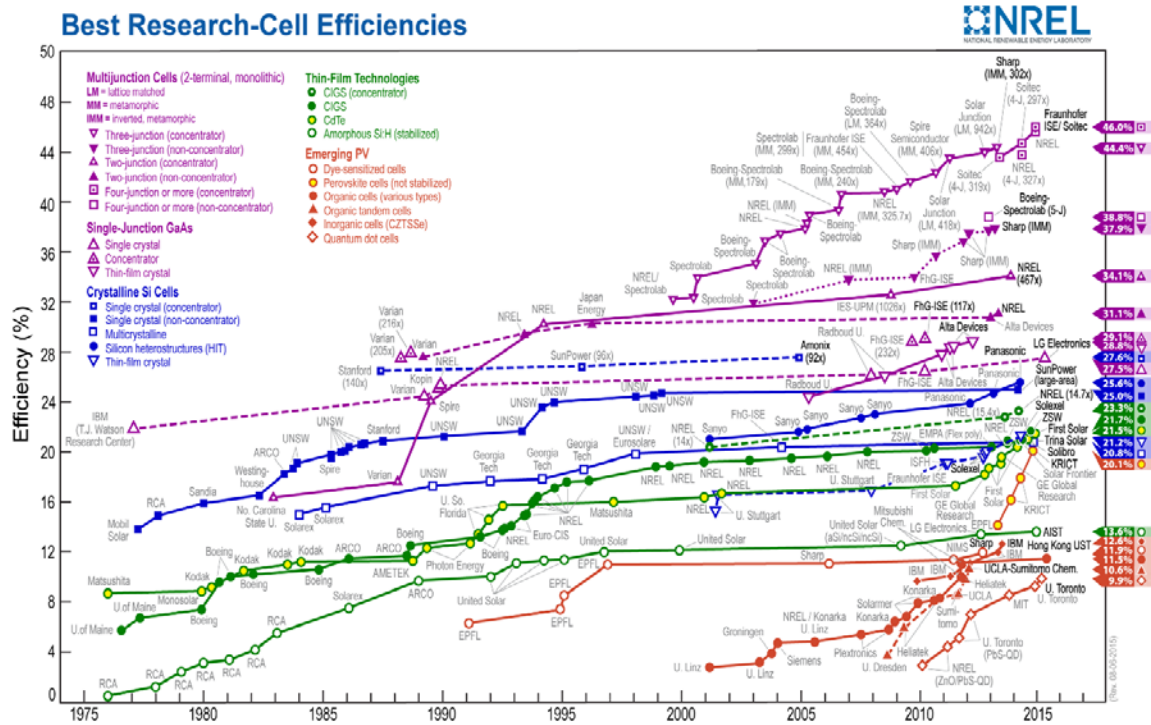


Figure 1.1: Reported time line of solar cell energy conversion efficiencies [6].

Thin film solar cells are proposed and widely studied due to its lower cost manufacturing processes, although they are slightly lower in efficiency than conventional crystalline silicon (c-Si) cells. With the significant efficiency improvement in recent years, in laboratory level, thin film cells have advanced over conventional multi-crystalline silicon which takes about 56% of the total solar cell production. Besides, by depositing one or more thin layers in micrometer (μm) scale, the thin film cells are more flexible and lighter than the silicon wafer based cells. At present, main commercially available thin film solar cells are a-Si, CdTe and CIGS.

a-Si as one of the earliest thin film technologies, it has been used from pocket calculators to home power supplies. The first a-Si:H solar cell was made by Carlson and Wronski in 1976 with a single p-i-n junction deposited on a glass substrate [7]. Nowadays, amorphous silicon panels are mainly fabricated by vapor-depositing about 1 μm of silicon on a glass or metal substrate. The principal advantage of a-Si solar cell is low manufacturing cost. Additionally, when manufacturing in a large area, a-Si is much more uniform than c-Si. Besides, the overall characteristics of the material will not be affected by impurities and defects too drastically. However, in addition to the lower energy conversion efficiency, the Staebler-Wronski effect is still an issue in a-Si cell application [8], and the life time is shorter than that of c-Si cells.

Since the company First Solar announced 17.3% CdTe solar cell efficiency in 2011, the efficiency of this type of thin film solar cell has been soaring in the past four years, now reaching 21.5% this February and a module efficiency 18.6% this June. In the thin-film CdTe cell, the p-n heterojunction is formed by p-type CdTe and n-type cadmium sulfide (CdS) in the form of a CdTe/CdTeS heterojunction [9]. The CdTe/CdS layers are deposited on a glass sheet (soda-lime glass for $< 550\text{ }^{\circ}\text{C}$ and alkali-free glass for $> 550\text{ }^{\circ}\text{C}$) coated with transparent conducting oxide (TCO). The CdTe absorber can be achieved by variety of methods, such as close-spaced sublimation, vapor transport, chemical spraying or electroplating [4]. Besides the low manufacturing cost, CdTe thin film solar cells also have some other advantages for example short energy payback time and abundance of cadmium [10]. However, the toxicity of cadmium is on the other hand the main concern of CdTe PV. There is wide concern about recycling CdTe modules at the end of their lift time

[11, 12]. Another limitation of an even larger scale CdTe cell application is the usage of rare elements of tellurium, which also contributes significantly to the module cost.

CIGS is a I-III-VI₂ semiconductor material with high absorption coefficient, which can absorb 99% of shining light in about micrometer of the material [13]. The band gap of CIGS is flexible by tuning each component within the absorber for the best PV application. Current best record efficiency of laboratory CIGS is 21.7%. This type of absorber can be deposited on different substrates such as soda-lime glass, metal foil and polyimide. Co-evaporation or co-sputtering copper, gallium and indium followed by selenization is the most common way to fabricate CIGS film. Other than the vacuum-based process, alternative non-vacuum-based processes have also been developed to further decrease manufacturing cost [14]. In addition to the widely studied CdS window layer, ZnO, ZnS, ZnSe and InS were also developed as “Cd-free” window layers [15-17]. So far, CIGS panels with competitive price and efficiency with c-Si and CdTe panels have not yet been achieved. Involvement of scarce element of indium can possibly become an obstacle for a large scale production of CIGS modules in the long run.

1.2. Cu₂ZnSnS₄ and Cu₂ZnSnSe₄ Thin Film

Quaternary compounds Cu₂ZnSnS₄ (CZTS) and Cu₂ZnSnSe₄ (CZTSe, if selenium is used to replace sulfur), which compose of copper, zinc, tin and sulfur (selenium), are proposed as other promising thin film absorber materials by substituting indium and gallium in CIGS absorber with zinc and tin. A group from UC Berkeley has conducted a study of material availability for large scale PV deployment [1]. According to their model, CZTS has been predicted as one of the materials which exhibit the greatest long-term potential. Fig. 1.2 shows the abundance of chemical elements in Earth’s upper continental

crust. All elements of CZT(S,Se) copper, zinc, tin, sulfur and selenium are rich from Earth. However, the content of indium is relatively low and tellurium is even considered among the nine rarest “metals” in Earth’ crust. As a result, thin film PV materials CdTe and CIGS both are constrained by one or more particular element(s) for long term and large scale production. In addition to the abundance in Earth, all the element in CZT(S,Se) are non-toxic. In recent years, CZT(S,Se) has attracted a lot of attentions as an environmentally friendly and low cost PV material.

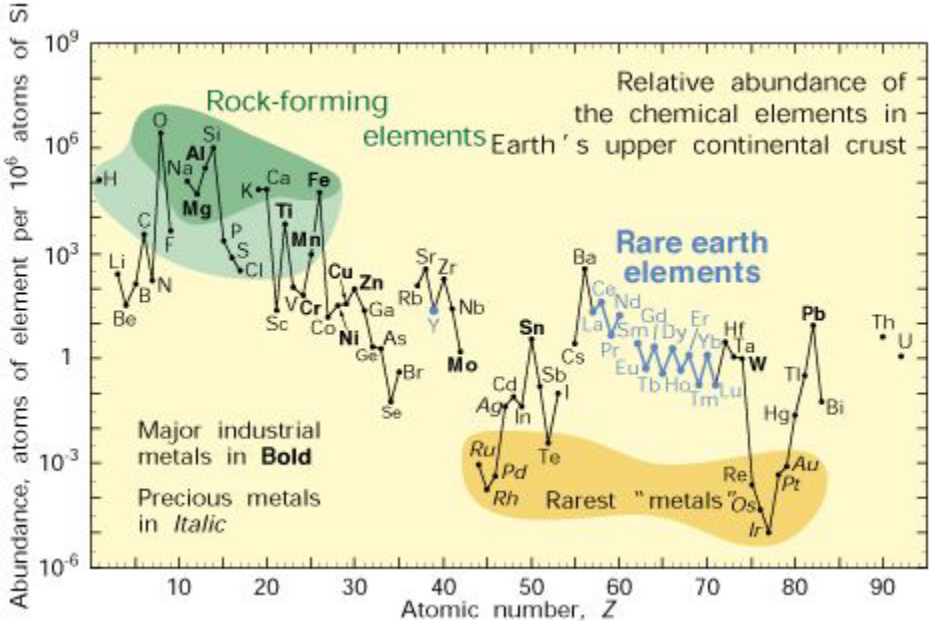


Figure 1.2: Abundance of the chemical elements in Earth’s upper continental [18].

Created in 1967 [19], not until 1988 did people found the PV effect of CZTS [20]. CZTS, as a p-type semiconductor, has a high absorption coefficient in 10^4 cm^{-1} scale for visible lights. And the direct optical band gap is found at 1.45 eV which matches the best semiconductor band gap value for PV application according to Shockley-Queisser limit [21]. Thereafter, people have been devoted to fabricate solar devices with this material and

the efficiency of CZT(S,Se) cells have been continuously increasing over the past twenty years. The first CZTS cell was fabricated in 1996 with only 0.66% efficiency and open circuit voltage (V_{oc}) of 400 mV [22]. The efficiency was improved to 2.3% and V_{oc} to 470 mV for both CZTS and CZTSe cells the next year [23]. Till 2008, CZTS cell efficiency was improved to 6.7% [24]. In 2010, 7.2% and 9.6% CZTSSe cells were fabricated in different methods [25, 26]. And the first CZTSSe cell with over 10% efficiency was demonstrated in 2011 [27]. As of 2014, the highest energy efficiency obtained from CZTSSe solar cell is 12.6% [28].

The quaternary compound CZTS(Se) exists in three crystal structure: kesterite (KS), stannite (ST) and primitive mixed CuAu-like structure (PMCA) as shown in Fig. 1.3 [29]. Among them, kesterite structure with the $I\bar{4}$ symmetry is calculated as the most stable one [30, 31], but due to the small difference in total energy (about 3 meV/atom) between KS and ST structure, they may coexist in the synthesized material [29]. For all structures, cations and anions form a tetrahedral bonding configuration with a zincblende stacking. In KS structure, the cation layers alternate in CuZn, CuSn, CuZn and CuSn at $z = 0, 1/4, 1/2$ and $3/4$ respectively. Whereas in ST structure, the cation layers alternate between Cu_2 and ZnSn, and Zn atoms switch with position with Sn atoms every other layer. In PMCA structure, such position swapping is absent, which makes it different from ST structure. Recently, partially disordered KS structures with disordered Zn and Cu atom were also observed using neutron diffraction measurement [32, 33]. Furthermore, because the off-stoichiometry CZTS(Se) materials have been found empirically to result in better device performance, in this case, the material structure is inevitably disordered.

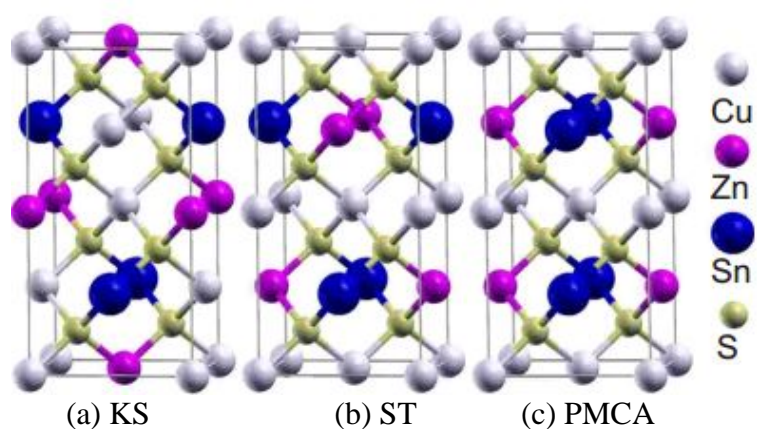


Figure 1.3: Crystal structures of CZTS [29].

The bandgap of CZTS is calculated around 1.5 eV for KS structure, and 1.3 eV ~ 1.4 eV for ST structure [29, 30]. Experimentally, CZTS film prepared in different methods are mostly reported to have band gap from 1.4 eV to 1.6 eV [20, 34-39]. Studies have shown that many factors such as element ratio, sulfurization condition and metal stack order may affect the band gap of this material [39-41]. In Ref. [41], CZTS thin films were prepared in sputtering method with different stacking precursor order: (A) Cu/SnS₂/ZnS/glass, (B) ZnS/Cu/SnS₂/glass and (C) SnS₂/ZnS/Cu/glass. It is found that secondary phases Cu_{2-x}S and SnS are easy to form in (B) and (C) stacking films, leading to band gaps at 1.35 eV and 1.1 eV, respectively, which is narrower than the 1.45 eV band gap of single crystalline kesterite CZTS thin formed in (A) stacking. Though it was found that Zn content does not influence CZTS band gap much, increasing Sn/Cu ratio can contribute to a steep band gap increase [40]. On the other hand, there was controversy about the band gap of CZTSe film, experimentally measured at 0.85 eV [42], 0.95 eV [43], 0.96 eV [44], 1 eV [45], 1.44 eV [46], 1.56 eV [47] and 1.42 – 1.58 eV [48]. However, using first principle calculation, CZTSe bandgap is predicted around 1 eV [29]. Ahn and her co-workers proposed that the

existence of ZnSe within the film as the possible reason for the large discrepancy of CZTSe band gap [49]. Same with CZTS film, the elemental stoichiometry also has a significant impact on CZTSe optical and electrical properties. Cu-poor films are found to have higher band gap than Cu-rich films. Varying Cu/(Zn+Sn) ration from 0.83 to 1.14 leads to a band gap drop of 250 meV [39]. By replacing partial sulfur in CZTS with selenium, CZTSSe film is also used as solar cell absorber. The current world record solar cell using this type of absorber is based on CZTSSe alloy [28]. One advantage of CZTSSe film attributes to the possibility to engineer the band gap of CZTSSe by tuning S/Se ration from 0.9 eV to 1.5 eV. It is proved theoretically and experimentally that the band gap of CZTSSe alloy decrease almost linearly with Se content [50-53]. Besides, CZTSSe alloys with high selenium concentration have lower conduction band and are easier to be doped n-type. High efficiency CZTSSe based solar cells can be achieved by balancing the band gap size and doping ability [50].

Various types of defects are possible in quaternary compound CZTS. Shallow or deep levels will be introduced within the band gap by these defects, which will act as traps or recombination centers affecting properties of the material. S. Chen et al. and A. Nagoya et al predicted that Cu substitution at Zn site (Cu_{zn}) will be the dominant intrinsic defect in CZTS if the film is grown in an equilibrium condition [31, 54]. However, Cu_{zn} brings deep acceptor level compared with Cu vacancies (V_{Cu}), which is not a preferable situation for PV applications. As a result, CZTSSe cells with higher efficiency are fabricated in Cu-poor

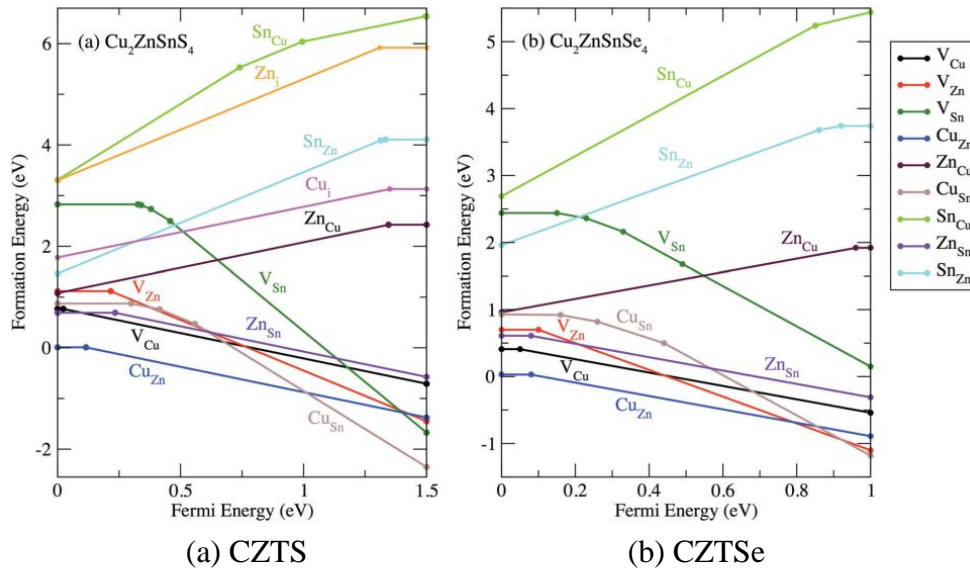


Figure 1.4: Calculated defect formation energy as a function of the Fermi energy at the thermodynamic chemical-potential point for CZTS and CZTSe. (Only the most stable charge state is plotted for each value of the Fermi energy) [55].

and Zn-rich conditions. According to Chen et al.'s calculation, the compensating defect complex $[\text{Cu}_{\text{Zn}}^- + \text{Zn}_{\text{Cu}}^+]^0$ are not benefiting carrier separation. To avoid this situation, Cu-poor and Zn-rich is also desired to form $[\text{V}_{\text{Cu}}^- + \text{Zn}_{\text{Cu}}^+]^0$ pair which should be more beneficial for optimize solar cell performance. Cu-poor and Zn-rich environment on one side helps to form V_{Cu} and Zn_{Cu} defects in the system, however on the other side may introduce secondary phase ZnS. Fig. 1.4 compares the energetic of defect formation in CZTS and CZTSe. In both materials, the acceptor defects have lower formation energy than the donors, which results in p-type conductivity and Cu_{Zn} antisite is believed to be the dominant defect [55]. However, the acceptor level for the antisite defect in CZTSe is shallower in CZTS and n-type doping in CZTSe should be easier, whereas the high conduction band minimum (CBM) level of CZTS make n-type doping difficulty in CZTS [56]. An inversion layer formed at the absorber and window layer interface is believed to facilitate the

electron-hole separation. With a shallower acceptor level and possible efficient n-type doping, CZTSSe alloy absorber could have advantages over pure CZTS based cells.

Single phase CZTS(Se) film is very hard to achieve according to the complicated phase space of CZTS(Se) predicted by theoretical calculations [31, 55, 57]. And it was indeed observed in experiments that secondary phases are often found in CZTS(Se) films [58-62]. Secondary phases in the absorber can affect the performance of CZTS(Se) cells, and it may be one possible reason causing efficiency of CZTS(Se) cells much lower than its counterpart CIGS cells [62, 63]. The most common secondary phases found are $\text{Cu}_x\text{S}(\text{Se})$, $\text{SnS}(\text{Se})_x$, $\text{ZnS}(\text{Se})$ and $\text{Cu}_2\text{SnS}(\text{Se})_3$ in CZTS(Se) films. In the following, CZTS will be analyzed as an example. Cu_xS is often observed in thin film for Cu-rich growth conditions. As discussed before, Cu-rich condition is in favor of more acceptor defects. In addition, CuS was found with excellent metallicity and p-type conductivity which may locally shunt the solar cell [64]. As a result, the photon-generated current cannot be extracted for an external load. Besides, the band gap of Cu_2S is around 1.2 eV, which is lower than CZTS. It can also act as recombination centers and reduce the V_{oc} of the cell [65]. On the other hand, with 2.2 eV band gap [66-68], SnS_2 would act as a barrier for the carriers and reduce the fill factor [69]. ZnS is usually formed in Sn- and Cu- poor or Zn-rich conditions. Due to the wide band gap of 3.6 eV [70], the presence of ZnS will reduce the density of active area. When existing at surface, it may also absorb shorter wavelength and reduce the current in the cell [71]. Therefore, growth of pure CZTS(Se) film requires very strict control of chemical composition and processing conditions.

1.3. Structure of CZTS(Se) Devices

Fig. 1.5 illustrates the typical device structure of a CZTS(Se) solar cell which is very similar with the CIGS cell. Due to the small film thickness, thin film solar cells are deposited on a substrate to protect the back side. A good substrate material should at least have stable thermal, mechanical and chemical properties, sufficient film adhesion, suitable surface morphology to prevent shunt and are available at low cost. The most common substrate in thin film technology is the soda lime glass which contains sodium and benefits the solar cell performance [72]. Other materials such as polyimide, metal foils are also developed as thin film solar cell substrates.

Firstly, a metal layer is deposited on the substrate as a back contact. With good conductivity, working function and stability, molybdenum (Mo) is deposited by sputtering as back contact metal for CIGS and CZTS(Se) solar cells. The thickness of Mo layer is found to affect the properties of CIGS cells [73], and in CIGS cells, favorable ohmic contact attributes to the existence of MoSe_2 at the interface of Mo and CIGS layers [74-76]. However, CZTS and CZTSe are found to decompose with the contact of Mo [77, 78], leading to phase segregation [77]:



And in selenium compound, it is believed that the decomposition (1) also promotes the formation of highly oxidized Cu_xSe and selenization of SnSe in the following two reactions [78]:



Extra layers such as ZnO, TiN and TiB₂ are introduced to inhibit the above reactions [78-80]. However, these intermediate layers on one side suppress the formation of MoS(Se)₂, on the other side bring along problems such as high series resistance in the device or degraded absorber's crystallinity. Thus, a better substrate material and design is urgent for CZTS(Se) devices.

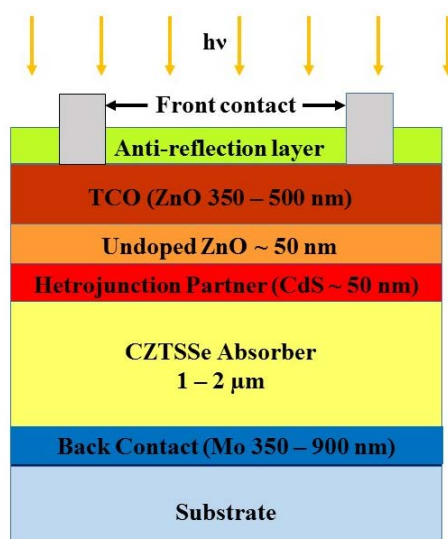


Figure 1.5: Schematic of the CZTS(Se) solar cell.

Absorber, the most important part of a solar cell is deposited on top of back contact. There are many methods been developed to grow CZTS(Se) film, for example, evaporation, sputtering, spray pyrolysis and solution based techniques which will be discussed later. Since CZTS(Se) is intrinsically p-type doped, an n-type layer is required to form a heterojunction for PV application. At present, CdS deposited by chemical bath deposition (CBD) is the most widely used and efficient window layer for CZTS(Se) cells. As the heterojunction partner, the window layer must be transparent so that the maximum light can reach the absorber and form good conduction band minimum (CBM) alignment with the absorber. Additionally, CdS layer also helps to passivate the surface states of the

absorber and protect the absorber from photo-degradation. However, driven by the intention to avoid the toxicity of cadmium, people are trying to find substitution of CdS as the window layer in thin film solar cells [81-84]. Zn-based materials are demonstrated bringing either high series resistance or low shunt resistance in Refs. [81, 83]. In_2S_3 turns out to be a competitive candidate with a proper conduction band offset with the absorber [81]. The CdS is then capped by a thin layer of intrinsic ZnO which is used to protect absorber and CdS from damage when depositing the following transparent contact layer [85].

Aluminum doped zinc oxide is widely used as transparent conducting oxide (TCO) layer in thin film solar cells. The main purpose of this layer is to carry out the electrons while transmitting as much as possible light. ZnO as an abundant and nontoxic material, has large band gap around 3.3 eV and heavy Al doping offers good conductivity. To ensure more light reaching absorber layer, an anti-reflection coating is usually deposited as the final layer. Similar to other optical equipment, the anti-reflection layers are chosen at a special thickness to take advantage of destructive interference. In CZTSSe cells, MgF_2 is usually used as the anti-reflective coating.

1.4. Fabrication of CZTS(Se) Absorber

Proposed as a low cost thin film PV material, the fabrication of CZTS(Se) needs to be accomplished at low cost while possessing high processing rate with good quality film and reproducibility. As discussed in section 1.2, the current common barrier in CZTS(Se) fabrication is the complicated phase equilibrium depends sensitively on the compositional control, which makes high quality single phase CZTS(Se) very hard to achieve. Numerous methods have been developed successfully to grow CZTS(Se) films, and they can roughly

categorized as vacuum and non-vacuum methods. Most of them are mirrored from the successful CIGS fabrication.

Evaporation is a well-known vacuum technique in CIGS fabrication. There are three phases of evaporation process: (1) evaporate the source material; (2) transport the atoms or molecules to the substrate; and (3) condense the vapor phase material on the substrate [86]. The first CZTS cell was also fabricated with absorber deposited by an electron beam (E-beam) evaporation method [22]. Cu/Sn/Zn metal precursors were deposited by E-beam evaporation sequentially on a soda lime glass substrate. The metal layers were then sulfurized at 500 °C in N₂ + H₂S (5%) atmosphere to obtain a CZTS film. Later, other materials were used as precursors in this method, for example ZnS as a source of Zn [87, 88]. Besides, the precursors stacking order was modified and sulfurization condition was also improved [89]. H. Katagiri found that with Sn/Cu/ZnS precursor the surface morphology could be improved [87].

Co-evaporation is also a widely used methods for compounds deposition, with which the film composition can be controlled precisely. In 2006, nearly stoichiometric composition kesterite CZTS thin films were successfully fabricated by evaporation of Cu, Zn, Sn and S elemental sources simultaneously at various substrate temperatures [90]. CZTSe was also successfully deposited with the co-evaporation method, achieving the current highest 9.15% total area efficiency in 2011 by an NREL group [44]. 8.4% CZTS device was demonstrated by co-evaporation of precursors at low temperature (150 °C) followed by a short high temperature (540 °C) annealing [91]. And thermal evaporation was also conducted with evaporated Sn/Cu/ZnS precursors deposited on substrate at room temperature and then sulfurized at 550 °C for 3 hours [92]. Fast co-evaporation of ZnS, Sn,

Cu and S sources can also achieve near stoichiometric single phase polycrystalline CZTS thin film with subsequent KCN etching away the CuS secondary phase [93]. Weber et al. applied multi-stage evaporation method to CZTS thin film fabrication with two different stage sequences: (A) Cu_2SnS_3 precursor reaction with Zn-S and (B) ZnS precursor reaction with Cu-Sn-S [94], and a SEM image reveals that type B results in a denser and larger crystallites film than type A. In multi-stage processes, different evaporation sequences allow compositional gradients which can be used for band gap engineering.

The sputtering techniques can also be realized in either a directly or two-stage process. The second step in the two-stage process is to sulfurize the metallic precursors Cu-Zn-Sn, Cu-Zn-Sn-Cu or Cu-ZnS-SnS. The first CZTS film observed with PV effect was made by atomic beam sputtering on corning 7059 glass heated more than $90\text{ }^\circ\text{C}$ in argon atmosphere [20]. In 2003, the film was deposited with radio frequency (RF) magnetron sputtering without substrate heating. Finely mixed Cu_2S , ZnS and SnS_2 were cold-pressed at 250 MPa followed by annealing in $\text{Ar} + \text{S}_2(\text{g})$ at $250 - 400\text{ }^\circ\text{C}$. The $\text{Cu}/(\text{Zn} + \text{Sn})$ ratio was close, but the $\text{S}/(\text{Cu} + \text{Zn} + \text{Sn})$ ratio was less than the stoichiometry of CZTS. Higher quality thin film with better crystallinity and lower sheet resistance were resulting from higher annealing temperature [34]. Hybrid sputtering, which combines evaporation and sputtering, was introduced to the fabrication of CZTS film in 2005. This method is expected to inherit the advantages from both evaporation and sputtering while eliminating some drawbacks of these two methods, for example, large area deposition, precise control of film composition and less plasma damage caused by bombardment of anions. In Ref. [95], Sn and Cu depositions were carried out by DC and RF sputtering respectively, and Zn was evaporated before Cu deposition. The film was obtained by sulfurizing the Cu/Zn/Sn precursor in

sulfur flux. Best results came with 400 °C substrate temperature, whereas the film became Zn-poor when the substrate temperature is higher than 450 °C. In 2006, CZTS film was successfully prepared by sulfurization of ion beam sputtered precursor on soda-lime glass [96]. P. Fernandes and his co-workers studied the CZTS film obtained by another two step method, in which the metallic precursors Cu/Zn/Sn or Zn/Sn/Cu were DC magnetron sputtered in sequence on soda lime glass coated with molybdenum [60, 97]. Reactive magnetron co-sputtering is well suitable for large scale production as a direct one-step depositing process. F. Liu et al. first grow high quality CZTS film by a reactive magnetron co-sputtering technique in 2009. H₂S was introduced to react with metallic copper, zinc and tin targets [98].

Pulsed laser deposition (PLD) is an important technique for thin film preparation, where a high power pulsed laser beam is focused inside a vacuum chamber to strike the target material [99]. In 2006, CZTS films were grown epitaxially on GaP substrate by PLD for the first time [100]. Later, laser parameters, target to substrate distance, substrate temperature, background gas and pressure, deposition time and target composition were all studied as the aspects which influence the growth of thin film [101-103]. CZTSSe was also successfully deposited on quartz substrate by PLD one-step process [104]. The current highest efficiency CZTS thin film solar cell prepared with PLD method is ~ 5.85% [105].

The methods discussed above all involved with vacuum processes which usually require expensive and complicated evacuation systems. Non-vacuum process attracts a lot of interest in the past decade owing to their potential of low cost and flexibility to large area coating. A variety of non-vacuum methods were also developed to fabricate CZTS films. The best record CZTSSe device was produced by hydrazine (N₂H₄)-based pure

solution processing approach [28]. This method was developed from a hydrazine based slurry processing method [26], where Cu_2S and $\text{SnS}(\text{Se})$ is dissolved in hydrazine with elemental Zn powers added. The reaction results in $\text{ZnS}(\text{Se})\text{N}_2\text{H}_4$ nanoparticles dispersed in the Cu-Sn-S-Se solution. In the hydrazine pure solution, a zinc salt is used instead of elemental zinc. The precursor material is then spin coated to Mo-coated soda lime glass followed by heat treatment at temperature $> 500\text{ }^\circ\text{C}$.

However, due to the high toxicity of hydrazine, other solution based methods such as spray pyrolysis, sol-gel sulfurization, electrodeposition and nanocrystal-ink-based approaches also attracts a lot of interest. Among them, nanocrystal inks are demonstrated to be most successful in the fabrication of CZTSSe solar cells. This method begins with the synthesis of CZTS(Se) nanocrystals and the formulation of printable nanocrystal inks. The inks are deposited on the substrate to form a nanocrystal film which is later sintered under selenium vapor [86]. CZTS nanocrystals were firstly synthesized in solution through a hot-injection method for the first time in 2009 [106]. And the device efficiency was increased from 0.23% in 2009 [107] rapidly to 7.2% in the next year [25]. By using binary and ternary sulfide nanoparticles copper tin sulfide, ZnS, SnS, CuS and Cu_7S_4 , Y. Cao et al. managed to improve the total area efficiency to 8.5% in 2012 [108]. To date, Miskin et al have achieved 9%, the best efficiency with the nanocrystal ink method by modification of nanoparticle synthesis and selenization [109].

The first non-vacuum method to grow stannite CZTS thin film was spray-pyrolysis performed by Nakayama and Ito in 1996 [110]. It is a process in which the thin film is deposited by spraying solution on pre-heated substrate. Due to its simplicity, cost-effectiveness and structure control at molecular level, this method is popular in thin film

synthesis. The best cells fabricated by spray-pyrolysis is now 8.6% with CZTSSe absorber [111]. The precursor solution, selenization conditions and anneal temperature were all found having impact on spray-pyrolysis processed CZTS(Se) films [112-116].

Sol-Gel method is a homogeneous process transforming a solution into hydrated solid precursor which offers better control of the texture, composition, homogeneity and structural properties of the final solids [117]. Tanaka et al. started to prepare CZTS thin film by sulfurizing sol-gel deposited precursors in 2006 [118]. Since sulfide films cannot be directly obtained by sol-gel method, oxyhydrate precursor layers were first deposited and then sulfurized. Yeh et al. avoided the sulfurization step by spin coating CZTS precursors composed of solutions of copper chloride, zin chloride, tin chloride and thiourea dissolved in deionized water (30% ethanol) [119]. Chemical composition of sol-gel solution, annealing temperature and H₂S concentration effects on sol-gel fabricated CZTSSe film have been studied over the years [120-124].

Electrodeposition method has been used to fabricate CdTe and CIGS cells. In 2008, Scragg and his co-workers developed this method to fabricate CZTS thin film [125]. The metal precursors were electrodeposited on soda lime glass and then sulfurized in sulfur vapor. In Ref. [126], CZTS films were prepared with an electrodeposition method using choline-based ionic liquid as the electrolyte. Single step electrodeposition technique was reported in 2010. CZTS thin films were prepared from an aqueous electrolytic bath containing CuSO₄, ZnSO₄, SnSO₄ and Na₂S₂O₃ [37]. The highest efficiency of CZTSe solar cell fabricated by electrodeposition at present is up to 8% [127]. They found that annealing temperature at 550 °C gave the best and most-stable device performance.

In addition to the techniques discussed above, there are also other non-vacuum techniques such as a hydrothermal method which is well industrially established [128], low cost screen printing approach [129] and so on. Many of the CZTS(Se) fabrication methods involve with high temperature processing. However, CZTS(Se) will decompose into binary or ternary compounds at high temperatures ($> 350\text{ }^{\circ}\text{C}$), and Se and SnSe start to evaporate, which makes high quality material hard to achieve in high temperature processing. Solution based methods have been proposed to overcome this difficulty such as excess Sn and Se in co-evaporation [44], excess SnSe and Se in final heat treatment [130], excess chalcogen in precursor layers [26], fast heating ramps [131] and introduction of $\text{SnS}(\text{Se})_2$ capping layer to prevent the CZTS(Se) decomposition and to eliminate the Sn losses due to SnSe evaporation at high temperature [132].

1.5. Samples Used in This Study

Seven CZTSe samples were studied in this work: one sputtered bare film CZTSe_97; one co-evaporated bare film M3599-12; and five co-evaporated devices M3602_21, M3602_22, M3599_23, M3690_13 and M3652_13. Sample information is summarized in Table 1.

CZTSe_97 from Dr. Sergio Bernardi was prepared by selenization DC-sputtered Mo/Zn/Cu/Sn metal stacks. The metal stacks were deposited on 1.8 mm thick Ashai PV 200 glass substrate. Before selenization, 300nm molybdenum, 130 nm zinc, 155 nm copper and 180 tin metal stacks were annealed under Argon at atmospheric pressure to promote intermixing between Zn, Cu and Sn. Se flakes were used as selenization source. The kesterite film thickness was measured slightly thicker than $1\text{ }\mu\text{m}$, and a device with nominally similar absorber was measured with 5% efficiency (Dr. Bernardi, unpublished).

Table 1. Samples used in this study.

Samples	Efficiency	Fabrication Method	Absorber Thickness	Cu/(Zn+Sn)	Zn/Sn
CZTSe_97	Bare film	DC-sputtering	Slightly > 1 μm	0.85	1.25
M3599_12	Bare film	Co-evaporation	1.49 μm	0.82	1.32
M3599_23	~ 8%	Co-evaporation	1.49 μm	0.82	1.32
M3602_21	~ 8%	Co-evaporation	1.3 μm	0.87	1.28
M3602_22	~ 8%	Co-evaporation	1.3 μm	0.87	1.28
M3690_13	~ 4%	Co-evaporation	2.09 μm	0.85	1.41
M3652_13	~ 3%	Co-evaporation	1.54 μm	0.97	1.12

The other samples from Dr. Repins were grown using four-source thermal co-evaporation, which are similar to those reported in Ref. [44]. The devices were fabricated on soda lime glass substrate. On top of the 1 μm sputter Mo back contact, a 150 \AA NaF precursor was e-beam evaporated to enhance the Na content of the absorber. The CZTSe films were grown by co-evaporation elemental Cu, Zn, Sn and Se from thermal sources onto a 500 $^{\circ}\text{C}$ substrate. CZTSe film thickness varies from 1.3 μm to 2.09 μm . Devices were finished with a thin chemical bath deposited CdS layer, a sputtered resistive/conductive ZnO bi-layer, e-beam evaporated Ni/Al grids, an MgF_2 antireflective coating, and photolithographic device isolation. More details for the film growth and device processing can be found in Refs. [44] and [133].

1.6. Summary

Solar cell is considered as a viable power supply option for human's future. With the endless sun power source and fast development of semiconductors, solar cell has

experienced a boom in the past two decades. With minimum material requirement, short payback time and flexible materials, thin film solar cells are attracting more and more interest as a promising low cost PV technology. a-Si, CdTe and CIGS are three main absorber materials for thin film solar cells. However, they either have long-term stability issue or contain rare and/or toxic elements which can be an obstacle for large scale and long-term applications. New absorber materials CZTS and CZTSe containing only earth abundant and environmentally friendly elements have been proposed. With tunable band gap from 0.9 eV to 1.5 eV, high absorption coefficient and p-type conductivity, CZTSSe is believed to be a viable PV material for the large scale PV application.

The PV effect of CZTS film was found in 1988, and the first CZTS cell was fabricated with a power conversion efficiency at 0.66% in 1996. To date, the world record efficiency is 12.6% based on CZTSSe alloy. The quaternary compound has three types of crystal structures: kesterite, stannite and PMCA. Among them, kesterite is the main structure used for PV application. Intrinsic point defects Cu_{Zn} make the material p-type conductive. However, this type of defect brings deep acceptor level which is not a preferable situation for solar cells. As a result, Cu-poor and Zn-rich environment is desired for higher efficiency CZTSSe solar cells. According to the theoretical calculation, there is only a very narrow phase region to achieve a pure CZTS(Se) structure. It is even more difficult when fabricated with the off-equilibrium condition. Accordingly, secondary phases become an issue in the CZTS(Se) film fabrication and the device performance is also largely affected by the secondary phases in the film. $\text{Cu}_x\text{S}(\text{Se})$, $\text{SnS}(\text{Se})$, $\text{ZnS}(\text{Se})$, $\text{Cu}_2\text{SnS}(\text{Se})_3$ are the commonly reported binary and ternary secondary phases.

Many methods have been developed to grow CZTS(Se) thin film, and they can be roughly grouped as vacuum and non-vacuum based depositions or single step and two steps with sulfurization/selenization reaction methods. Vacuum based methods are mainly evaporation, sputtering and pulsed laser depositions. Due to low cost and ability for large scale deposition, numerous non-vacuum techniques have been developed for CZTS(Se) fabrication. And the current best CZTSSe device is achieved by a hydrazine solution based non-vacuum method.

CHAPTER 2: SPATIALLY RESOLVED TECHNIQUES

2.1. Micro-Raman and Photoluminescence Spectroscopy

Raman spectroscopy is named after C. V. Raman who observed Raman effect for the first time in 1928. Nowadays, Raman spectroscopy is used in various fields, from fundamental research to applied solutions. It is a spectroscopic technique taking advantage of light interaction with vibrational and rotational states of a material.

When light shines on a sample and interacts with the material, the dominantly scattering is elastic scattering which does not involve with energy change, and is referred to as Rayleigh scattering. However, it is also possible that the incident light interacts with the material in such a way that the energy is either transferred to or received from the sample, resulting an energy change of scattered photons or frequency shift of the scattered light. Such inelastic scattering is the so-called Raman scattering. Similar with Rayleigh scattering, the material in Raman scattering also needs to be polarizable since the incident photon interacts with the electric dipoles in the material. In classic terms, the interaction can be viewed as a perturbation to the material's polarization field [134]. From a quantum mechanics' view, the incident photons can excite the vibrational modes of the material, in this way, photons give up energy and scattered with a lower (red-shifted) frequency than that of Rayleigh scattered light. A spectral analysis of the scattered light can reveal light signals at frequencies different from the incident light, and the lower frequency lines are referred to as Stokes Raman scattering. Alternatively, if the system is already in a

vibrational excited state, it is possible that the vibrational energy can be transferred to the incident photon leading to a blue-shifted frequency which is larger the incident frequency, referred to as anti-Stokes Raman scattering. Fig. 2.1(a) shows the energy-level diagram involved in Rayleigh and Raman scattering, and Fig. 2.1 (b) shows the relative locations of three different scattering lines in spectrum. In most cases, the probability of a system in the vibrational excited states is much lower than in the ground state. As a result, the probability of the anti-Stokes scattering is usually much less than the Stokes scattering. Usually, Stokes scattering is studied in most applications.

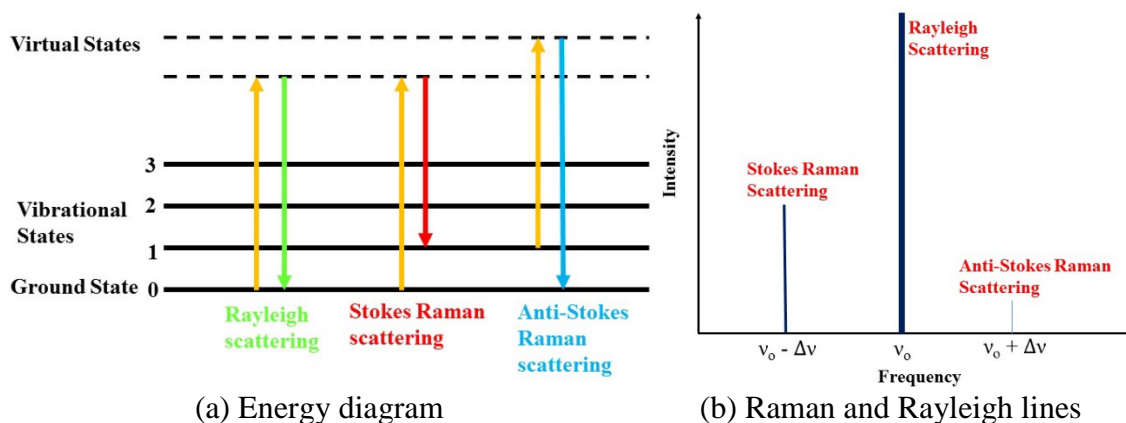


Figure 2.1: Energy-level diagram and relative location in frequency of Rayleigh, Stokes and anti-Stokes scattering.

The frequency shift or Raman shift is typically measured in wavenumber with a unit of inverse length. Since photon energy is inversely proportional to wavelength, the energy change can be converted to wavenumber of shift in Raman spectrum using the following equation:

$$\Delta\omega = \frac{1}{\lambda_0} - \frac{1}{\lambda_1} \quad (2.1)$$

where $\Delta\omega$ is the Raman shift in wavenumber, λ_0 is the incident wavelength, and λ_1 is the scattered wavelength. Usually, the unit chosen for wavenumber shift in Raman spectra is inverse centimeters (cm^{-1}).

Raman lines originate from a change in the polarizability of the material due to an interaction of light with the material, which corresponds to specific energy transitions. As a result, Raman spectroscopy is a form of vibrational spectroscopy. The energy of a vibrational mode is determined by lots of aspects: crystal structure, atomic mass, ionicity, bonding and so on, all directly related to the specific characters of the material. By probing individual vibration modes, Raman spectroscopy can be used to identify the structure and composition as it provides a “fingerprint” of the material being observed. Raman spectroscopy is a very important tool in semiconductor research and characterization.

By utilizing light interaction with a sample, Raman only involves a laser illuminating a sample and collecting the scattered photons, which offers some other great advantages of Raman spectroscopy such as non-destructive, no sample preparation, fast measurement and so on. With only a laser shining on the sample surface, Raman spectroscopy is totally non-contact and non-destructive (if the power is sufficiently low) which makes repeatable measurement and additional analysis by other techniques possible. It is also suitable to examine historic and precious pieces. It has the least requirement for sample size and phases (gas, liquid or solids). Raman analysis can be made as the sample is without any preparation such as dissolution or grinding which may be required in other techniques. When using a confocal Raman microscope, Raman spectroscopy can offer sub-micron spatial resolution so that individual particles or specific regions can be analyzed. And only

a few seconds to several minutes is need to obtain Raman spectrum which makes Raman spectroscopy a very fast technique.

When light shines on a material surface, another light interaction with the material may occur. There is a spontaneous emission of light from a material under optical excitation, and this process is called photoluminescence (PL). This phenomenon involves absorption of light energy and subsequent emission of photons. When photons with energy larger than band gap of a semiconductor is absorbed, and electrons on the ground state are excited to higher energy levels. Eventually, the excitations relax and the electrons return to the ground state. If a photon is emitted during this process, it is called radiative recombination, in contrast to the non-radiative recombination where the excited electron returns to the ground state by giving out the energy to phonons. Due to the vibrational relaxation, energy of photon emitted by PL is generally smaller than that of the absorbed photon. Obviously, PL spectroscopy is also non-contact and non-destructive which relates tightly with the material's electronic band structure. Typical application of PL spectroscopy includes band gap determination, impurity levels and defect detection and recombination mechanisms study.

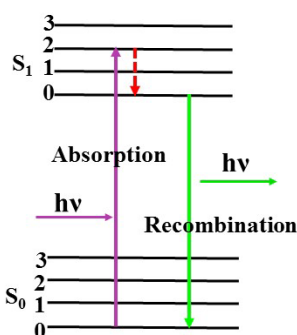


Figure 2.2: Energy diagram of PL.

In this study, Raman spectroscopy was performed with Horiba Jobin Yvon LabRam HR800 confocal Raman system. A simplified schematic of the system is shown in Fig. 2.3. Laser beam (green arrow line in the figure) from the back of the instrument is directed to a notch filter which can totally reflect it toward the microscope lens. Laser beam is then focused on the sample with the help of the objective lens available in 10x, 50x and 100x. Scattered lights including both Rayleigh and Raman scattering (red arrow line) are then collected by the objective lens in back scattering configuration to the notch filter, where Rayleigh scattered light is again reflected, leaving only Raman signals passing through. The Raman signal is focused onto the confocal hole that also serves as the entrance slit of the spectrometer. Finally, Raman signal is dispersed into its constituent parts, then captured by a CCD detector. The data are acquired and analyzed by LabSpec 5 software which is designed to control LabRam HR800 instrument. Multiple laser sources such as 325, 442 and 532 nm are available from the external laser entrance, while a 633 nm laser is integrated in the system. Laser power can be adjusted by neutral density (ND) filter at ND = 0, 0.3, 0.6, 1, 2, 3 and 4 before reaching the notch filter. Sample is placed on a motored XYZ stage which has 10 nm movement accuracy. With a translation stage, two-dimensional (2-D) or three-dimensional (3-D) mappings are possible with a specified mapping area or volume and step sizes. Moreover, using cryostat or heating stage, we are able to perform measurements from 10K to 1500 °C.

By using a laser with photon energy larger than the bandgap of the material of interest and corresponding settings in LabSpec software, PL spectroscopy can be performed with the same system. Similarly, reflectance can also be quantitatively obtained by measuring the light intensity reflected back to the system. One can find a pre-amp and a lock-in the

lower part in Fig. 2.3. These two units are connected to the system when laser-beam-induced-current data are collected. All these measurements can be carried out from the same sample area correlatively.

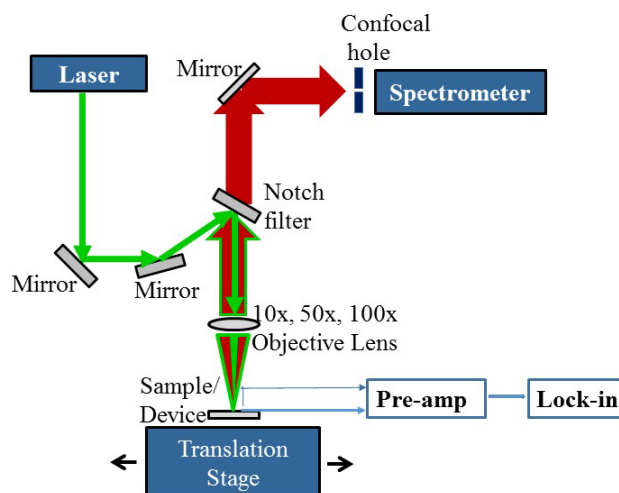


Figure 2.3: Schematic diagram of Raman system (simplified).

2.2. Laser-Beam-Induced-Current

Laser-Beam-Induced-Current (LBIC) is another high resolution, non-destructive optoelectronic characterization technique used in this study to spatially map device photo-response. In the technique, a laser beam is focused on the solar cell surface and the short circuit current induced by laser beams of the solar cell is measured. By scanning the laser beam across the sample or moving the sample with a XY stage, the current value at each point can be translated to a color value and shown as a 2-D LBIC mapping image representing the spatial distribution of the photo-response in the scanned semiconductor region. As a result, the electrical defects can be easily visualized with this technique. Depending on the laser spot size and scanning step size, the spatial resolution can range from sub-micron up to several hundred micrometers. It is well known that the spatial

inhomogeneity in a semiconductor can have significant effect on the uniformity in the performance of the final opto-electronic device. With micro-LBIC, inhomogeneity in micron scale can be identified.

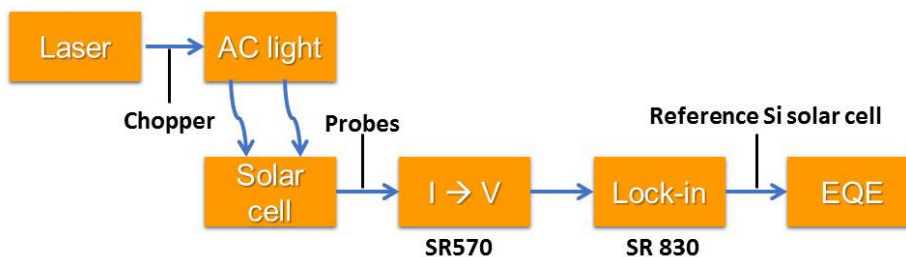


Figure 2.4: Schematic of electronic system to measure LBIC.

Taking advantage of the laser beam and moving stage of the Horiba Raman system, we have built an electronic system to measure the LBIC, as shown in Fig. 2.4. A mechanical chopper is used to modulate the laser beam to alternating light (AC light) so that the resulting AC current can be measured by a lock-in amplifier. A current pre-amplifier is used to improve the signal to noise ratio, in particular for very weak signal, for instance, down to pA level, if needed. Two gold plated probes (50 μm in diameter) are connected to the front and back contacts of the solar cell respectively to carry the LBIC from the solar cell to the external circuit. The current signal from the solar cell is first directed to the current amplifier with an insulated Bayonet Neill-Concelman (BNC) cable. The current amplifier converts the small current signal into a voltage output which is measured by the lock-in amplifier. The voltage data are finally converted to external quantum efficiencies (EQEs) with the help of a reference silicon solar cell that has a calibrated $\text{EQE}(\lambda)$ curve.

The current measured in this study can vary over more than four orders of magnitude depending on the incident laser power when different ND filters from ND0 to ND4 are

used. With ND4 filter, the excited current can be in as low as nano-ampere (nA) scale which is so small that the current can hardly be measured directly. A lock-in amplifier is widely used to detect and measure very small AC signals by extracting a signal with a known carrier wave from noisy environment. Before making the current signal measurable by the lock-in amplifier, Stanford Research Systems low noise current preamplifier SR570 is used. It provides a voltage output in proportional to the input current. More importantly, it has better amplitude and phase accuracy than a resistor alone in the presence of stray capacitance. Besides, the current amplifier can sink current directly into a virtual null or a selected DC bias voltage avoiding operation into possibly large bias voltages brought by resistive terminations [135]. The sensitivity of SR570 can be adjusted from 1 nA/V to 1 mA/V to produce a voltage output smaller than ~ 1 volt root mean square (RMS). However, according to the instrument manual, the frequency response and input impedance also depend on the sensitivity setting, for example, higher sensitivities will attenuate the signal at high frequency. By balancing the frequency and noise response, the sensitivity used in this study is chosen from 1 μ A/V to 1 mA/V depending on the input amplitude. Due to the used chopper frequency at 100 Hz, the filters within SR570 are set as band-pass with cutting off frequencies at 30 Hz and 300 Hz to guarantee the pass of the LBIC signal at 100 Hz while filtering out as much noise as possible.

The output of the current amplifier is measured by Stanford Research System digital signal processing (DSP) lock-in amplifier SR830. SR830 amplifies the signal and then multiplies it by a reference signal using a phase-sensitive detector (PSD) or multiplier. The input signal and reference signal are both square waves. With Fourier expansion, the output of the PSD is:

$$V_{psd1} = V_{sig} V_L \sin(\omega_r t + \theta_{sig}) \sin(\omega_L t + \theta_{ref}) = \frac{1}{2} V_{sig} V_L \cos([\omega_r - \omega_L]t + \theta_{sig} - \theta_{ref}) - \frac{1}{2} V_{sig} V_L \cos([\omega_r + \omega_L]t + \theta_{sig} + \theta_{ref}) \quad (2.2)$$

where V_{psd1} is the output of PSD, V_{sig} is the input signal amplitude, ω_r is input signal frequency, θ_{sig} is the input signal phase, and V_L , ω_L and θ_{ref} represent amplitude, frequency and phase of the reference signal. By passing through a low pass filter, only the signals which are very close in the reference frequency will be detected. Noise signals at frequencies different from the reference are attenuated by the low pass filter. Only the signal with the same frequency of the reference signal will not be affected by the low pass filter as DC output, which is:

$$V_{psd1} = \frac{1}{2} V_{sig} V_L \cos(\theta_{sig} - \theta_{ref}) \quad (2.3)$$

The PSD output is proportional to $V_{sig} \cos \theta$, where θ is the phase difference between the signal and the lock-in reference oscillator. However, there will be no output when $\theta_{sig} - \theta_{ref} = 90^\circ$. A second PSD with reference signal $V_L \sin(\omega_L t + \theta_{ref} + 90^\circ)$ is added to eliminate the phase dependency. Similarly, the output of the second PSD is

$$V_{psd2} = \frac{1}{2} V_{sig} V_L \sin(\theta_{sig} - \theta_{ref}) \text{ or } \sim V_{sig} \sin \theta \quad (2.4)$$

Now the magnitude (R) of the signal vector can be calculated by

$$R \sim \left[(V_{sig} \cos \theta)^2 + (V_{sig} \sin \theta)^2 \right]^{1/2} \sim V_{sig} \quad (2.5)$$

which is phase independent. With two PSD's, SR830 is called dual-phase lock-in and can measure the signal magnitude and phase difference between input and reference signal directly. According to its manual, SR830 only measures the first Fourier component of the signal at the reference frequency, which is $\frac{4}{\pi} V_0 \sin(\omega t)$ in the square

wave case with amplitude V_0 . The output signal is given in RMS. As a result, the measured and displayed magnitude value is $(4/\pi/\sqrt{2})V_0 = 0.9017 V_0$.

Time constant τ is another importance parameter of a lock-in amplifier. Not only does it determine the bandwidth of the low pass filter, but also reflects the speed of output response. Generally, a RC filter requires about 5 times of the time constant to settle to its final value. However, usually 3τ is adequate. With increased time constant, the output becomes more steady and reliable. In this study, for a 100 Hz signal, the time constant of 300 micro-seconds was used. For 2D mapping, the lock-in amplifier output is automatically collected by Labspec software via GPIB communication. At each spot, the software was set for continuous reading for 1 second, so that at least 3τ integration time could be taken for one single spot, and the corresponding output is finally recorded by the software.

External quantum efficiency (EQE) is an importation measurement of the light-to-current conversion sensitivity of a PV cell. For a solar cell, it is the ratio of the number of the electrons passing through the external circuit to the number of photons of a given energy incident on the solar cell [136]. If all photons are absorbed, and each photon generates one electron, and all the generated electrons are turned into the electrical current, the EQE will be unity. However, in the real world, the EQEs of the solar cells are reduced by recombination, and not all charge carriers are able to move to an external circuit. Besides, the external quantum efficiency of a solar cell includes reflection and transmission losses, which also leads to an EQE smaller than 1. Fig. 2.5 shows the EQE curve of a silicon solar cell. The plot is measured over a range of different wavelengths to characterize the device's EQE at different photon energies. At long wavelength when photon energy is below the

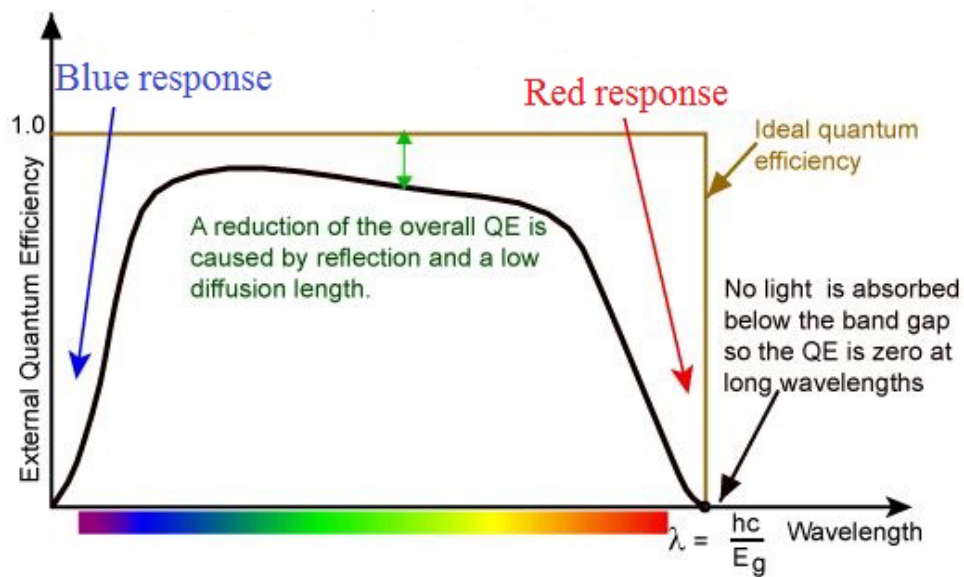


Figure 2.5: External quantum efficiency of a silicon solar cell [137].

semiconductor band gap, no electron-hole pair will be generated. And the EQE is usually not measured at wavelength below 350 nm because air mass 1.5 (AM1.5) contains very low power from these wavelengths. The high energy blue light is mainly absorbed near the surface, and considerable surface recombination will lower the quantum efficiency at the blue portion. Absorbed mainly in the bulk, a low diffusion length is the main factor which will reduce the quantum efficiency of green light. As for red portion in the spectrum, not only the low diffusion length, but also recombination at rear surface and reduced absorption at long wavelengths lead to low EQEs. In this study, green laser at 532 nm and red laser at 633 nm were used to generate the photo-current in solar cells. To achieve more accurate and stable measurement, a reference Si solar cell from PV Measurement Inc. was used to calibrate the system. With varying laser powers, EQEs of the reference cell measured by our system range from 61% to 65% (with less than 1% uncertainty) with 532 nm laser and

62% to 66% with 633 nm laser, which are very close to the 63.6% EQE at 530 nm and 64.9% at 632 nm offered by the vendor. The EQE of the tested device is calculated using equation:

$$EQE = \frac{V_{sample}}{V_{ref.}} * 64\% (532 \text{ nm}) \text{ or } 65\% \quad (2.6)$$

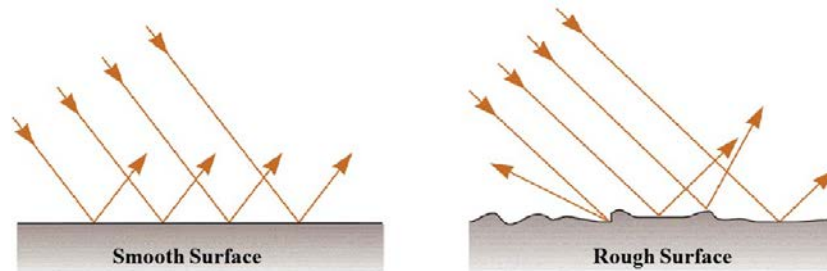
where V_{sample} is the output of the lock-in amplifier when the device is measured, and V_{ref} is the value for reference Si cell measured at the same condition.

2.3. Other Electrical and Optical Techniques

Solar cells are designed to absorb light in order to convert it into electricity. The more light that is absorbed, the more electrical energy can be potentially produced. Reflected light are uncaptured energy, thus higher reflectance will result in lower energy conversion efficiency. Anti-reflection layers are deposited to cover the surface of the solar cell for the purpose of reducing reflectivity and raising the solar cell efficiency.

According to the surface type, reflections are categorized in specular reflection and diffuse reflection, shown in Fig. 2.6. Specular reflection (Fig. 2.6 (a)) is generated by smooth surface like a mirror. Diffused reflection is generated by a rough surface. In this case, incident light is reflected at a wide range of angles rather than at just one angle. Many materials manifest a combination of both specular and diffuse reflectance. In this study, when measured macroscopically, reflectance was measured and calculated as the ratio of reflected laser beam power to the laser power incident on solar cell surface. Reflectance obtained in this way is dominant by specular reflectance, because of a small collection angle. In the microscopic scale measurement, using an objective lens with high numerical aperture (NA) focused on the sample surface helps to capture a major portion of diffusely reflected light as well as the specular reflection, as illustrated in Fig. 2.7. Reflected light intensity was obtained also with HR800 system. Using Thorlab aluminum mirror whose

reflectance data is provided by the vendor as a reference, we were able to convert the light intensity data to reflectance.



(a) specular reflection (b) diffused reflection

Figure 2.6: Two types of reflection.

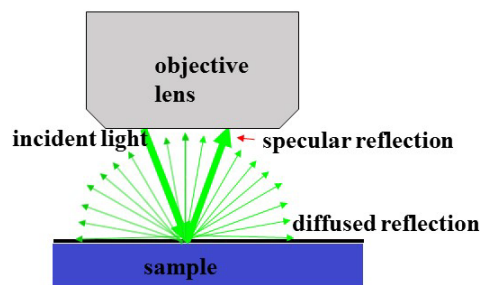


Figure 2.7: Microscope with high NA captures both specular and diffuse reflection.

I-V characteristic can offer a wealth of information about the performance of a solar cell. Ideally, the I-V curve of a solar cell is the superposition of the I-V curve of a diode in dark with the light-generated current:

$$I = I_L - I_D = I_L - I_0 \left[\exp\left(\frac{qV}{kT}\right) - 1 \right] \quad (2.7)$$

where I is the current of the solar cell, I_L is the light generated current, I_D is the diode current, I_0 is the reverse saturation current of the diode, q is the elementary charge 1.6×10^{-19} Coulombs, k is Plank constant 1.38×10^{-23} J/K, T is the cell temperature in Kelvin, and V is the measured voltage either produced or applied. Fig. 2.8 illustrates an I-V curve

measured from a silicon solar cell. The short circuit current (I_{SC}) is the current through the cell when voltage across the cell is zero, and it presents the largest current which may be produced by the solar cell. Similarly, open circuit voltage V_{OC} is the maximum voltage from a solar cell and it occurs when the net current through the device is zero. The power produced by the solar cell can be calculated by $P = I \times V$. The maximum product of I and V is denoted as P_{MAX} in the figure, and the corresponding current and voltage are I_{MP} and V_{MP} . Fill factor of a solar cell is defined as the ratio of maximum of obtainable power to the product of I_{sc} and V_{oc} . Solar cell efficiency is the most important parameter to reflect the solar cell performance. It is the ratio of the output power of the cell to the energy of the incident light. Intensity of the incident sunlight, temperature of the solar cell and some other ambient conditions may also affect the solar cell efficiency. Therefore, when comparing efficiency of PV cells, it is more reasonable to test them under similar conditions.

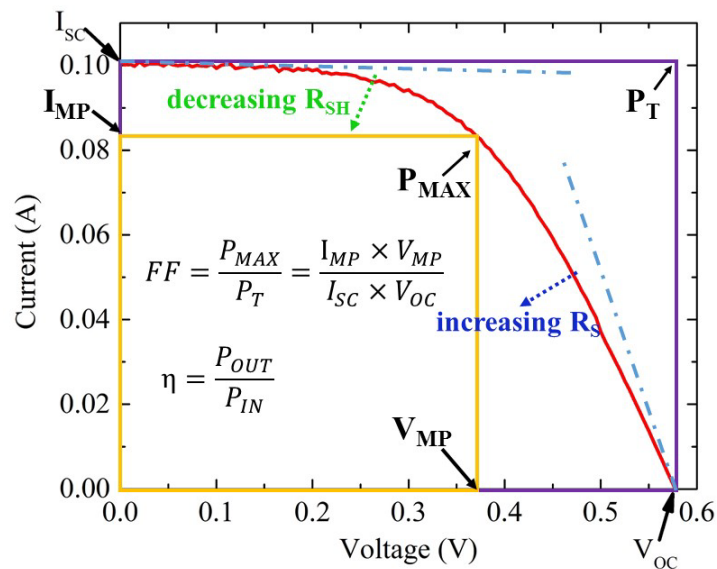


Figure 2.8: I-V curve of a silicon solar cell.

Internally, resistive effects in solar cell will reduce the efficiency by dissipating power in resistance. Most common parasitic resistance are series resistance (R_S) and shunt resistance (R_{SH}). The PV cell including series and shunt resistors is described in Fig. 2.9 using a single diode model, and the current of the solar cell is rearranged as the equation below [8]:

$$I = I_L - I_0 \left[\exp \frac{q(V+I \cdot R_S)}{nkT} - 1 \right] - \frac{V+I \cdot R_S}{R_{SH}} \quad (2.8)$$

where R_S and R_{SH} are respectively series and shunt resistance and n is the diode ideality factor. The main impact of series resistance is to reduce the fill factor by consuming power approximately $I^2 \times R_S$, which increase almost quadratically with increasing photo-current. Thus the series resistance loss is prominent at a high illumination intensity. With excessively high R_S , short circuit current may also be reduced. By providing an alternate current path for the photo-current, shunt resistance R_{SH} reduces the voltage from a solar cell. At a low light level, the loss of current due to small shunt resistance will have a large impact on the small photo-current generated by light illumination. Near V_{oc} , the I-V curve is strongly affected by R_S . The slope of the I-V curve at the open circuit point is used to estimate the series resistance. And similarly, an estimate of shunt resistance can be determined by the slope of the I-V curve at the short circuit point.

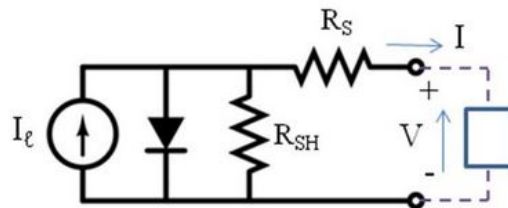


Figure 2.9: Single diode model of a solar cell [138].

In this study, I-V curves are measured in both macroscopic and microscopic scale illumination conditions. Macroscopy I-V curves are used to examine the properties of the entire solar cell device, while microscopy test helps to compare the photo-response of individual regions. Keithley 4200-SCS was used to obtain macroscopy I-V curves with an entire solar cell being illuminated by Scientech solar light simulator lamp. And in the microscopic measurement, a focused laser beam was used to excite the photo-current in a single spot on the solar cell, and the I-V curve was measured by Keithley 2401 source meter unit.

2.4. Summary

This work focuses on study of optoelectronic properties of thin film solar cell material CZTS(Se). In this chapter, main optical and electrical characterization techniques involved in this work are introduced. When tested with 100x confocal lens with NA = 0.9, sub-micron spatial resolution is achieved. Micro-Raman spectroscopy, with its ability to identify chemical compositions, was used to analyze the chemistry in CZTS(Se) film. Micro-PL was used to determine the band gap of the sample material and possible defects within the film. Micro-LBIC was used to probe the photo-response of CZTS(Se) solar cell, and examine the impact of microscopic inhomogeneity on solar cell performance at the same time. Micro-reflectance was used to measure the reflectance loss, especially to compare the general CZTS(Se) reflectance with the nonuniform regions. I-V curves in macroscopic were used to compare the important parameters of different cells as an entire piece, whereas microscopic I-V curves were used to compare the photo-response of different individual spots. Surface morphology was characterized by scanning electron microscopy (SEM) and atomic force microscopy (AFM). All characterization techniques

performed are non-destructive, which makes correlative examination of the same region with multiple techniques possible. In this work, we emphasize on the integration and correlation of multiple such techniques. By correlating multiple spatially resolved techniques, including micro-Raman/PL/reflectance/LBIC in conjunction with SEM and AFM, we were able to study the nature and impact of the inhomogeneity on CZTSe solar cell performance, achieve a better understanding of the secondary phase within CZTSe films, compare microscopic structural variations of CZTSe film fabricated by different methods, and compare CZTSe solar cells fabricated in different conditions.

CHAPTER 3: ILLUMINATION DENSITY DEPENDENCE OF LBIC AND THE EFFECTS OF CdS LAYER THICKNESS

3.1. Introduction

CdS has been widely used as window layer in thin film solar cells, including CdTe, CIGS, and CZT(S,Se) cells, due to its relative wide bandgap and sound chemical stability. The primary function of CdS layer is to form a hetero p-n junction with the absorber layer and allow most usable solar spectrum to reach to the absorber layer. It also act as a passivation layer, preventing the minority carrier from surface recombination. Additionally, it offers protection to the absorber from photo-degradation [139]. Efficiency of thin-film solar cells is known to depend greatly on the quality and thickness of the window layer. People have been working to optimize the window layer between the absorber and the front contact to improve the device efficiency in many types of thin-film solar cells, such as CuInS₂ [140, 141], CuGaSe₂ [142], CdTe [143, 144], CIGS [145] as well as CZTSSe [146]. In general, thinner CdS layer is preferable to reduce the absorption of the CdS layer and achieve higher short-circuit current (I_{sc}). However, this may also result in a sacrifice in open circuit voltage (V_{oc}) and fill factor (FF) [147-149]. Thus, an optimized thickness of CdS layer is expected to achieve better thin-film performance.

When forming heterojunction at the interface between window layer and absorber, there are two types of band alignment, the so called “spike-like” and “cliff” alignment, concerning the movement of electrons from the absorber layer to the window layer. In the spike-like alignment, which is type I heterojunction, the conduction band minimum (CBM)

of the CdS window layer is above that of the absorber and the valance band maximum (VBM) is lower than the absorber side, also referred to as positive conduction band offset (CBO). In contrast, when CBM of the window layer is lower than absorber CBM, a “cliff” forms, which is type II heterojunction, as shown in Fig. 3.1 using CIGS as an example. T. Minemote et al. did a detailed analysis of CBO effect on solar cell performance using a CIGS as an example [150]. According to their simulations, at spike-like configuration, 0.4 eV is the highest barrier for photo-generated electrons to cross. J_{sc} will decrease abruptly with CBO larger than 0.4 eV. At cliff alignment, no barrier against photo-generated electrons will form and J_{sc} will be constant. However, under forward bias, the cliff becomes a barrier against injected electrons, leading to more majority carrier recombination with the defects at the cliff interface, which will result in a great reduction in V_{oc} . When conduction band of the window layer is higher than that of the absorber, no such barrier was formed and V_{oc} will not be affected. Thus, 0 – 0.4 eV CBO is favorable for excellent performance thin film solar device. In CdS/CIGS structure, the conduction band of CdS is about 0.2 eV higher than that of CIGS conduction band, which largely contributes to superior performance CIGS cells.

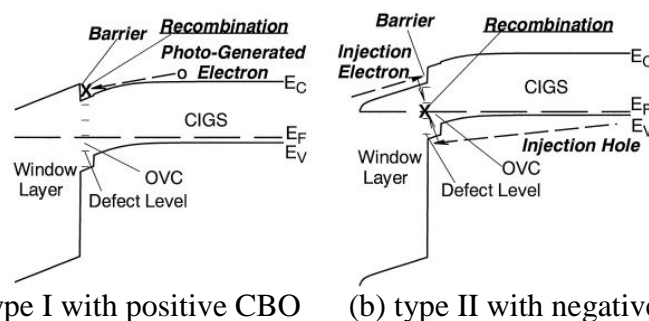


Figure 3.1: Two types of schematic energy band diagrams of window/CIGS structure [150].

CdS/CZTS structure is mostly reported as a type II heterojunction with a varying CBO value [56, 151]. Using ultraviolet photoelectron spectroscopy (UPS) and inverse photoelectron spectroscopy (IPES), M. Bar et al. [151] managed to measure a -0.33 eV cliff at the CdS/CZTS interface. S. Chen et al. [56] propose that type II band offset benefits electron-hole separation and the band bending at the absorber layer could be a positive factor for achieving high efficiency device based on the ordered vacancy compound (OVC) layer found in CuInSe₂ solar cells [152]. However, a positive CdS/CZTS CBO is presented in Ref. [153], and Ref. [154] also reports a spike structure in CZTSSe with varying sulfur ratio. The estimated CBO is 0.4 – 0.5 eV with sulfur/(sulfur+selenium) ratio from 0 to 1. The band alignment study of CdS/CZTSe heterojunction interface is very limited. J. Li et al. demonstrated a 0.34 eV CBO spike like structure at the CdS/CZTSe interface using X-ray photoemission spectroscopy (XPS) analysis in Ref. [155], and the spike like alignment is mostly used in CdS/CZTSe heterostructure analysis [146, 156]. At present, the CBO of CdS/CZT(S,Se) is still under debate, and it is believed depending on the CZTSSe bandgap and CdS deposition method and some other issues [63, 153, 154].

Previously, people have focused on optimize CdS layer in a macroscopic scale on solar device performance. In this work, we have investigated the microscopic scale CdS thickness inhomogeneity effect on the CZTSe device. Multiple spatially resolved techniques including micro-Raman/PL/LBIC/reflectance in conjunction with scanning electron microscopy (SEM) and atomic force microscopy (AFM) were applied as an effort to provide a more integrated and correlated study of the nature and impact of inhomogeneity in CZTSe solar cells. With 100x optical lens (NA=0.9), resolution of the measurement is sub-micron.

3.2. PL and Raman Characterization of CZTS and CZTSe

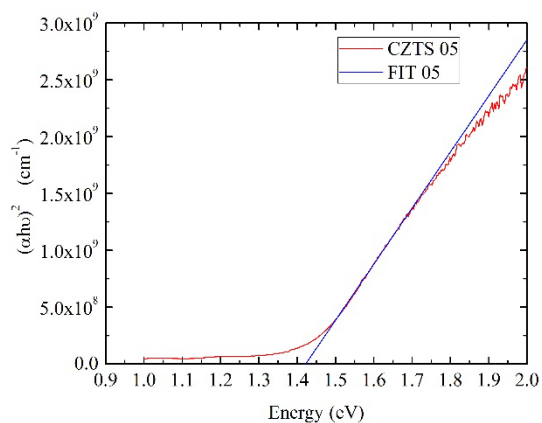
As mentioned in Chapter 1, the energy bandgap of CZTS is around 1.45 eV ~ 1.5 eV and optical absorption can help to estimate the bandgap of semiconductor near band edge, using the widely used relationship below [157]:

$$\alpha = \frac{A(\hbar\nu - E_g)^n}{\hbar\nu} \quad (3.1)$$

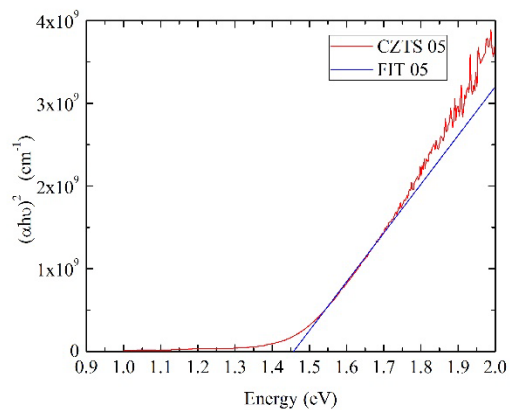
where α is the optical absorption coefficient, $\hbar\nu$ is the incident photon energy, E_g represents the band gap between the bottom of conduction band and top of the valence band. n is a constant: $\frac{1}{2}$ for allowed direct transitions, $\frac{3}{2}$ for forbidden direct transitions, and 2 for indirect transition [157]. This method is also widely used to estimate the bandgap of CZTSSe films, varying from 1.37 eV to 1.8 eV for CZTS [39, 88, 120, 158, 159], and 0.9 eV to 1.52 eV for CZTSe [45, 51, 58, 160]. Keep in mind that the bandgap derived this way only offers a rough estimate of the threshold energy for the optical transitions that can contribute significantly to the photo-carrier generation, but so obtained bandgap does not have the same meaning as the excitonic bandgap that can be unambiguously determined for a highly order crystalline material such as GaAs [161].

Absorbance of three CZTS sample CZTS_05, CZTS_29 and CZTS_30 were measured to estimate their band gap using ITO and air as reference. Due to the fact that CZTS has direct bandgap, $(\alpha\hbar\nu)^2$ is plotted versus photon energy from 1 eV to 2 eV. As shown in Fig. 3.2, the intercept of X-axis and the linear fit of the curve gives the bandgap of the tested material. For CZTS_05, the band gap is estimated at 1.42 eV using air as reference and is 1.46 eV using ITO as reference; For CZTS_29, the band gap is around 1.61 eV or 1.47 eV with different references; and the band gap of CZTS_30 is estimated around 1.60 eV or 1.53 eV. Band gap of CZTS can also be estimated using our Horiba

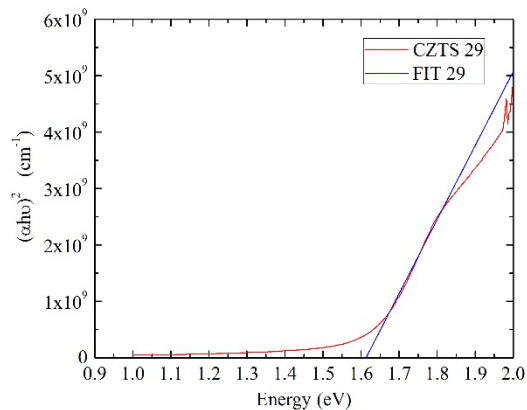
Raman system, for example, Fig. 3.3 shows the PL spectrum of a CZTS sample FSS 18 and the peak position indicates the band gap of this piece is about 1.39 eV. Due to the spectrometer limitation, bandgap of CZTSe was not measured in this work. According to literature, people estimated the band gap of CZTSe is around 0.95 eV [49, 53].



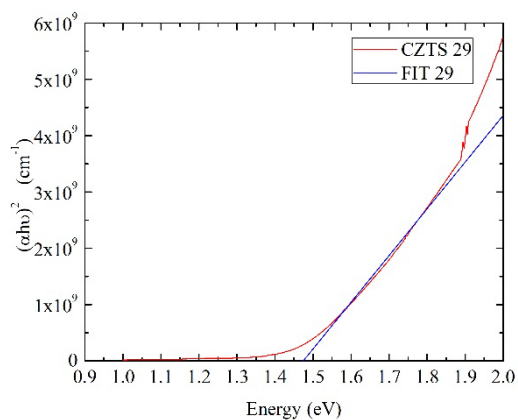
(a) CZTS_05 using air as reference



(b) CZTS_05 using ITO as reference



(c) CZTS_29 using air as reference



(d) CZTS_29 using ITO as reference

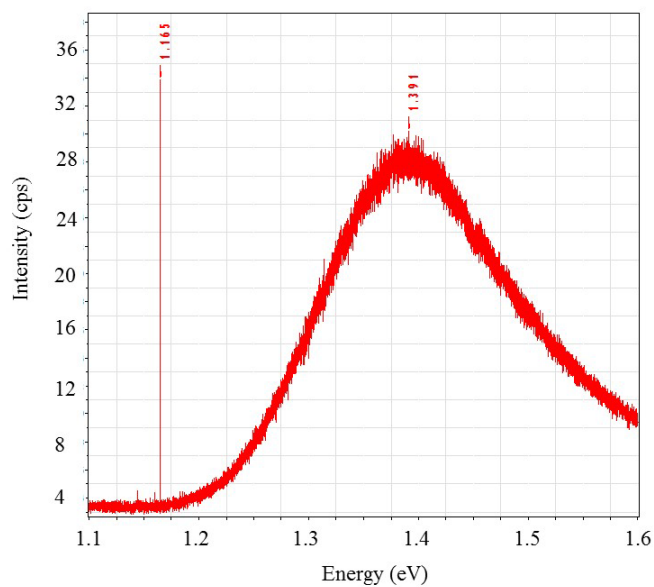
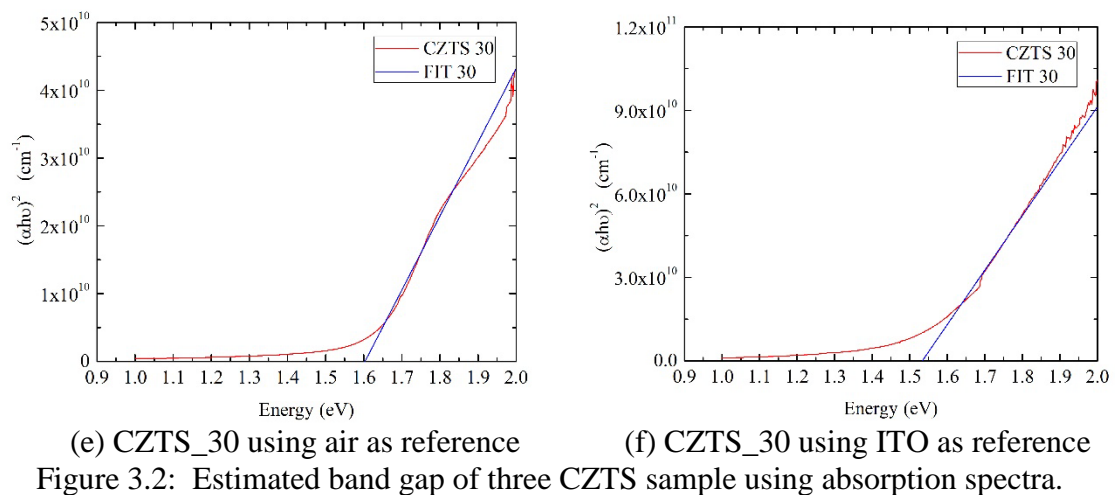


Figure 3.3: PL spectrum of CZTS sample FSS 18 using Horiba system at room temperature. (The spike at 1.165 eV is the second order signal of the 532 nm excitation laser.)

Raman modes of CZTS are reported at 338, 167, 252, 288, 347 and 366 cm^{-1} [53, 59]. A CZTS sample CZTS 13 was examined with a 532 nm laser power at $\sim 179 \mu\text{W}$ and 100x lens at room temperature, as shown in Fig. 3.4 (a). The dominant CZTS phase was found at 336.4 cm^{-1} and other phases at 165.9, 250.5, 285.3, 345.2, 365.2 cm^{-1} were also observed

very close to the literature values. Weak peak near 144.5 cm^{-1} was also reported as CZTS Raman both theoretically and experimentally [162-164] and the 671.5 cm^{-1} peak was identified as second order Raman scattering of CZTS [165, 166]. Same Raman spectroscopy was also performed with a CZTSe sample M3599_12, as shown in Fig. 3.4 (b). Reported single phase CZTSe Raman modes at 196, 172 and 233 cm^{-1} were all observed in sample M3599_12 [42]. Secondary phases such as SnSe_x at 143 cm^{-1} [167, 168] and ZnSe at 252 cm^{-1} [169-171] were also found in the film.

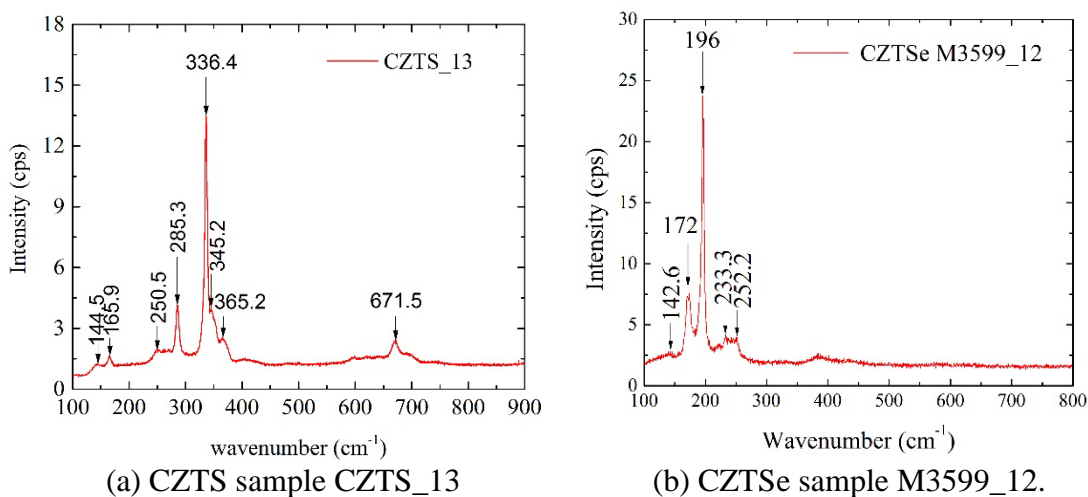


Figure 3.4: Raman spectra of CZTS and CZTSe measured with 532 nm laser at $\sim 179 \mu\text{W}$.

3.3. CdS Rich Regions on CZTSe Devices

As stated in section 3.1, the CdS layer is crucial for the thin-film solar devices in many aspects. Previously, people focused on its role in solar device performance in a macroscopic scale, i.e., optimizing it through the performance of a device as a whole. In this work, we investigate the impact of micro-scale inhomogeneity in the CdS layer on device performance by correlating multiple spatially resolved techniques.

Three CZTSe samples were measured and compared: M3599_12 bare CZTSe film without CdS coating, M3599_23 device processed from the same film as M359_12; and M3602_22 CZTSe device processed from a different but similar film. All the CZTSe films were grown using a vacuum co-evaporation method, and the devices investigated have efficiencies larger than 8%, $I_{sc} \sim 15.0$ mA, $V_{oc} \sim 0.34$ V and fill factor (FF) $\sim 65\%$. The film thickness is about $1.4 \mu\text{m}$. Details for film growth and device fabrication can be found in [44, 172]. Raman excitation source 532 nm laser was kept less than 0.2 mW (4.8×10^4 W/cm²) in order to avoid any thermal effect or permanent material damage. Laser spot was focused on sample surface with a 100x objective lens whose numerical aperture is 0.9. Laser spot size is $\sim 0.72 \mu\text{m}$ and the spatial resolution of the measurement is about half of the spot size.

Optical image of the three samples are shown in the insets of Fig. 3.5. Three distinctly different types of areas were found on both device M3599_23 and M3602_22: bright spot, dark spot and general spot. The typical sizes of the bright spots vary from $1 \mu\text{m}$ to $5 \mu\text{m}$, and dark spot sizes are usually around $1 \mu\text{m}$. However, on the bare film sample, no bright spot was observed. Fig. 3.5 shows typical Raman spectra from the three types of spots measured for each sample. In addition to 172 cm^{-1} and 196 cm^{-1} CZTSe related Raman peaks, both CZTSe devices M3599_23 and M3602_22 give rise to a 303 cm^{-1} Raman peak in all the three spots. However, this peak is neither observed from the general nor dark spot from the bare film M3599_12. The CZTSe Raman peaks from all three samples have similar peak shape and intensity, which indicates similar absorber quality of the three

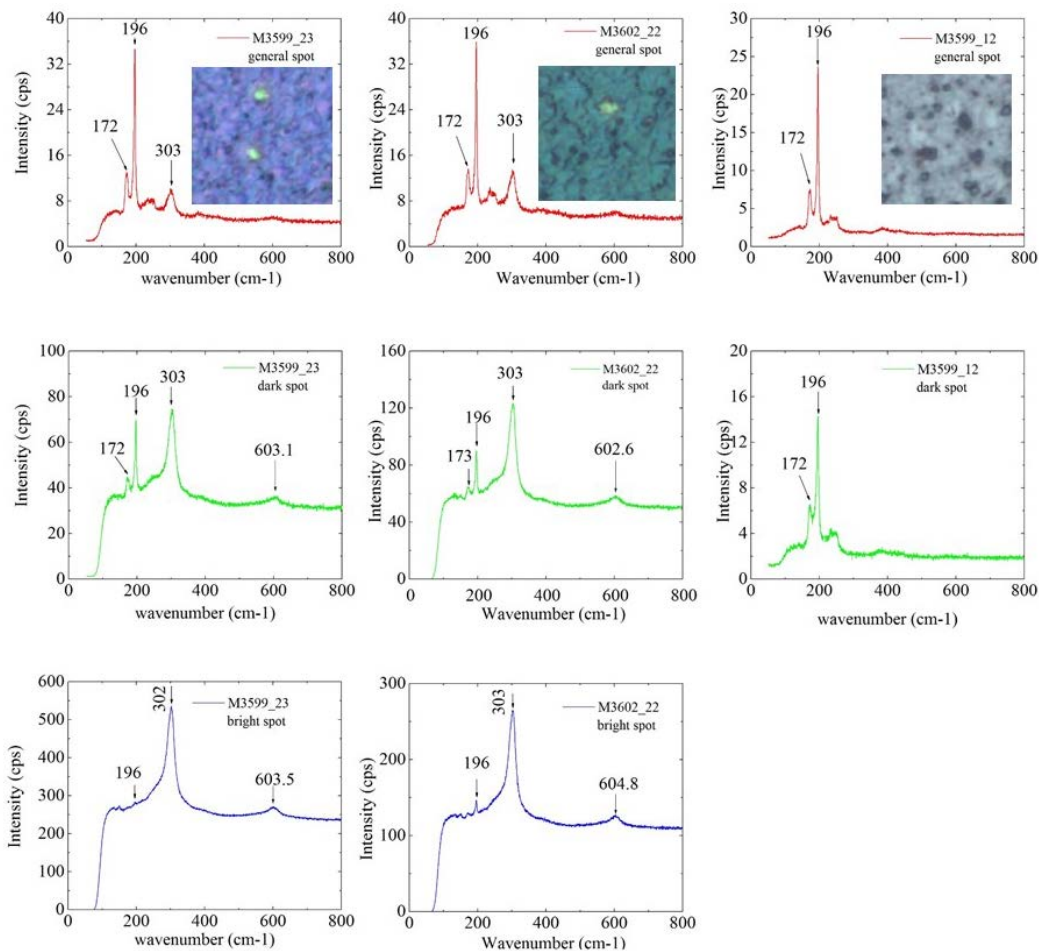


Figure 3.5: Raman spectra from bright spot, dark spot and general spot of three CZTSe samples.

sample. Since the 303 cm^{-1} peak only appears in the finished devices, it should come from the additional layers beyond the absorber. By noticing that the Raman shift is very closely matched to CdS longitudinal optical (LO) phonon, the 303 cm^{-1} peak can be attributed to the LO phonon mode of CdS. In addition, another peak near 603 cm^{-1} which matches the second order LO phonon Raman mode of CdS further support the assignment [173]. The intensity of 303 cm^{-1} is much less than that of CZTSe main peak in the general spot, comparable to 196 cm^{-1} peak intensity in the dark spot, and more than 5 times larger than that of the CZTSe peak in bright spot. Such strong enhancement of 303 cm^{-1} peak at the

bright and dark spots of the CZTSe devices can be understood as the resonant Raman effect of CdS, since the excitation laser energy of the 532 nm laser (~ 2.33 eV) is rather close to the band gap of CdS (~ 2.42 eV) [173]. Similar resonant effect has been reported previously in polycrystalline CdS thin films [148].

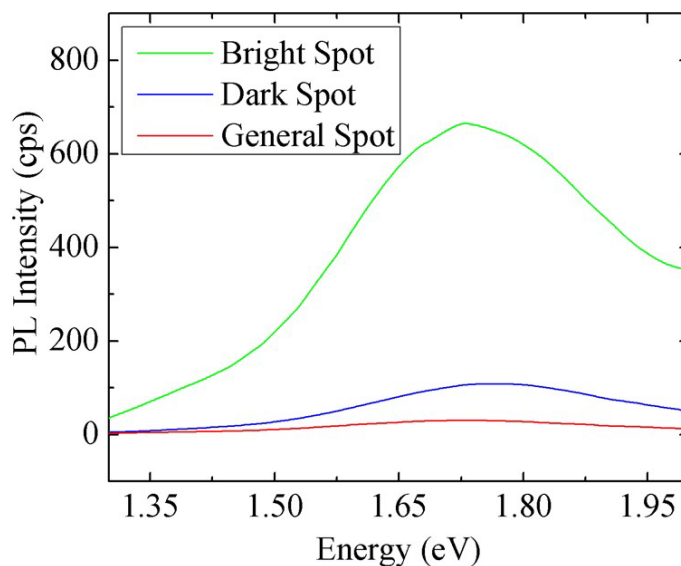


Figure 3.6: PL spectra from three types of spots on M3599_23 surface.

PL spectra from three different types of spots measured from M3599_23 surface were plotted in Fig. 3.6. A broad PL band at ~ 1.73 eV was found at bright and dark spot, which is much higher in energy than the measured PL band of similar CZTSe material at 0.96 eV [44]. CdS is known to have “red emission bands” at 1.70 – 1.86 eV, which is associated with the sulfur vacancies [174-176]. The broad PL band from bright and dark spot are attributed to the defects in the polycrystalline CdS layer, whereas no 1.73 eV spectral feature was observed from the bare absorber sample M3599_12. Thus, it is reasonable to conclude that the CdS layer is thickest at the bright spot and thinnest at the general area in

the CZTSe devices. CdS comes from the window layer of the device, so no CdS signal was found in the bare CZTSe film.

To obtain a better understanding of the inhomogeneity of the CdS layer on the CZTSe device surface, a set of 2-dimensional imaging and mapping techniques were applied to examine a single $20\ \mu\text{m} \times 20\ \mu\text{m}$ area on M3599_23 surface. Fig. 3.7 (a) shows the optical image, acquired with a 100x optical lens, of the examined square area containing a bright region of a few micrometers at its center and some scattered dark spots. The SEM image in Fig. 3.7 (b) further confirms the variation in surface morphology. Extra height of the bright region is estimated to be $1 - 1.5\ \mu\text{m}$ according to the AFM surface profile, shown in Fig. 3.7 (g). An aluminum mirror with its reflectance data provided by the vendor was used as a reference to obtain the reflectance mapping shown in Fig. 3.7 (c). The reflectance mapping shows that the bright CdS rich region is much more reflective than the general area, whereas the dark spots are less reflective than the rest area, which is in good agreement with the optical image since both of them are resulted from reflection. Dark spots with less reflectance highlighted with yellow circles are matched with the dark CdS rich spots in the optical image. Raman and PL mappings were performed with $\sim 200\ \mu\text{W}$ power ($\sim 4.9 \times 10^4\ \text{W}/\text{cm}^2$) of a 532 nm laser. Both Raman (monitored at $303\ \text{cm}^{-1}$) and PL (monitored at 1.73 eV) reveal clearly stronger signals from the bright region than the general area, as shown in Fig. 3.7 (d) and (e). As expected and indeed observed in Fig. 3.7 (f), the CdS rich regions including the large bright island and scattered black spots yield much smaller photocurrent, reduced by as much as a factor of 2, than the general area. Yellow circles in LBIC mapping correlates with the dark spots in the optical images. By comparing Fig. 3.7 (c) and (f), one can find the general anti-correlation between the

reflectance and LBIC mappings. Lower current from the CdS rich region indicates the potential to optimize the thickness of CdS layer to further improve the device performance.

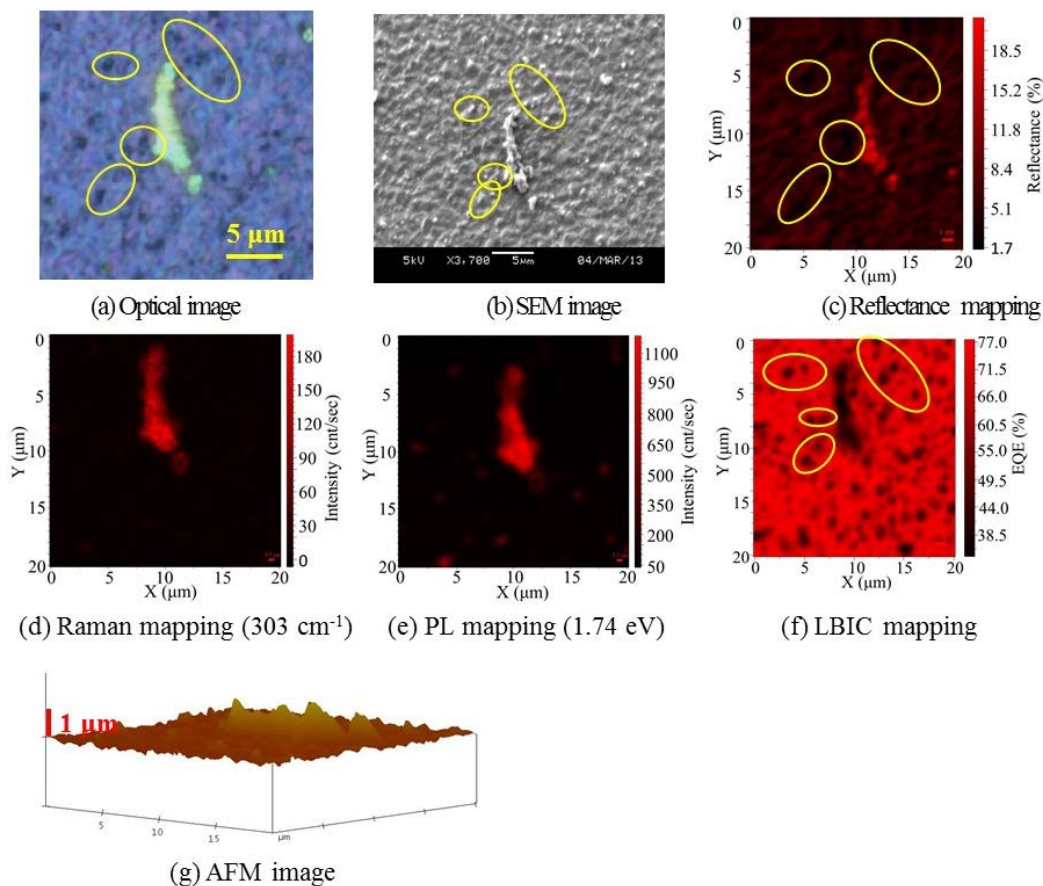


Figure 3.7: 2-Dimensional imaging and mapping result measured from M3599_23 device surface.

3.4. LBIC Contrast Reversal with Varying Illumination Density

Unintended CdS layer thickness fluctuation of CZTSe device offers an opportunity for us to study the microscopic scale inhomogeneity of CdS layer on device performance with minimal variation over many other possible growth parameters and device processing conditions. Two representative high and low laser powers were used to generate the photocurrent. At the low power level, the microscopically averaged EQE is comparable to that

from the macroscopic probe; while at the high power level, the general area shows significant EQE degradation, but the power is not too high to cause permanent damage to the material. All the mapping data were collected from the same area shown in Fig. 3.7 (a).

Reflectance and LBIC mapping measured with 532 nm laser at different laser power levels together with their histogram are shown in Fig. 3.8. The reflectance mapping was obtained with ~ 18 pW ($\sim 4.4 \times 10^{-3}$ W/cm²), showing a maximum reflectivity around $\sim 21\%$ at the CdS bright region, and a minimum reflectivity around $\sim 1.5\%$ at the dark spots. The average reflectance of the mapping area is about 5.3% (not including the large CdS island), which is much larger than the macroscopic specular reflectance from the device surface, $\sim 0.85\%$ at 532 nm. This is mainly due to the roughness of the sample surface which leads to significant diffuse reflectance or scattering in the macroscopic measurement. However, in the microscopic case, with the use of a high NA objective lens, we were able to capture majority of the scattered light, yielding a much higher reflectance that is in fact a more accurate measure of the actual reflectance loss.

For the LBIC data, at the lower power level of ~ 2 μ W with 532 nm laser, the device showed a rather high average EQE about $67.9 \pm 0.3\%$ (averaged over the entire mapping area), varying from 34.3% to 77.6%. The average EQE is consistent with the macroscopic data which is 81% for 532 nm laser from a similar device [44]. The somewhat lower EQE under local excitation is understandable, because carrier lateral diffusion from the illumination site tends to reduce the carrier collection efficiency along the vertical direction [177]. Histogram plot shows that the general area which represents the major part of the mapping area yields EQEs higher than 70%. However, the large CdS rich island and scattered CdS spots only yield EQE about 40% – 60%, becoming the dark regions in the

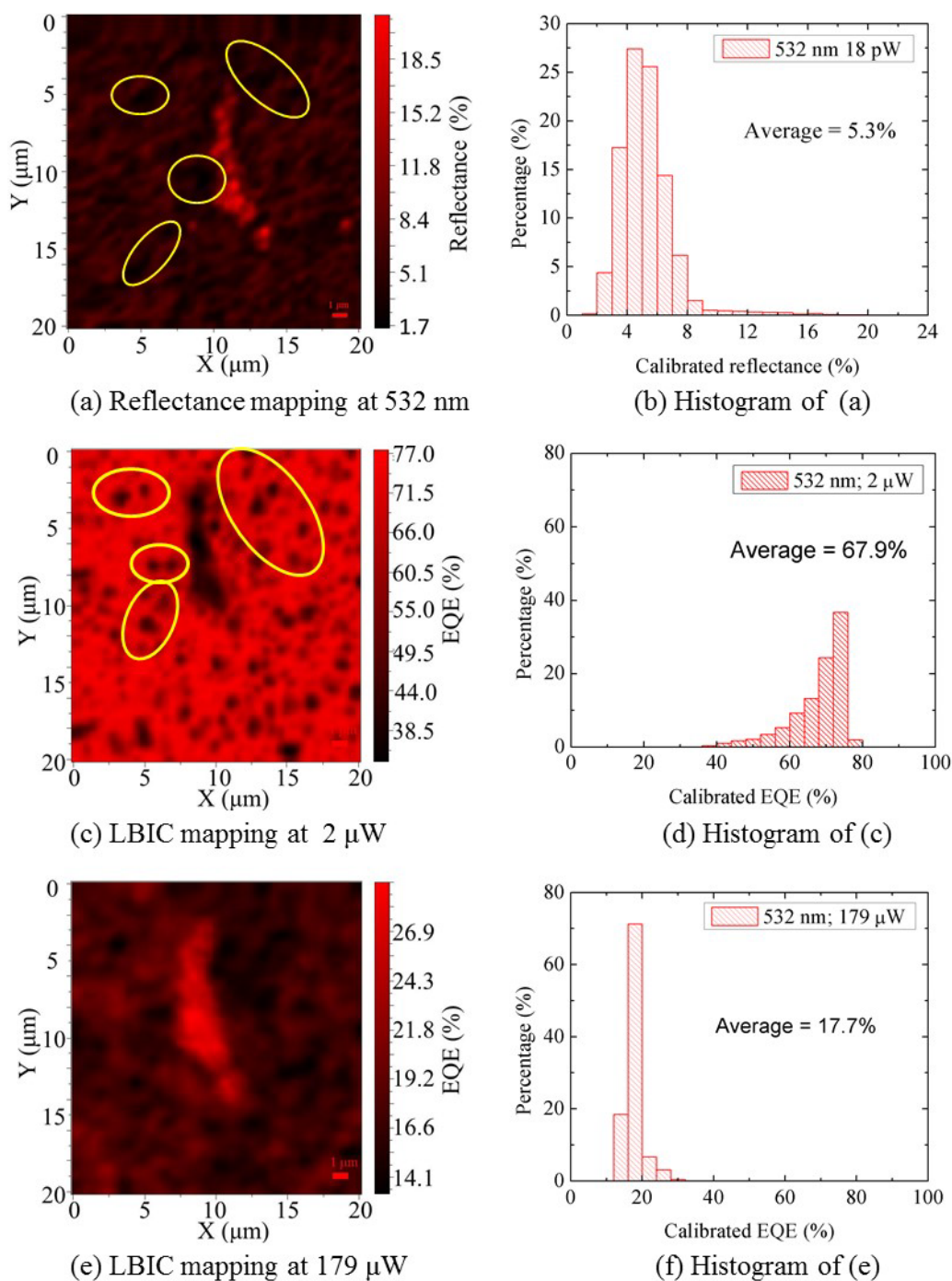


Figure 3.8: Reflectance and LBIC mapping with 532 nm laser at low and high power levels for CZTSe device M3599_23.

lower power level LBIC mapping as shown in Fig. 3.8 (c). The statistical data of Fig. 3.8 (c) reveal that a maximum EQE about 78% was achieved from some device areas, which is about ~16% larger than the average value. This finding suggests that if the device were made uniform like the best area throughout the whole device, the energy conversion efficiency could potentially be significantly higher. Because the open circuit voltage is also expected to increase slightly with the increase in the short-circuit current, the overall efficiency improvement could be as much as 20% at this wavelength.

For the LBIC mapping results shown in Fig. 3.8 (e) obtained at the high power level of $\sim 179 \mu\text{W}$, the average EQE drops drastically to $17.7 \pm 2.3\%$. EQE from the general area now drops to less than 20%, while the EQE from the CdS rich region is about 20% – 30%. Such relative change in EQEs leads to the reversal of the LBIC contrast as shown in Fig. 3.8 (c) and (e). Similar reflectance and LBIC mapping were also performed at the same area with a 633 nm laser. In the 633 nm laser reflectance mapping, although the reflectance contrast between the CdS rich region and general area is not as strong as that in the 532 nm reflectance mapping, the bright CdS island still shows higher reflectance than the general area, and the scattered spots with lower reflectance in yellow circles also matches to the scattered dark spots in optical image. Measuring at $0.75 \mu\text{W}$ (the low power level), the overall average EQE is about 87.4%, which is very close to the macroscopic data of ~90% for a similar device [44]. At the high power level, EQE from general area drops from ~90% to ~25%. However, the reduction at the CdS island is only from 70% to 40%, which also leads to the reversal of the LBIC contrast, as evident between Fig. 3.9 (c) and (e). Clearly, the CdS rich regions is more immune to EQE droop when illuminated with higher laser powers, although these regions have lower initial EQEs at lower power level. One possible

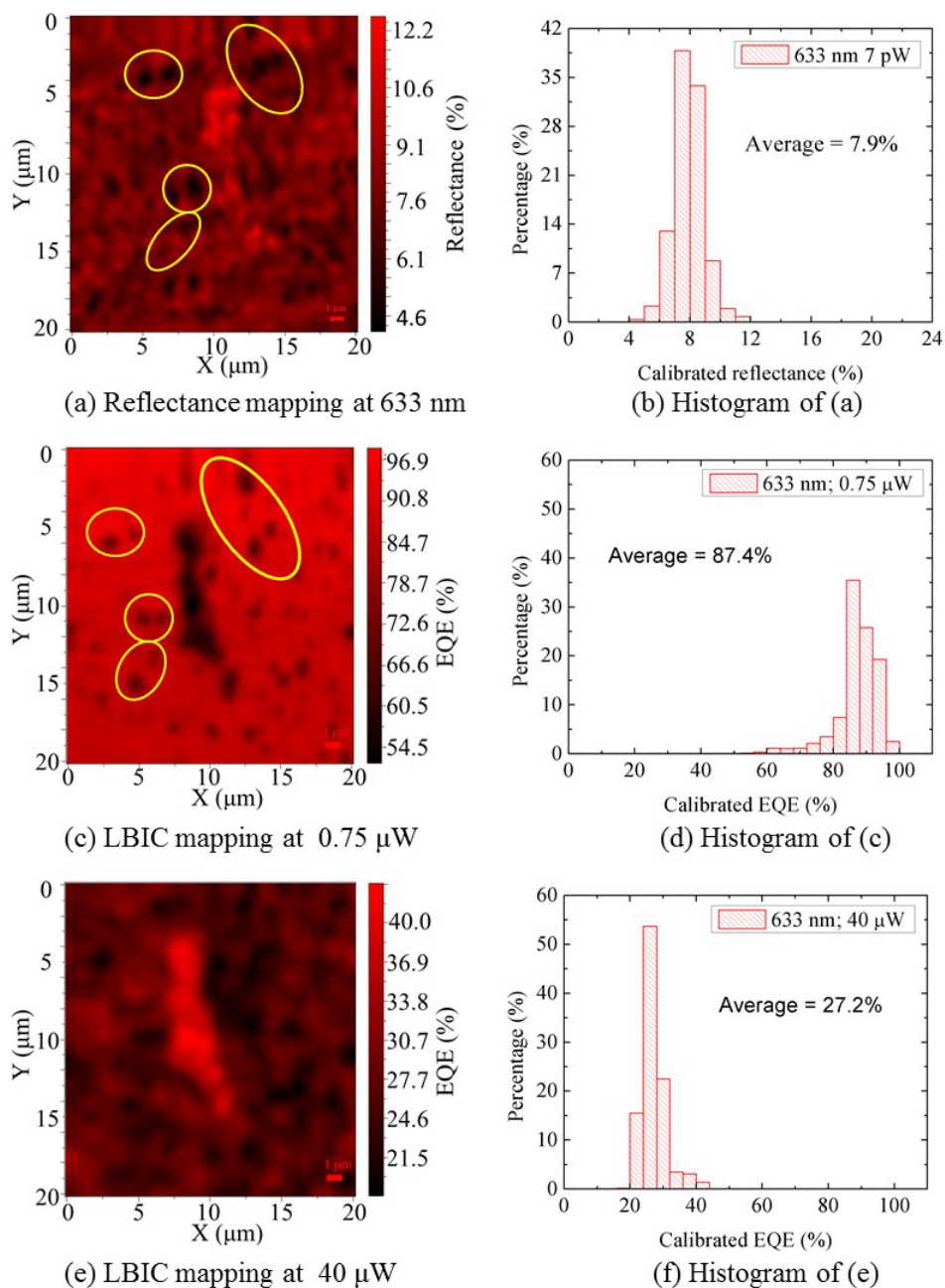


Figure 3.9: Reflectance and LBIC mapping with 633 nm laser at low and high power levels for CZTSe device M3599_23.

mechanism could be the electronic structure of the CZTSe/CdS heterojunction, such as the effective barrier height, depends sensitively on the CdS layer thickness. Undesirable CdS properties such as poor carrier transport of the polycrystalline phase, higher reflectivity and

residual absorption near the band gap are likely causing lower initial EQEs of the CdS rich regions. These issues could, in principle, be mitigated or improved to allow the adoption of thicker CdS layer, in particular for high illumination applications either in concentrated PV or photo-detection. By comparing the mapping with 532 nm laser and 633 nm laser, one may notice that the thicker CdS layer affects the device performance more at 532 nm than 633 nm, for example, the bright region reflects about three times more light than the general area with 532 nm, whereas the reflectance of the bright region is only about 1.5 times of the general area reflectance, which could be directly related to the larger CdS refractive index at 532 nm near the its bandgap. The LBIC contrast between the CdS rich region and the general area is also stronger with 532 nm laser than that of 633 nm laser.

I-V characteristic also offer a direct evaluation of PV material with short circuit current (I_{sc}) and open circuit voltage (V_{oc}). In Fig. 3. 10, local I-V curves from three different types of spots were measured with varying laser power, $\sim 25 \mu\text{W}$ and $\sim 200 \mu\text{W}$. At $25 \mu\text{W}$, with an I_{sc} about $6.8 \mu\text{A}$ and V_{oc} at 6.9 mV , the general spot gives the largest conversion efficiency which is almost twice as large as the efficiency of the bright spot. However, at $200 \mu\text{W}$, the same bright spot exceeds the general spot by 29% in I_{sc} and 60% in V_{oc} . And the local conversion efficiency of bright spot becomes twice of the general spot. The dark spot also surpass the general spot in I_{sc} , V_{oc} and efficiency. The changes in I-V curves from three types of spots is consistent with LBIC mapping data at different laser power levels. Although I_{sc} in microscopic probe is similar with those measured under large area illumination under the same power, the V_{oc} and fill factor (FF) are substantially lower than the macroscopic measurement numbers, which results in low observed cell efficiencies values in the local I-V tests. When measuring local I-V curves, the external

bias is applied across the whole device area of which the most is dark, and thus the locally generated photocurrent is mostly cancelled by the forward current passing through the non-illuminated area in the opposite direction, leading to a very low V_{oc} under tightly focused local excitation condition. Therefore, the efficiencies derived above are not the real efficiencies of the local regions under illumination, but only used to serve as qualitative measures of the change.

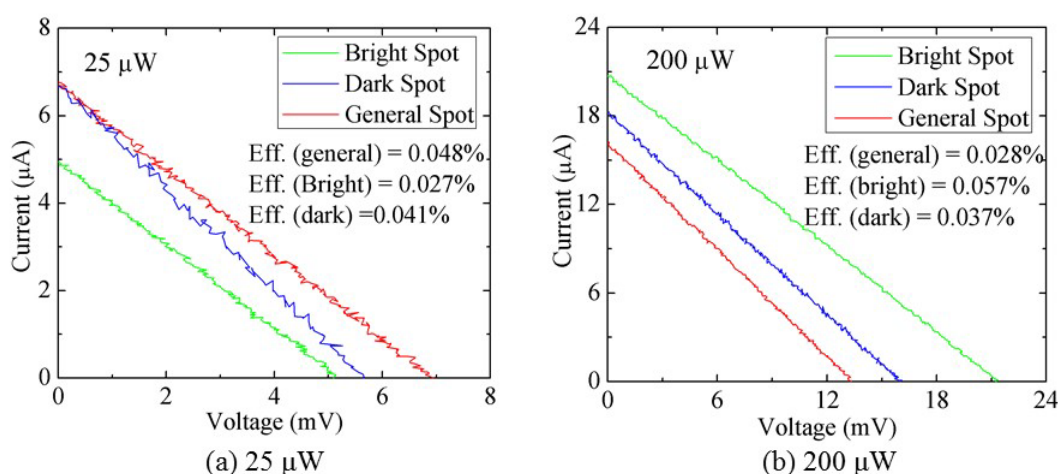


Figure 3.10: I-V curves of three types of regions with 532 nm laser at low and high power levels.

One could in principle subtract the dark current contribution from the non-illuminated area to recover the I-V curve of the illuminated site. I-V curves from another set of three types of spots on M3599_23 were measured at $179 \mu\text{W}$, as the dashed lines shown in Fig. 3.11. Similar with Fig. 3.10, the directly measured curves also showed very small V_{oc} , fill factors and efficiencies for all the three spots. By subtracting dark I-V curves obtained from the same cell, the corrected I-V curves were shown as solid curves in Fig. 3.11. The fill factors were increased to 46.3% for the general spot, 59.4% for the dark spot, and 56.5% for the bright spot, which are reasonably close to macroscopic measurement of 65%. The

efficiencies (given in the figure) are lower than the macroscopic efficiency measured under much lower illumination density, but the bright region yields the highest efficiency. This subtraction scheme implicitly assumes the laser illuminated area is much smaller than the overall device area that includes the illuminated site. The local I-V could be more accurately obtained by using a modulated laser beam and lock-in detection technique.

The different changes in EQE, I_{sc} , V_{oc} and efficiency between the CdS rich region and general area under different illumination conditions also suggest the potential of the device to operate at a higher illumination density.

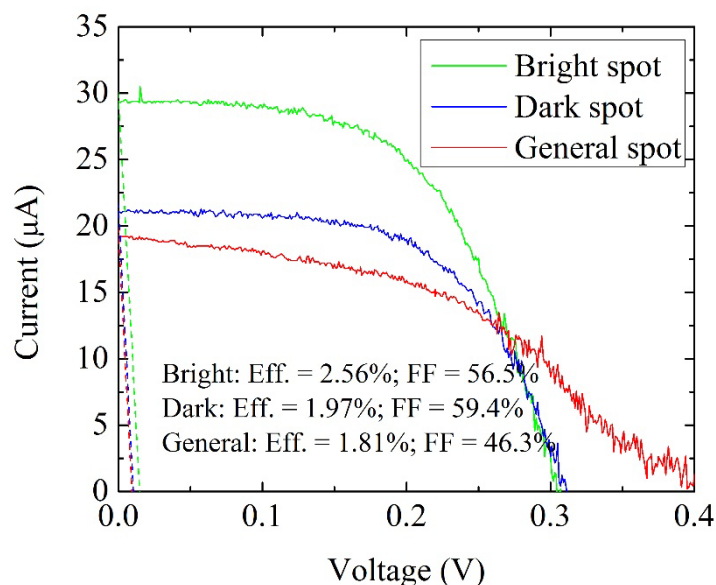


Figure 3.11: Corrected IV curves from three types of spots.

Similar LBIC contrast reversal was also observed from other CZTSe devices, for example, the LBIC mappings at different laser power levels obtained from M3602_22 surface shown in Fig. 3.12. The two bright spots within the mapping area give lower EQE when illuminated by $\sim 2 \mu\text{W}$ in Fig. 3.12 (b). Besides, the inhomogeneity of the film was revealed by the scattered dark spots with lower EQEs over the mapped area. When the

illuminating laser power was increased to $\sim 179 \mu\text{W}$, one region with obvious higher photo-current than the general area appeared, and it matched the position and shape of the upper bright spot in the optical image of Fig. 3. 12 (a). The EQE value from the smaller bright spot was comparable to or slightly larger than that of the general area. Multiple similar LBIC mappings were performed with multiple CZTSe devices. In general, the LBIC contrast reversal observed from M3599_23 is more significant than from other samples. Although the exact thickness of each CdS rich region was not measured, regions with thicker CdS may appear brighter in the optical image and show stronger Raman signal. Stronger LBIC contrast reversal was observed from regions with thicker CdS layer. In other words, the degree of the LBIC contrast reversal between the CdS rich region and general areas at least depends partially on the thickness of CdS.

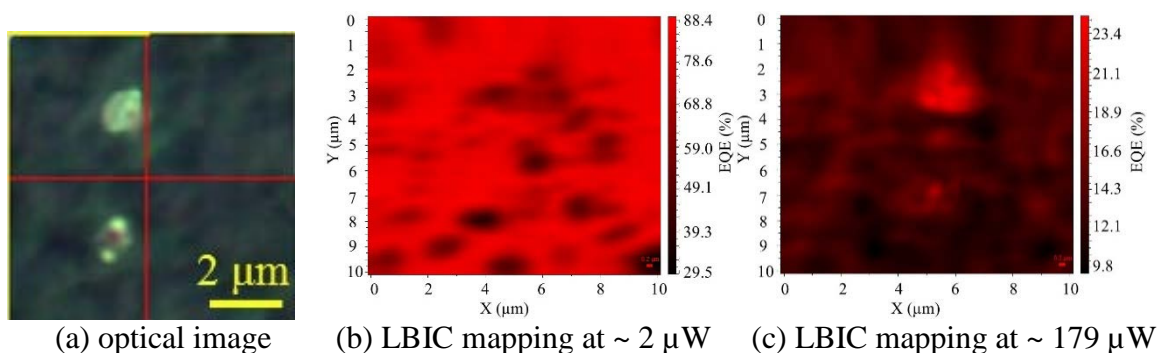
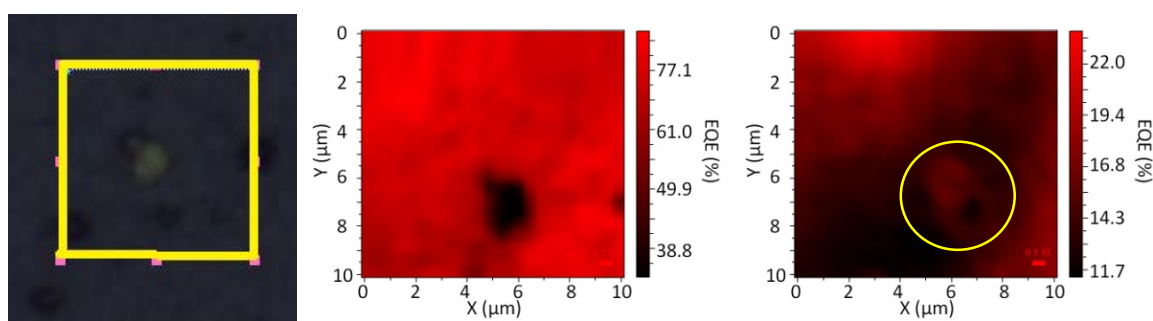


Figure 3.12: LBIC mapping with different 532 nm laser power levels obtained from M3602_22.

As the parent structure of the CZTSSe film, the similar phenomenon might also be expected for CIGS solar cells. One CIGS cell has been tested. On this cell, only a few CdS-rich spots were found on the CIGS sample, as indicated by the strength of CdS Raman signal. LBIC mappings were performed within an area shown in Fig. 3. 13 (a) on this CIGS sample. At the lower power level, the EQE from the CdS rich region is about half of that

from the general area. At $\sim 179 \mu\text{W}$ illumination, the CdS rich region seems to show much smaller change than the surrounding area, and it appears to be brighter in Fig. 3.13 (b). But no clear LBIC contrast reversal was found with the CdS rich region generating similar EQE with its neighbor regions. It is possible that the CdS layer is not thick enough to introduce the LBIC contrast reversal; or due to different band alignment and other factors, thickness of CdS layer does not affect the EQE in CIGS cell as much as in CZTSe cell. Fig. 3.13 (c) also shows the EQE droop in the CIGS is not uniform itself, though not CdS related. IV curves from the CdS rich spot and general spot were also measured at $200 \mu\text{W}$ shown in Fig. 3.14. I_{sc} from bright spot is about 12% less than I_{sc} of the general spot, and V_{oc} is about 4% less. Energy conversion efficiency of the general spot is also larger than that of the bright spot. Although the V_{oc} and efficiency of local I-V curves in Figs. 3.10 (b) and 3.14 are not the actual values of the device. One may still note the significant difference in V_{oc} between the CIGS and CZTSe cell. Low V_{oc} in CZTSSe cells is the primary hurdle limiting its performance compared with CIGS cells [63].



(a) optical image (b) LBIC mapping at $\sim 2 \mu\text{W}$ (c) LBIC mapping at $\sim 179 \mu\text{W}$
 Figure 3.13: LBIC mapping with different 532 nm laser power levels obtained from a CIGS cell.

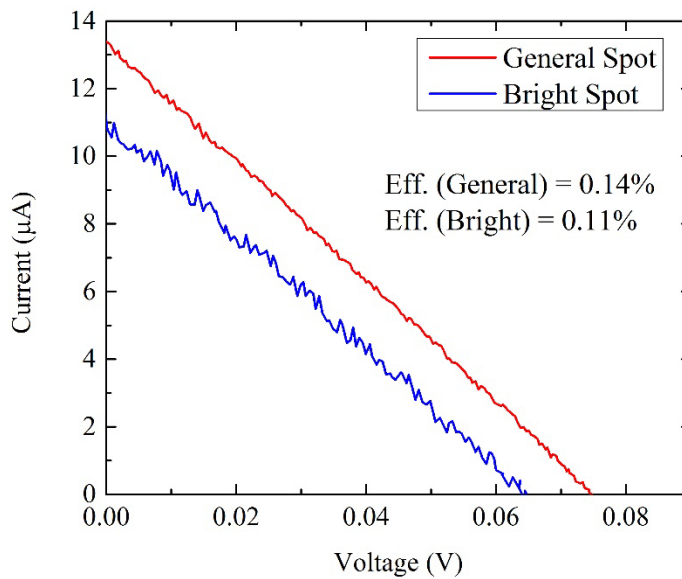


Figure 3.14: I-V curves of bright and general spot from a CIGS device with 532 nm laser at high power level.

3.5. Summary

CZTS Raman modes at 144.5, 165.9, 250.5, 285.3, 345.2, 365.2 cm^{-1} together with the dominant phase at 338.4 cm^{-1} and its second order mode at 671.5 cm^{-1} were observed by micro-Raman spectroscopy. CZTSe Raman lines were detected at 172, 196 and 233 cm^{-1} . Secondary phase such as SnSe and ZnSe were also found from the film.

Three distinctly different types of regions were found on CZTSe device samples: bright, dark and general area. Raman modes of CZTSe from the device surface are similar with those observed from the bare film sample in terms of both peak position and intensity. However, a 303 cm^{-1} Raman peak was also detected from the finished device and this peak was found strongly enhanced at the dark and bright spot together with its second order peak at 603 cm^{-1} . A broad PL band near 1.73 eV was observed from both dark and bright spot, which is much higher than the bandgap of CZTSe. Both the 303 cm^{-1} Raman mode and the 1.73 eV PL band were originated from the polycrystalline CdS window layer. By

comparing the CdS Raman and PL intensities from different types of spots, we have concluded that CdS is thickest at the bright spot and thinnest in the general area.

Multiple spatially resolved techniques were applied including micro-Raman, PL, LBIC, reflectance mapping, SEM and AFM to study the impact of inhomogeneity in CdS thickness on CZTSe device performance. SEM and AFM images of a CdS rich island confirm the surface morphology fluctuation, and reveal that the height of the extra CdS layer varies from 1 μm to 1.5 μm for the examined island. The bright spots with most CdS were found substantially more reflective than the general area, while the dark spots reflect less light than the general region, which is consistent with its optical image. Raman and PL mapping further confirm that the bright spot is rich in CdS with the strongest signal regions share similar shape and position with the bright islands in the optical image. In general, a thinner CdS layer is expected in the thin-film solar cell to reduce resistance. The LBIC mapping reveals lower EQE from the CdS rich regions when illuminated with low laser power level.

More interesting result comes from the laser power dependence of the LBIC mapping data. Both 532 nm and 633 nm laser were used to excite photo-current. For both lasers at low power level, CdS rich regions show about 50% lower EQE from the general area. When excited by high power level, the general area experienced drastically reduction in EQE. However, the CdS rich regions are more immune to the EQE droop due to high illumination density, leading to the LBIC contrast reversal when using low and high laser power illumination. The thicker the CdS layer is, the stronger LBIC contrast reversal can be observed from CZTSe devices. The local I-V characteristic proves the CdS rich spot exceeding the general spot in I_{sc} , V_{oc} and efficiency. These findings on one hand point out

the possibility of increasing the cell efficiency by improving the microscopic uniformity of the CdS window layer, and on the other hand, suggest the potential to fabricate CZTSe and related thin-film solar cells or photo-diodes for concentrated PV and photo-detection.

The LBIC mapping, in conjunction with other techniques, such as SEM, AFM, reflectance, local I-V measurement, can be a very useful technique to predict the potential for device performance.

CHAPTER 4: RAMAN STUDIES OF THE CZTSE SAMPLES PREPARED BY DIFFERENT METHODS

4.1. Introduction

Similar to its parent CIGS, CZT(S,Se) phase also has a narrow region of phase stability in which the device quality material can be synthesized without major adverse effects of secondary phases. Chen et al. [54] have predicted that the pure CZTS can only be grown in a very small regions (around point P in Fig. 4.1) according to their phase diagram calculations. Olekseyuk et al. [57] experimentally demonstrated the complicated phase diagram in the pseudo-ternary $\text{Cu}_2\text{S-ZnS-SnS}_2$ system from X-ray structural analysis data. The single phase CZTS is confined within a small region marked by 1 in Fig. 4.2. The formation of binary and ternary secondary phases including $\text{Zn}_x\text{S(Se)}$, $\text{Cu}_x\text{S(Se)}$, $\text{Sn}_x\text{S(Se)}$ and $\text{Cu}_x\text{SnS(Se)}_y$ are often observed in CZT(S,Se) films. Usually, film quality, defect formation and secondary phase formation are coupled [63]. The presence of these secondary phases has been assumed to contribute to lowering the energy conversion efficiency of the solar cell. For example, Cu-Sn-S clusters could act as recombination centers, resulting in a lower open circuit voltage; Cu_{2-x}S could even short the device; and ZnS may reduce the volume of the useful material and absorb the shorter wavelengths and lower EQEs when present at the film surface [71]. Achieving a high quality film requires a higher degree of understanding and control of the CZT(S, Se) phase space. Detection of secondary phases will guide how to improve the growth method for the CZT(S, Se) thin film. Identifying secondary phases using only XRD in CZT(S, Se) is not as easy as in CIGS

because kesterite CZTS shares multiple peaks with cubic ZnS and Cu_2SnS_3 [178]. Raman spectroscopy is a powerful characterization method to reveal vibrational signatures of CZT(S, Se) and especially of secondary phases.

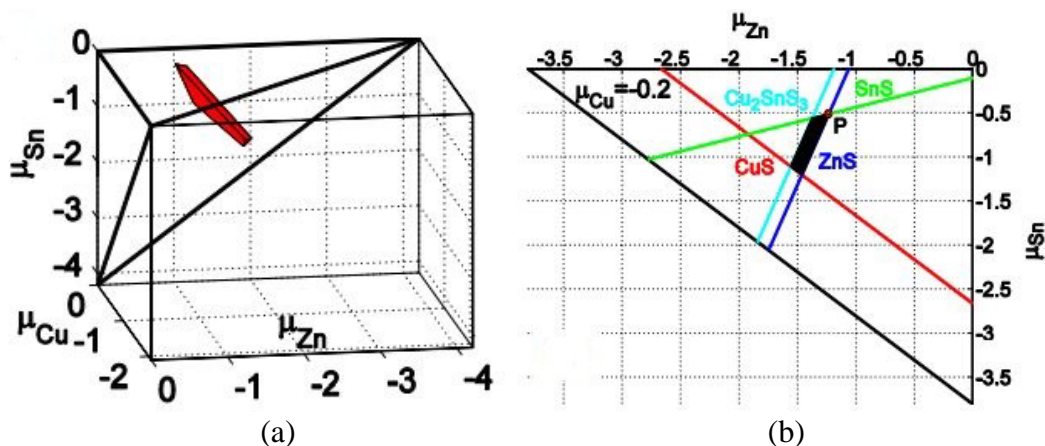


Figure 4.1: (a) Calculated polyhedron of the chemical potential region where CZTS is stable against formation of four elements and six competitive compounds. (b) At $\mu_{\text{Cu}} = -0.2$ eV, SnS (green line), ZnS (blue line), CuS (red line), and Cu_2SnS_3 (navy line) defines the allowed chemical potential region (black). Point P locates the region where all intrinsic defects have positive formation energies. [54]

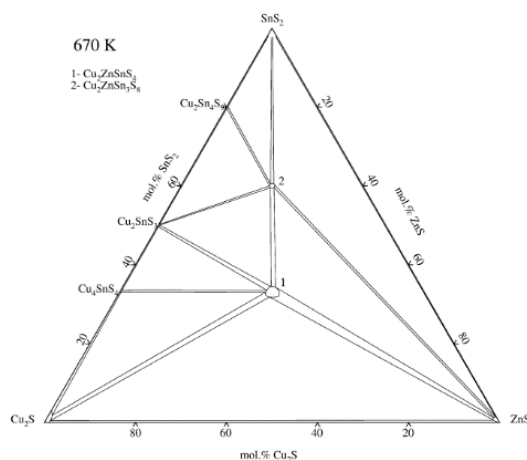


Figure 4.2: Pseudo-ternary phase diagram showing a very small central area where CZTS forms (marked as 1). [57]

CZTSe film is found to decompose at temperature higher than 350 °C. It has been reported that at high temperature, SnSe and Se evaporated and Cu_xSe and ZnSe are left behind based on X-ray analyses [130, 132, 179]. In this work, to examine the decomposition process in the CZTSe film, high laser power illumination is used in Raman spectroscopy study to introduce high local temperature in tested spots. Laser power dependence in Raman shift, peak width and intensity has been found significant in CZTSe films. Raman spectroscopy from room temperature to very high temperature (for example 800 ~ 900 °C) has also been performed to compare with high laser power Raman spectroscopy to estimate the local temperature change caused by the tightly focused high power excitation laser light. Both high laser power and high temperature Raman studies have been shown to be very effective tools for probing the structural differences of different complex alloys like CZTSe.

In this work we performed micro-Raman study on three CZTSe samples prepared by two different methods: one by a sputtering method and the other two by a co-evaporation method. These three films showed different changes in Raman spectra after being illuminated by high laser power or under high temperature condition. Raman spectroscopy was performed not only from front surface but also from cleaved edge. By comparing Raman spectra from different positions of the cleaved edge, we were able to achieve a better understanding of its composition depth profile, and the subtle difference between films prepared by the two methods. By heating the samples to different temperatures, we observed the phase change within the film from room temperature to 800/900 °C. Heated pieces were also examined after being cooled down to room temperature, different residue components have been found in the pieces being heated to different temperatures.

4.2. Raman Studies of CZTSe Samples From Front Surface

In this chapter, three CZTSe samples were measured: Bare CZTSe film CZTSe_97; Bare CZTSe film M3599_12 and CZTSe solar cell device M3602-21. For CZTSe_97, the CZTSe film was prepared by selenizing a metal stacks which compose of 300 nm Mo, 130 nm Zn, 155 nm Cu and 180 nm Sn sputtered on an Ashai PV 200 glass substrate. The film compositions are $[Zn]/[Sn] \cong 1.25$ and $[Cu]/([Zn]+[Sn]) \cong 0.85$, and the kesterite film is slightly thick than 1 μm . M3599_12 and M3602_21 were prepared via a co-evaporated method which has been described in Chapter 3. The film compositions of 3599_12 is $[Zn]/[Sn] \cong 1.32$ and $[Cu]/([Zn]+[Sn]) \cong 0.82$ and $[Zn]/[Sn] \cong 1.28$ and $[Cu]/([Zn]+[Sn]) \cong 0.87$ for M3602_21. Raman spectroscopy were performed at room temperature with 532 nm laser and 100x lens.

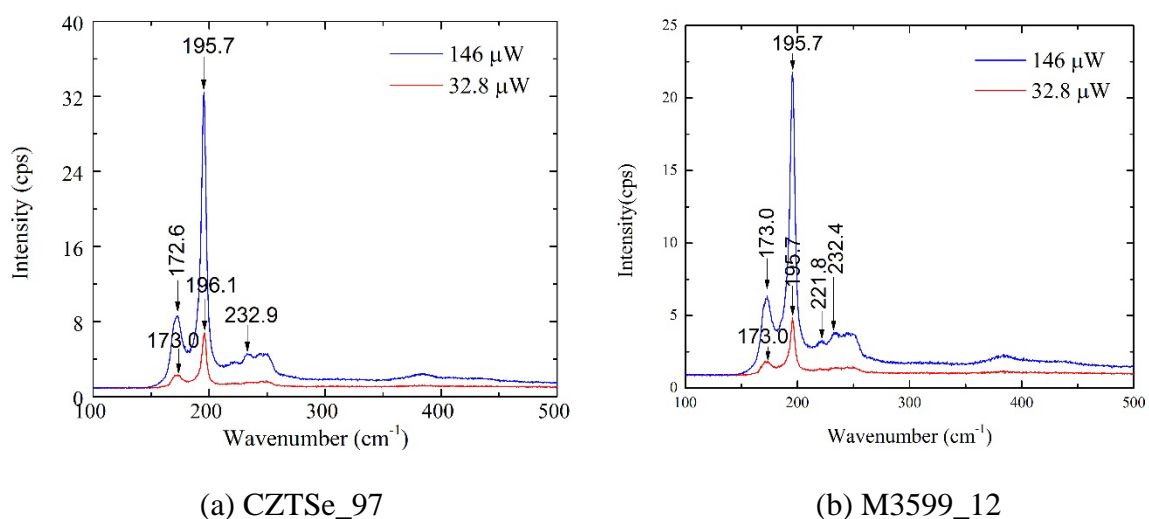


Figure 4.3: Raman spectra of bare CZTSe film samples measured from front surface at 32.8 μW and 146 μW .

In Fig. 4.3, Raman spectra from CZTSe_97 and M3599_12 surface were obtained with both 32.8 and 146 μW from the same sample point with no grating movement between

the two measurements. For sample CZTSe_97, CZTSe main Raman mode experienced a 0.4 cm^{-1} red shift when the laser power was increased from $32.8 \text{ }\mu\text{W}$ to $146 \text{ }\mu\text{W}$, but not obvious shift for M3599_12 bare film. The slight CZTSe Raman mode shift indicates a small heating effect was introduced for the sputtered sample under $146 \text{ }\mu\text{W}$ illumination. However, the power level was not too high to cause irreversible material change. The comparison suggests some subtle structural difference between the two samples, manifested in the difference in thermal conductivity.

Figure 4.4 illustrates typical Raman spectra from three CZTSe samples taken from their front surface with 0.146 mW laser power. All three samples showed two intense Raman peaks at $195 - 196 \text{ cm}^{-1}$ and $172 - 173 \text{ cm}^{-1}$, and a weak peak at $232 - 233 \text{ cm}^{-1}$ from CZTSe, since they are very close to the single crystal Raman scattering peaks at 196 , 173 and 231 cm^{-1} [42]. Except for the primary CZTSe single crystal Raman scattering peaks, we also found additional peaks at 221.8 , 222.7 , $243.9 \sim 245.2$ and $251 \sim 252.7 \text{ cm}^{-1}$ in all three samples. Besides, another 249.2 cm^{-1} peak was observed in M3599_12. Theoretical calculations have been performed to predict the possible CZTSe Raman modes in kesterite, stannite and PMCA structures [164, 180-182]. Here, the $221 \sim 223 \text{ cm}^{-1}$ is believed to be a transverse optical (TO) Raman mode in E symmetry from kesterite structure [164, 180, 181]. $244 \sim 245 \text{ cm}^{-1}$ was also reported to be CZTSe related both experimentally and theoretically [43, 53, 62]. The presence of secondary phase Cu_2SnSe_3 contributes to weak peaks located near 251 cm^{-1} [42]. Raman peak at 249 cm^{-1} in Fig. 4.4 is reported to be from ZnSe [62]. However, ZnSe peaks were observed at 253 cm^{-1} instead in most cases [169-171, 183, 184]. On the other hand, amorphous selenium (a-Se) was reported to displays a Raman feathers at $\sim 250 \text{ cm}^{-1}$ and a shoulder at $\sim 235 \text{ cm}^{-1}$ [185-188]. It is also

possible that selenium is present in CZTSe films since they were fabricated in a Se-rich ambient. A broad band from 140 to 150 cm^{-1} in all three spectra is from SnSe [167, 168]. Raman line near 303.6 cm^{-1} in Fig. 4.4 (c) is known to be from CdS [139], which is the window layer of the CZTSe solar device, as discussed in Chapter 3. The origin of the broad band ranging from 380 to 390 cm^{-1} is still unclear.

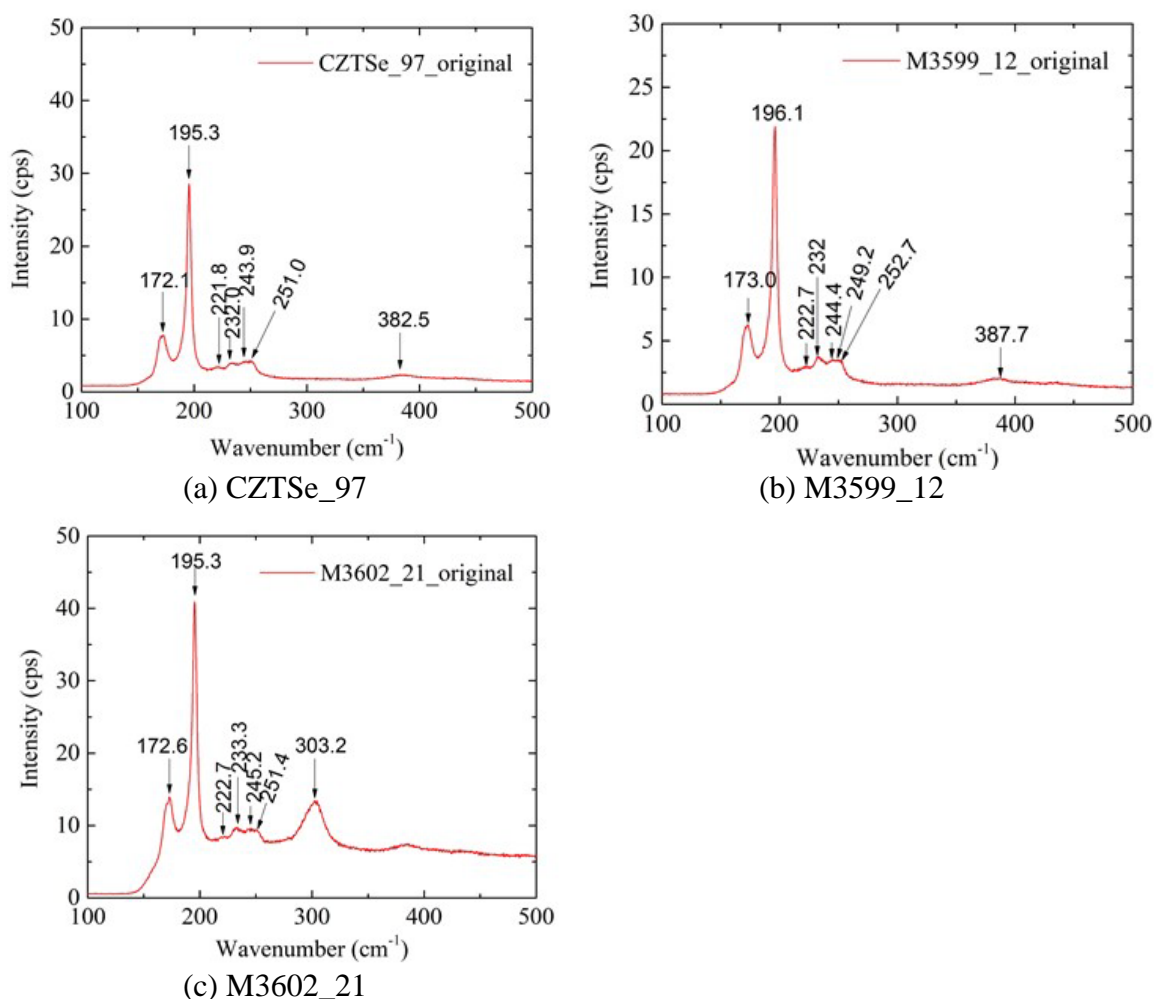


Figure 4.4: Raman spectra of three CZTSe samples measured from the front surface at 0.146 mW.

Ref. [189] indicated that Raman spectra taken at the same spot of the CZTSe absorber with different laser power (0.2 mW/micro spot, 0.5 mW/micro spot and 2.5 mW/micro spot)

were the same except for a change in background. However, in this work, we observed high laser power effect on CZTSe Raman scattering by comparing Raman spectra taken at the same spot before and after high power illumination. For each sample, after taking the Raman spectrum shown in Fig. 4.4 with 0.146 mW (3.5×10^4 W/cm²) laser power, we illuminated the same sample spot with 2.47 mW (3.6×10^5 W/cm²) for 100 seconds, then re-measured the Raman spectrum with 0.146 mW under the same conditions. After the higher power illumination, the illuminated spot showed some color change (becoming lighter under optical microscope), but no apparent ablation. The results for the three samples are shown in Fig. 4.5. The two main CZTSe peak at 195 or 196 cm⁻¹ and 171 – 172 cm⁻¹ experienced not only intensity reduction, but also red shift in all three samples. For example, 195.3 cm⁻¹ of CZTSe_97 CZTSe main peak shifts to 193 cm⁻¹, 172.1 cm⁻¹ to 171.7 cm⁻¹. Besides, some new peaks appeared after the high power illumination. In Fig. 4.5 (a), a new Raman peak at 242 cm⁻¹ is observed from CZTSe_97. This 242 cm⁻¹ matches A_{1g} Raman mode of MoSe₂ [190], although some people reported 242 cm⁻¹ also as a CZTSe Raman mode [191, 192]. For M3599_12 and M3602_21 in Fig. 4.5 (b) and (c), new peaks appeared at 234.7 and 235.1 cm⁻¹ which is close to reported Cu₂SnSe₃ Raman mode at 236 cm⁻¹ [42] and a-Se shoulder at 235 cm⁻¹.

The laser power was further increased to 4.5 mW (1.07×10^6 W/cm²) to illuminate the same spots for 36 seconds, then Raman data were collected again with 0.146 mW power. The intensity of the strongest CZTSe peak initially at 195 or 196 cm⁻¹ drops further for all three sample, but the peak position remains nearly the same as that after the first illumination except for in M3599_12 shifting further from 194.8 cm⁻¹ to 193.5 cm⁻¹. For CZTSe_97, as shown in Fig. 4.6 (a), the intensity of 193 cm⁻¹ peak is only 10% of its

original value before high power illumination, and the 172 cm^{-1} mode became a weak shoulder from 168 cm^{-1} to 178 cm^{-1} . In addition, a sharp and strong peak appears at 241.7

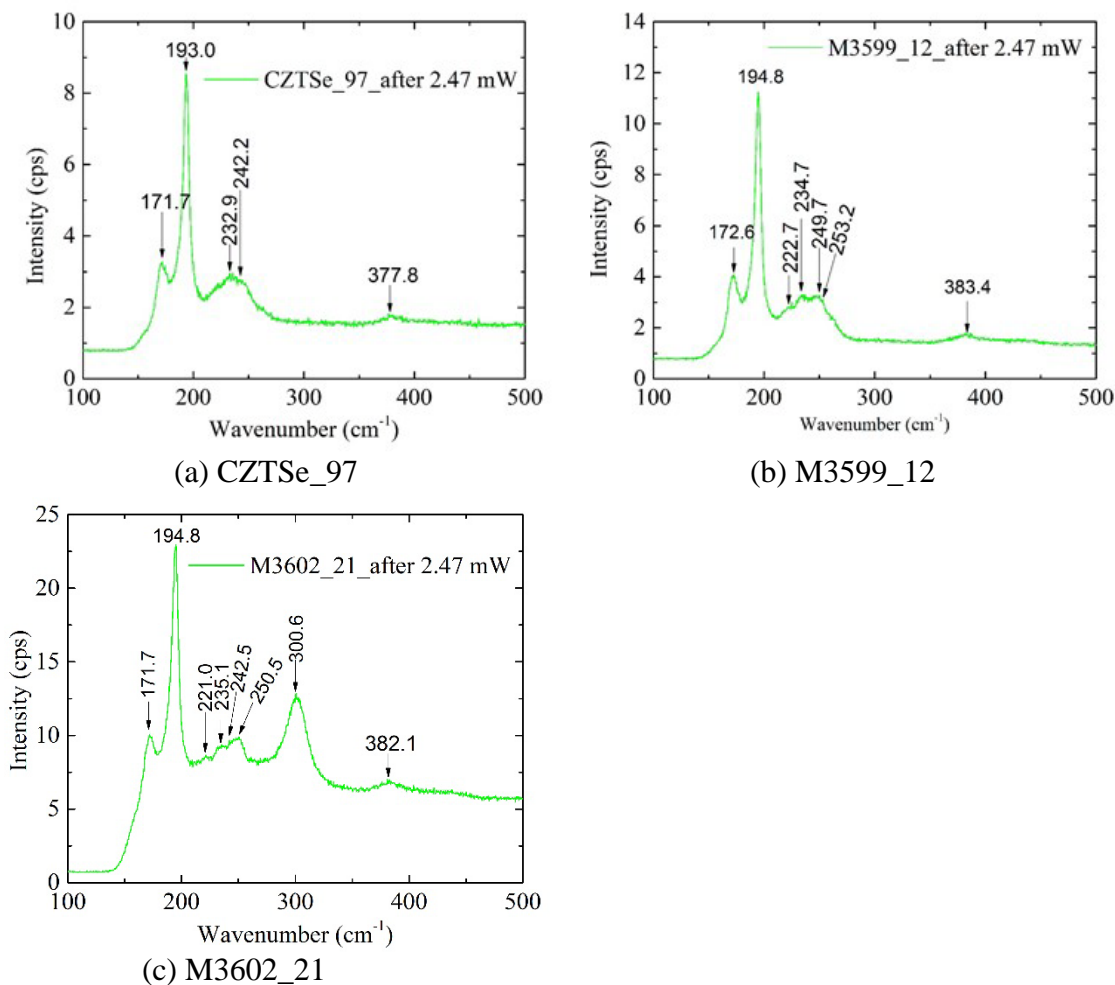


Figure 4.5: Raman spectra of three CZTSe samples after tested spots being illuminated by 2.47 mW.

cm^{-1} , which is enhanced from the 242 cm^{-1} peak in Fig. 4.5(a). In Fig. 4.14 as well as cleaved edge Raman study, this peak will be demonstrated as MoSe_2 coming from substrate-film boundary. After high power illumination, due to the intensity reduction of Raman mode from CZTSe layer which is above the substrate, the 242 cm^{-1} peak became prominent among the mesa-like band from $220 - 250\text{ cm}^{-1}$. Interestingly, the main CZTSe

peak intensity only dropped by a factor of four, and the $\sim 172\text{ cm}^{-1}$ CZTSe peak remains sharp in M3599_12 after the second higher power illumination. In addition, the 242 cm^{-1} peak do not appear in the other two co-evaporated samples measured at the same conditions as shown in Figs. 4.6 (b) and (c). CZTSe_97 and M3599_12 are both bare CZTSe film samples, one prepared by sputtering method and the other prepared via co-evaporation. Obviously, high temperature illumination brought more change to sputtered film in Raman spectrum, such as peak broadening, red shift and intensity reduction. In other words, the contrast between CZTSe_97 and M3599_12 suggests that the CZTSe structure prepared by co-evaporation seems to be more robust than what prepared by sputtering.

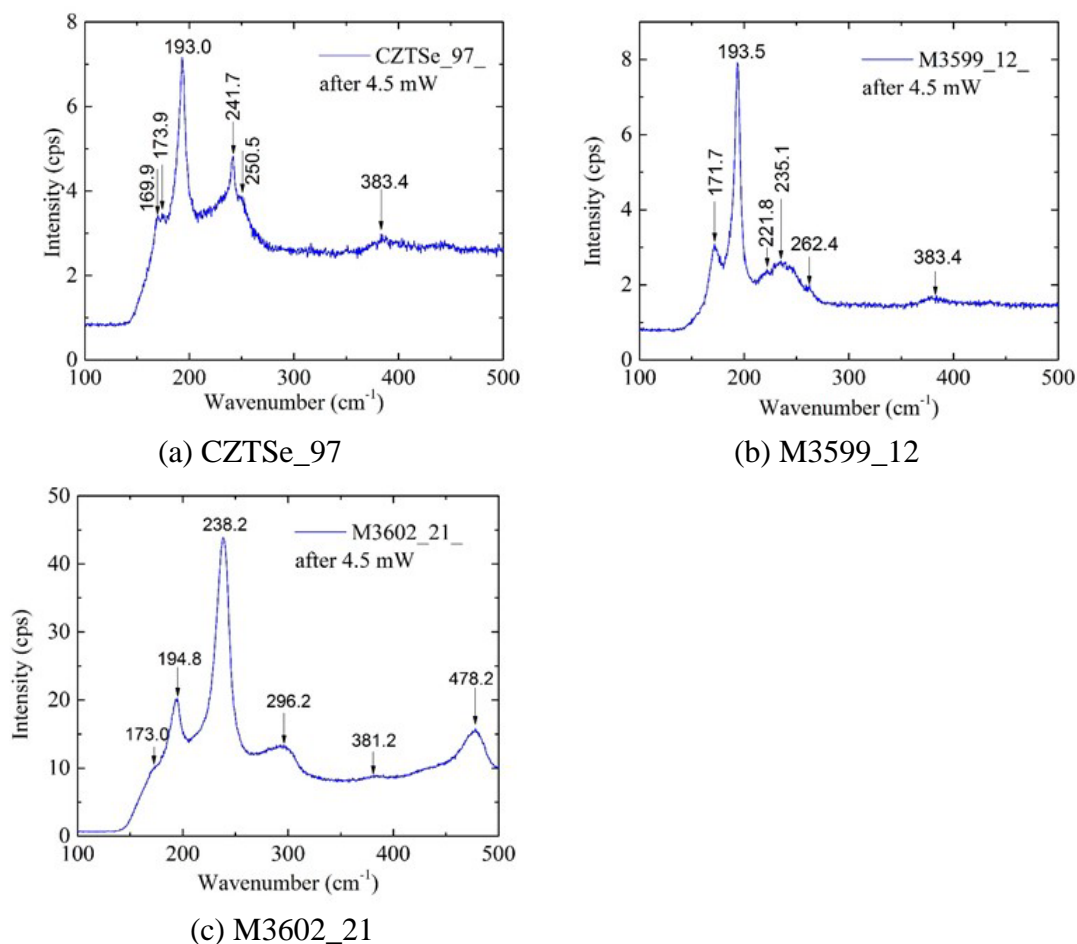


Figure 4.6: Raman spectra of three CZTSe samples after tested spots being illuminated by 4.5 mW.

For M3599_12, there is no significant further change after the second high power illumination compared to the first high power illumination, except a new weak Raman peak at 262.4 cm^{-1} . This new peak turns out to be Se-Se stretching mode of Se_2 ions in Cu_xSe_y [45, 193-195] coming from the periphery of the illuminated spot, which will be demonstrated in the Raman mapping of CZTSe sample surface near the illumination site. Instead of the mesa-like band which composed of multiple Raman peaks between 220 to 250 cm^{-1} , one strong sharp peak at 238.2 cm^{-1} and a possible second order peak at 478.2 cm^{-1} appeared, which is the most significant change happened in sample M3602_12 after the second high power illumination. The origin of these two peaks is believed as A_1 mode of trigonal selenium (t-Se) [185, 196]. In Ref. [185], a detailed description of phase transition from a-Se to t-Se due high laser power illumination is presented. As a result of the photocrystallization, a broad band at $\sim 250 \text{ cm}^{-1}$ and a shoulder at $\sim 235 \text{ cm}^{-1}$ observed in a-Se film became two resolved bands at 233 cm^{-1} and 237 cm^{-1} representing t-Se. This Raman feature transition matches our observation in M3602_21 before and after high laser power illumination, which indicates the possibility that a-Se existed in the as-deposited CZTSe film, and after high power illumination, the a-Se was nearly completely crystallized to t-Se, since no peak $\sim 250 \text{ cm}^{-1}$ was observed. One may notice that the intensity of $\sim 250 \text{ cm}^{-1}$ originally observed in CZTSe film was much smaller than the intensity of $\sim 238 \text{ cm}^{-1}$ appeared after high laser power illumination. It is possible that the CZTSe structure partially decomposed and generated more selenium, which contributed to the strong t-Se Raman mode. Similar change caused by high laser power illumination was also observed from other CZTSe device samples: M3599_23 and M3652_13. To conclude, changes in Raman spectra from all three CZTSe samples after higher power illumination indicated the

structural changes of the kesterite film and CZTSe partial decomposition. As a comparison, Fig. 4.7 gives Raman spectra collected from a Si sample before and after high power illumination. Even after 18.9 mW (4.5×10^6 W/cm²) illumination, the Si Raman spectrum looked almost the same with its original spectrum collected with 0.149 mW (3.5×10^4 W/cm²). Quaternary CZTSe is structurally not as robust as an elemental or binary semiconductor such as Si and GaAs. The contrast may also be related to the poorer thermal conductivity of the polycrystalline film.

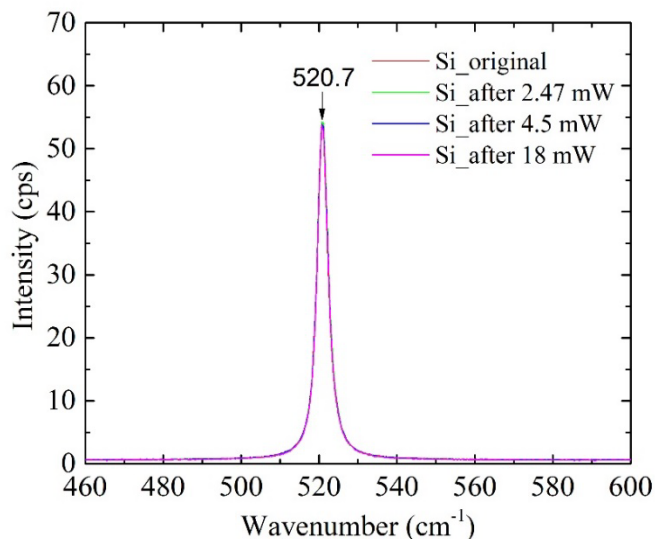


Figure 4.7: Si Raman spectra before and after high power illumination.

2D Raman mapping was performed to examine the spatial extension of the local heating effect caused by the high power illumination on CZTSe sample surface, as shown in Figs. 4.8 to 4.13. For each sample, one random spot from the sample surface was first illuminated by 2.47 mW for 100 seconds, Raman mapping was then acquired from a 5×5 μm (in Fig. 4.8) or 8×8 μm (in Figs. 4.9 to 4.13) area centered at the illuminated spot with 0.146 mW excitation laser power. Figs. 4.8 – 10 (a) shows the optical images of the

mapping areas. 1.47 mW laser illumination led to color change to all three illuminated spots, especially one can clearly see a halo surrounding the illuminated spot from M3599_12. In addition to two CZTSe Raman modes at $\sim 172\text{ cm}^{-1}$ and $\sim 196\text{ cm}^{-1}$ and the mesa-like band from 220 cm^{-1} to 250 cm^{-1} , another peak around $\sim 261\text{ cm}^{-1}$ was also observed in CZTSe_97 Raman mapping spectra. For each sample, Raman intensity mapping results of a narrow band centered at 196 cm^{-1} and 261 cm^{-1} are illustrated respectively in Figs. 4.8 to 4.10 (b) and (c). Dark circles in Figs. 4.8 – 10 (b) confirmed the intensity drop of the CZTSe main Raman mode at 196 cm^{-1} . For CZTSe_97, with the darkest $\sim 1\text{ }\mu\text{m}$ circle at the illumination site, a dark circle with diameter of $\sim 3\text{ }\mu\text{m}$ showed lower 196 cm^{-1} intensity, which is much larger than laser spot size $0.76\text{ }\mu\text{m}$. In addition, a ring which encloses the illuminated spot was found rich in Cu_xSe_y suggested by a strong Raman peak at 261 cm^{-1} , as shown in Fig. 4.8(c). On the other hand, 1.47 mW laser illumination only affected a range about $1.5\text{ }\mu\text{m}$ circle in M3599_12 and even less than $1\text{ }\mu\text{m}$ circle in M3602_21. The difference between CZTSe_97 and M3599_12 seems to suggest that the two nominally similar films might have different thermal conductivity, which might be correlated to the different responses in structural change mentioned above. We note that for M3602_21 the extra layers above CZTSe might improve the thermal conductivity of the structure as a whole, thus, showing less spatial extension. Besides, 261 cm^{-1} peak did not appear in either M3599_12 or M3602_21 mapping after being illuminated by 2.47 mW in Figs. 4.9 and 10 (c), which also suggests that CZTSe absorber prepared by sputtering method is more sensitive to high power illumination than film fabricated by co-evaporated method.

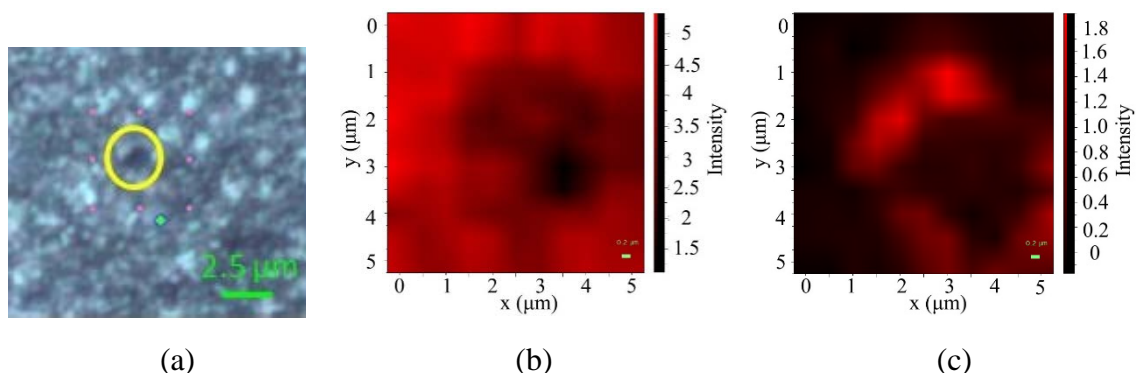


Figure 4.8: CZTSe_97 Raman mapping after one spot being illuminated by 2.47 mW for 100 s: (a) optical image of illuminated spot; (b) Raman mapping centered at 196 cm^{-1} ; (c) Raman mapping centered at 261 cm^{-1} .

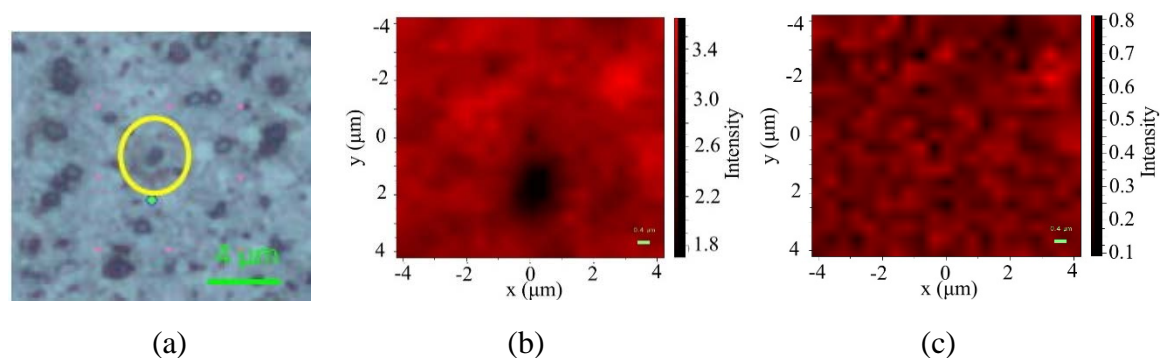


Figure 4.9: M3599_12 Raman mapping after one spot being illuminated by 2.47 mW for 100 s: (a) optical image of illuminated spot; (b) Raman mapping centered at 196 cm^{-1} ; (c) Raman mapping bang range $220 \sim 270\text{ cm}^{-1}$.

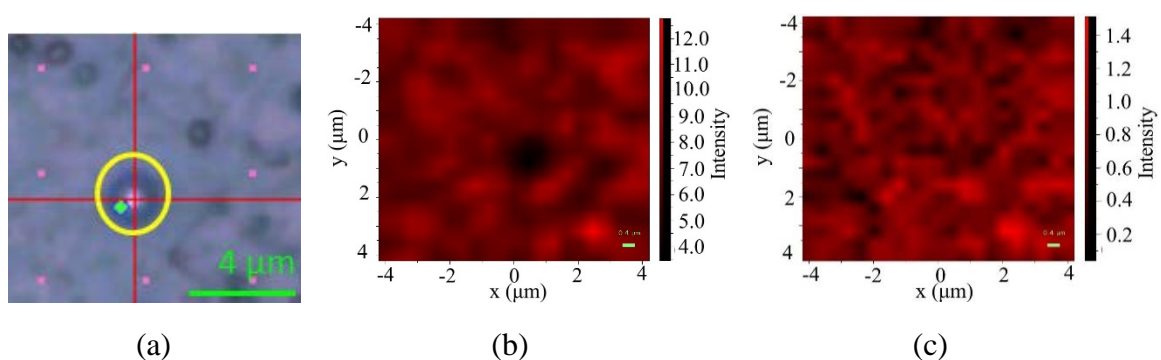


Figure 4.10: M3602_21 Raman mapping after one spot being illuminated by 2.47 mW for 100 s: (a) optical image of illuminated spot; (b) Raman mapping centered at 196 cm^{-1} ; (c) Raman mapping bang range $220 \sim 270\text{ cm}^{-1}$.

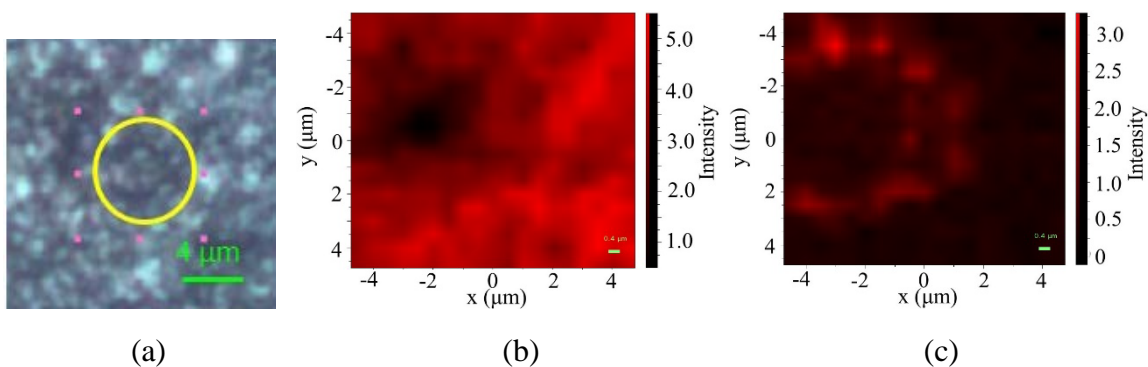


Figure 4.11: CZTSe_97 Raman mapping after one spot being illuminated by 4.5 mW for 36 s: (a) optical image of illuminated spot; (b) Raman mapping centered at 196 cm^{-1} ; (c) Raman mapping centered at 261 cm^{-1} .

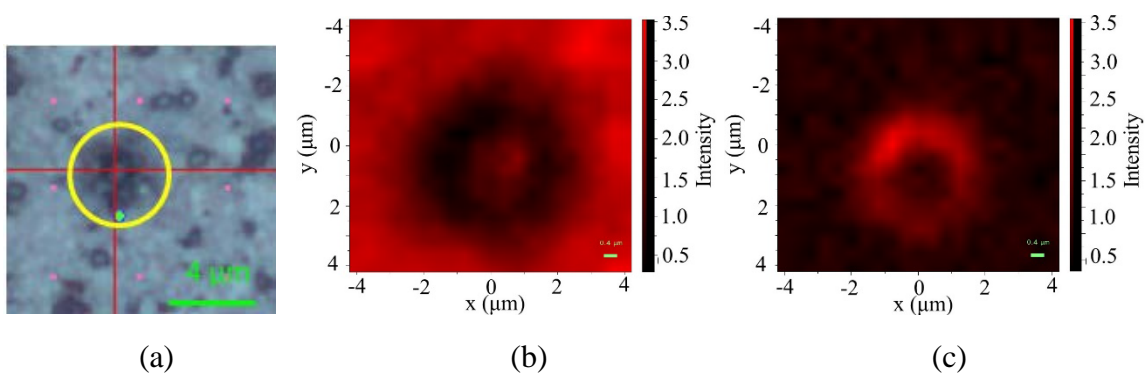


Figure 4.12: M3599_12 Raman mapping after one spot being illuminated by 4.5 mW for 36 s: (a) optical image of illuminated spot; (b) Raman mapping centered at 196 cm^{-1} ; (c) Raman mapping centered at 261 cm^{-1} .

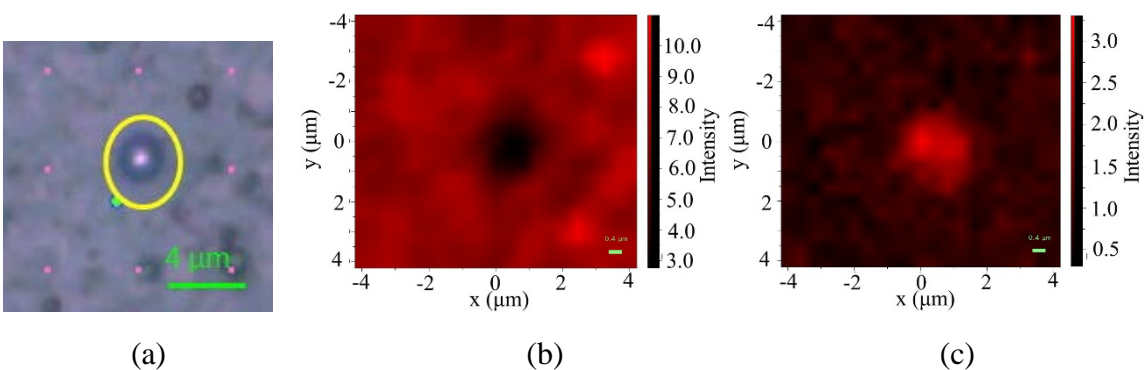
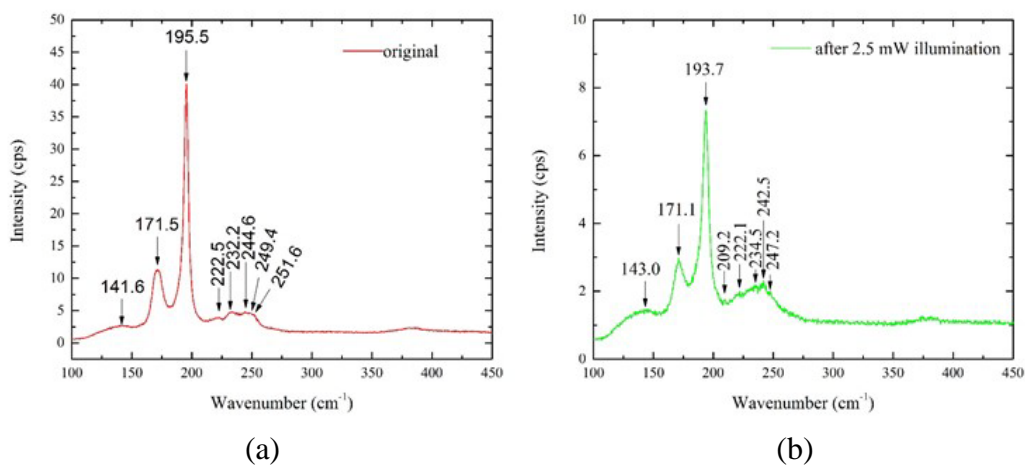


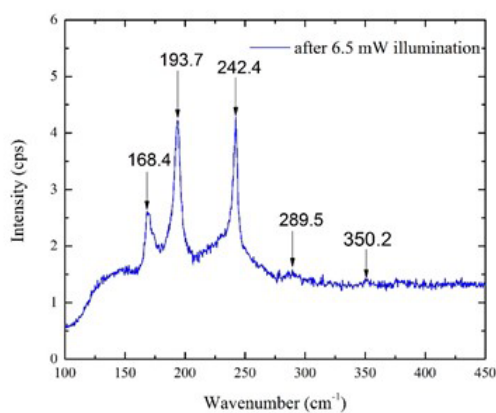
Figure 4.13: M3602_21 Raman mapping after one spot being illuminated by 4.5 mW for 36 s: (a) optical image of illuminated spot; (b) Raman mapping centered at 196 cm^{-1} ; (c) Raman mapping centered at 240 cm^{-1} .

When laser power was increased to 4.5 mW, the same spot was again illuminated for 36 seconds, and the same Raman mapping with low laser power (0.146 mW) was also performed at the same region. Optical images showed a larger affected region clearly in Figs 4.11 - 13 (a). Raman mapping in Fig. 4.11 (b) showed that the 196 cm^{-1} peak intensity of CZTSe_97 reduces in a circular region with a diameter larger than $6\text{ }\mu\text{m}$. The affected area of M3599_12 also enlarged to about $5\text{ }\mu\text{m}$ in diameter. For M3602_21, the affected area only has a diameter about $2\text{ }\mu\text{m}$. The extra layers of CZTSe solar cell device could possibly offer some extra protection to the CZTSe absorber. In the intensity map of the 261 cm^{-1} peak, a Cu_xSe_y rich ring still existed in CZTSe_97 as shown in Fig. 4.11 (c). But now a similar Cu_xSe_y ring was also observed in M3599_12 after it was illuminated by 4.5 mW. For M3602_21 in Fig. 4.13 (c) (map of 238 cm^{-1}), instead of a surrounding Cu_xSe_y rich ring, the illuminated spot was found to generate a strong Raman signal at $\sim 238\text{ cm}^{-1}$, which is consistent with previous single spot surface Raman result, Fig. 4.6 (c).

Due to the inhomogeneity of the absorber, there are spots from each sample which would generate additional new peaks after high power illumination. To illustrate this, compared with Figs. 4.4 – 6 (a), a broad band at $140\text{ } \sim\text{ } 149\text{ cm}^{-1}$, likely due to SnSe is observed from one CZTSe_97 spot in Fig. 4.14 (a). After 2.5 mW ($6.0 \times 10^5\text{ W/cm}^2$) illumination, besides the intensity drop and red shift of CZTSe Raman modes, Raman peaks at 242 cm^{-1} which is from MoSe_2 and a very weak peak at 209 cm^{-1} which is reported as stannite CZTSe mode were observed [182, 197]. When illumination laser power was further increased to 6.5 mW, the 172 cm^{-1} mode was replaced by a new Raman mode at 168.4 cm^{-1} with comparable intensity, and another sharp and strong peak appears at 242.3 cm^{-1} together with weak peaks at 289.5 cm^{-1} and 350.2 cm^{-1} . The 168.4 cm^{-1} mode was

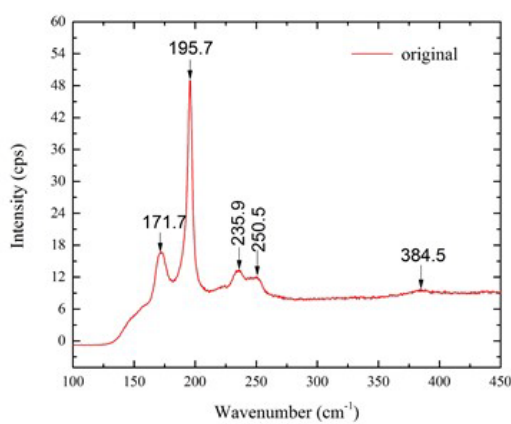
reported as another possible Raman mode of CZTSe [43, 189]. However, others have suggested this peak as well as the other three at 242.3 cm^{-1} , 289 cm^{-1} and 351 cm^{-1} are all from MoSe_2 , which is most likely correct [190, 198]. These four peaks do not appear in the other two samples measured at the same conditions. An atypical spot of M3599_12 in Fig. 4.15 was found rich in Cu_2SnSe_3 with two clear peaks at 236 cm^{-1} and 251 cm^{-1} in the low power Raman spectrum [42]. After being illuminated by 2.5 mW for 72 second , a new peak at 185.5 cm^{-1} which may also come from Cu_2SnSe_3 Raman mode instead of the 236 cm^{-1} mode [191, 199]. Meanwhile, 186 cm^{-1} was also frequently observed as SnSe_2 modes [200-202]. Fig. 4.16 shows the power dependent results for an atypical CdS rich spot in M3602_21. The strong Se Raman mode at 238 cm^{-1} was not found from this spot. Except for the intensity reduction and red shift for the two major peaks, and a initially unresolved peak at around 250 cm^{-1} becomes resolved, there is no other significant change in the Raman spectrum of this spot after high power illumination. Thicker CdS layer offered protection to the absorber from decomposing with high laser power illumination.



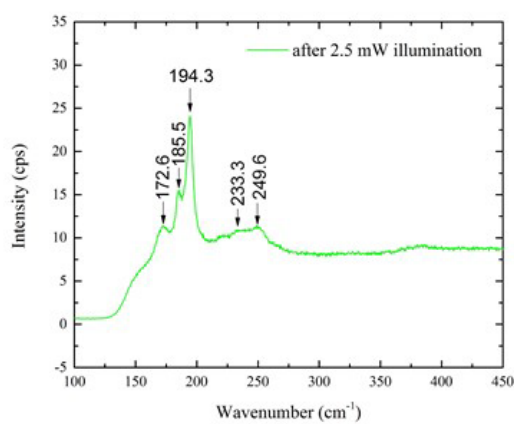


(c)

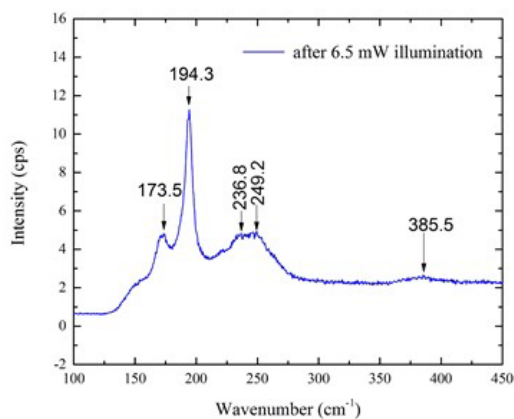
Figure 4.14: Raman spectra of another random spot measured from CZTSe_97 surface before and after high laser power illumination.



(a)



(b)



(c)

Figure 4.15: Raman spectra of another random spot measured from M3599_12 surface before and after high laser power illumination.

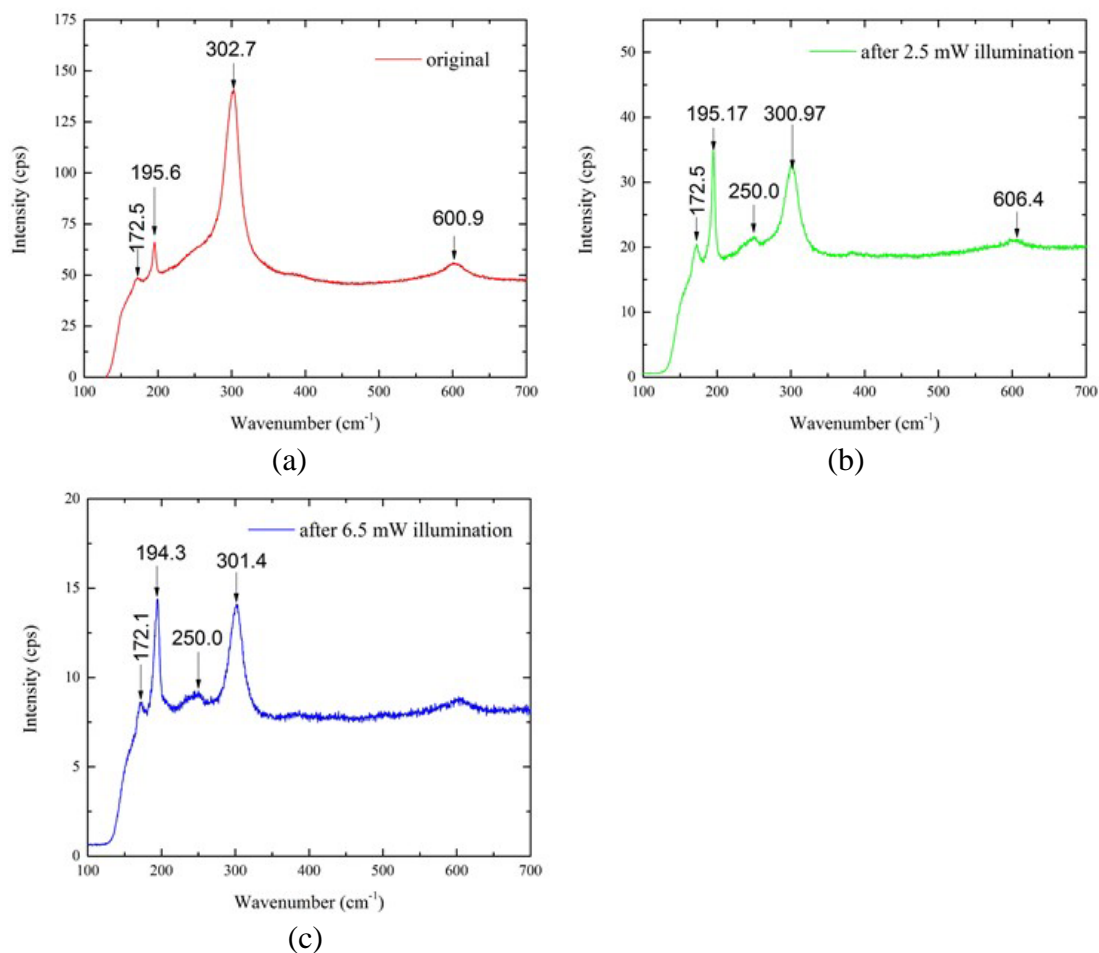


Figure 4.16: Raman spectra of CdS rich spot measured from M3602_21 surface before and after high laser power illumination.

4.3. Raman Studies of CZTSe Sample From Cleaved Edge

Raman spectra were measured with laser beam focused to different depths of the sample: Mo layer, Mo-CZTSe boundary, body of film, film-air boundary and air (when the beam was just moved off the edge of the front surface). Because of the limitation of the laser spot size, these measurements can only reveal the qualitative change. In Fig. 4.17, measured at the lower power condition (0.147 mW) from the cleaved edge, one can clearly

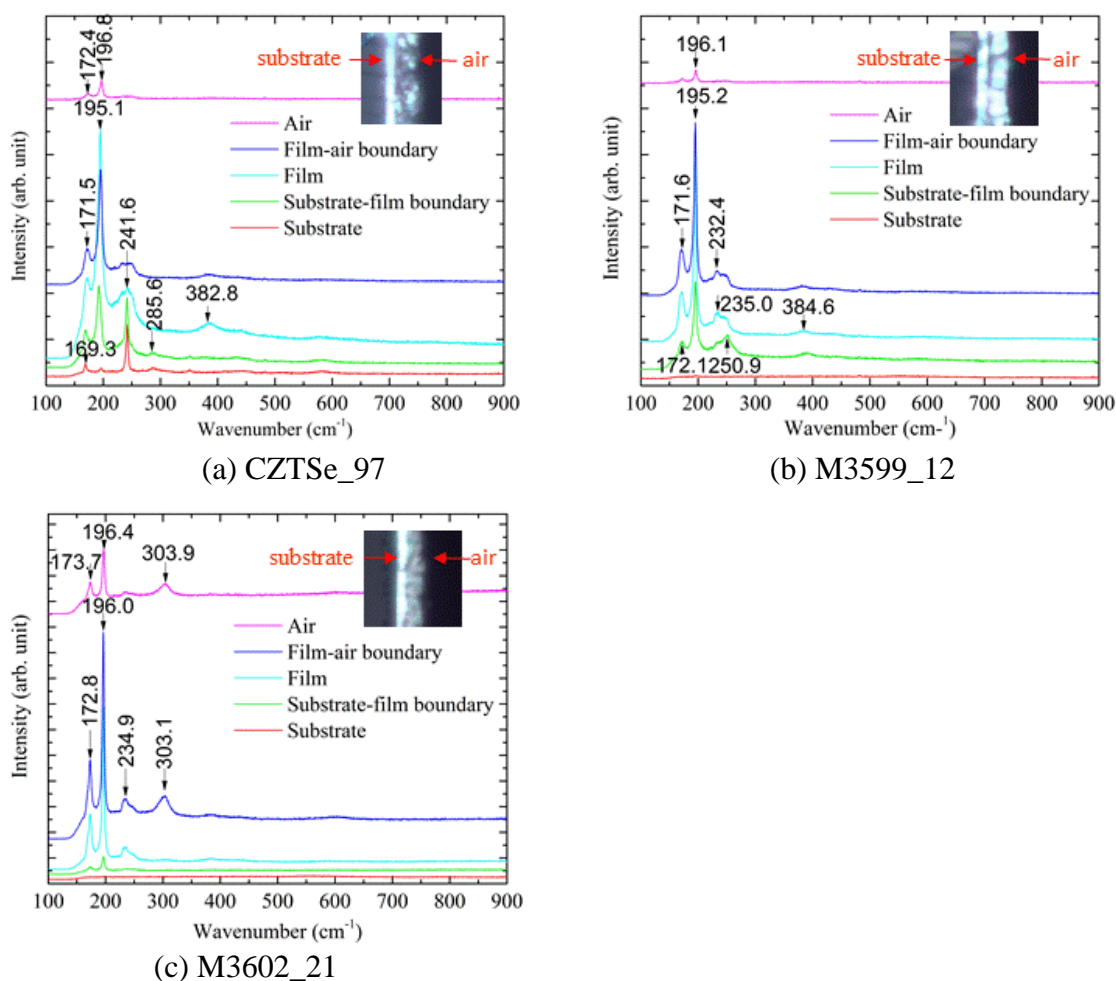


Figure 4. 17: Raman spectra of three CZTSe samples measured from the cleaved edge.

see the variation of the spectral features with the film depth. The spectra reveal the dominant components from substrate (Mo) to film. In Fig. 4.17 (a), only very weak peaks at 169, 196, 241, 286, and 351 cm^{-1} were detected on substrate. Observed close to the molybdenum layer, the $\sim 168 \text{ cm}^{-1}$ and $\sim 242 \text{ cm}^{-1}$ can be further confirmed from MoSe_2 rather than CZTSe absorber. MoSe_2 is dominant component at substrate-film boundary with Raman modes at 169, 242, 286 and 351 cm^{-1} in CZTSe_97. The mode $\sim 196 \text{ cm}^{-1}$ appears in both Mo and CZTSe layers, although substantially weaker in the Mo region. When moving toward the front surface, the MoSe_2 related peaks gradually diminish,

although remains throughout the film thickness, whereas the CZTSe peaks at 196 cm^{-1} and 172 cm^{-1} grow. Compared with results measured from the front surface, we conclude that MoSe_2 concentrates at the substrate and film boundary and exists throughout the film thickness in this sputtered sample. In contrast, in Fig. 4.17 (b) and (c), no Raman signals from MoSe_2 were observed near the substrate of M3599_12 or M3602_21. Only CZTSe Raman modes at $172, 196, 232\text{ cm}^{-1}$ as well as secondary phases such as ternary compound Cu_xSnSe_y or a-Se at 250.9 cm^{-1} and 235.0 cm^{-1} [42] are observed from M3599_12 and M3602_21.

These measured cleaved edge spots were then illuminated by higher laser power and Raman spectra from these spots were collected again at 0.147 mW , as shown in Figs. 4.18 and 4.19. After 100 seconds 1.47 mW laser illumination, CZTSe peaks in all three samples shifted to lower wavenumbers, for example, from 195.1 cm^{-1} to 193.8 cm^{-1} in the film spectra of CZTSe_97. A very weak peak at 262.3 cm^{-1} was observed when laser moves beyond the CZTSe film. As proved in the surface Raman study, high laser illumination could lead to the material decomposition and formation of Cu_xSe_y . It is possible that this weak Cu_xSe_y Raman mode came from the surface region after the center or close to substrate region was illuminated. Same Cu_xSe_y mode was also observed from M3602_21 but at the boundary of substrate and CZTSe film with much higher intensity. No new peak appeared from M3599_12 cleaved edge Raman spectra.

Increasing the illumination laser power to 4.5 mW , Cu_xSe_y Raman mode at 261.5 cm^{-1} could also be observed from M3599_12 cleaved edge spectra. Besides, a peak at 263.1 cm^{-1} which is close to Cu_xSe_y Raman mode showed up in the Raman spectrum from substrate of CZTSe_97. Additionally, many new peaks were detected at its substrate and

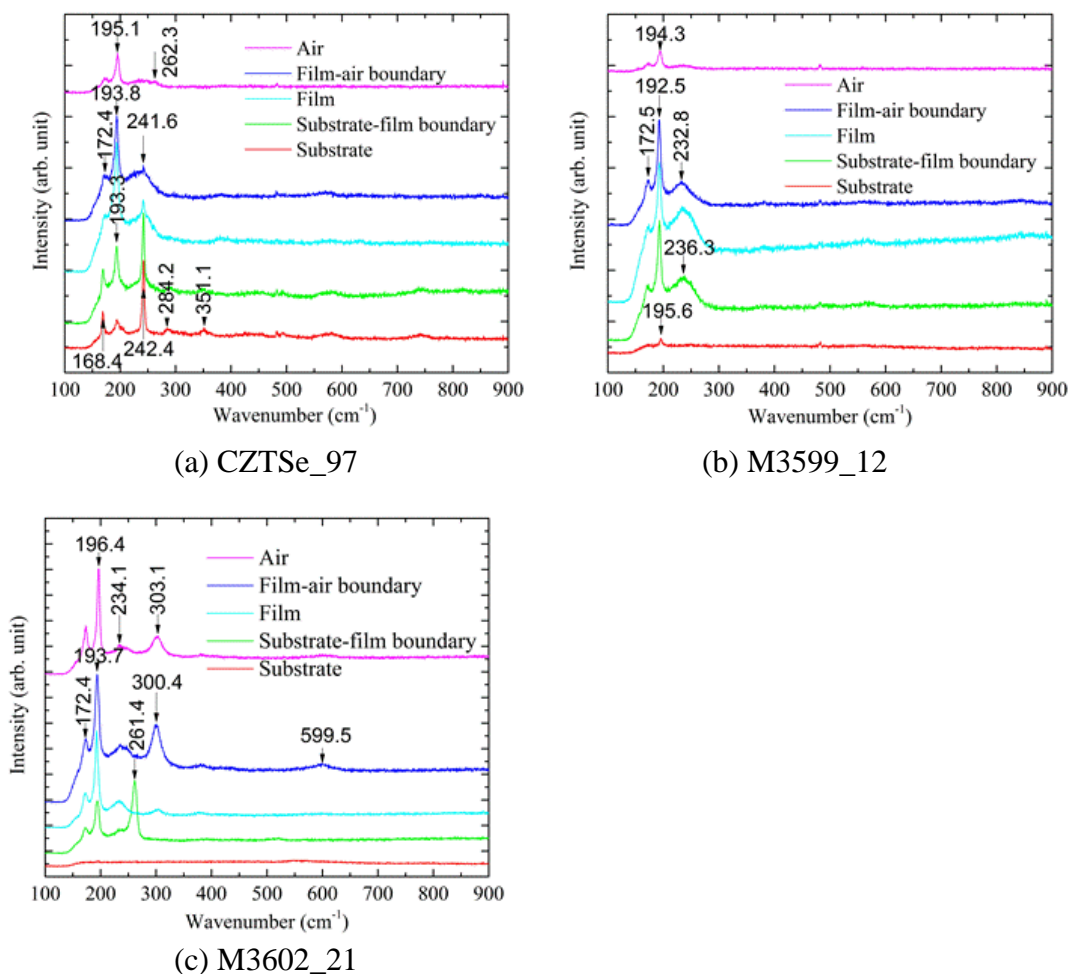


Figure 4. 18: Raman spectra of three CZTSe samples measured from the cleaved edge after being illuminated by 1.47 mW.

CZTSe film boundary, such as SnSe peak at 185.6 cm^{-1} [200-202], ZnSe peak at 202.6 cm^{-1} [203-206], and some other peaks at 729.3 cm^{-1} and 819.0 cm^{-1} which were very close the molybdenum oxide Raman modes [207]. As predicted in Ref. [208], at the CZTSe and Mo interface, it is favorable to generate secondary phases with reaction: $2\text{Cu}_2\text{ZnSnSe}_4 + \text{Mo} \rightarrow 2\text{Cu}_2\text{Se} + 2 \text{ZnSe} + 2 \text{SnSe} + \text{MoSe}_2$. Here, the result of cleaved edge Raman after high power laser illumination from CZTSe_97 confirms this process with the co-existence of ZnSe, SnSe, MoSe₂ and Cu_xSe_y near the substrate and film boundary. However, in Figs.

4.19 (b) and (c), only secondary phases Cu_2SnSe_3 / a-Se and Cu_xSe_y but no ZnSe or MoSe_2 was found in either M3599_12 or M3602_21. The ~ 235 and 262 cm^{-1} peak was found not only at the substrate and film boundary but throughout the film thickness after M3599_12 and M3602_21 being illuminated by 4.5 mW for 36 seconds. In other words, the above reaction was not preferable in M3599_12 or M3602_21. These observations again indicate the microscopic structure of the polycrystalline CZTSe film could vary substantially with deposition method.

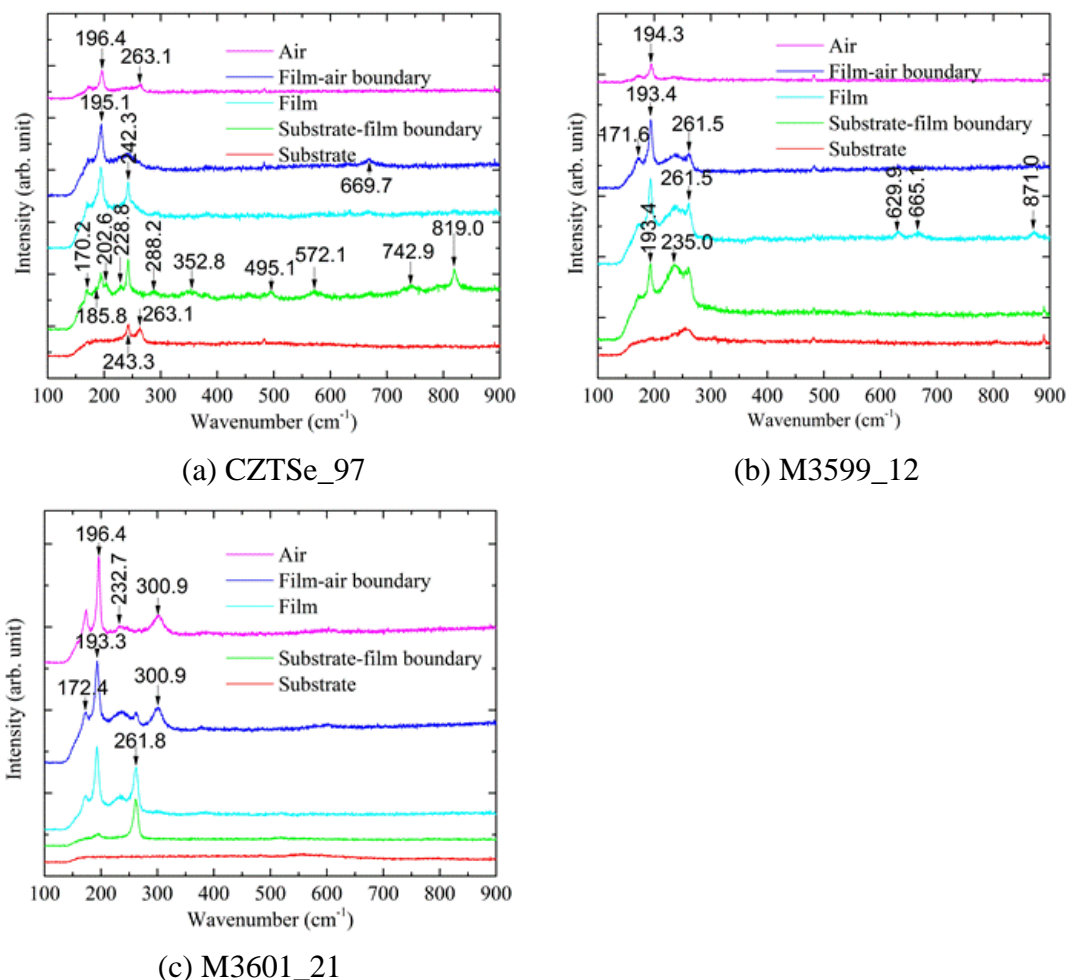


Figure 4.19: Raman spectra of three CZTSe samples measured from the cleaved edge after being illuminated by 4.5 mW.

Raman mapping at cleaved edge were also performed to locate the secondary phases across the film and phase change after higher power illumination. One horizontal line from substrate to air of CZTSe_97 cleaved edge was illuminated by 1.47 mW for 100 seconds at Mo layer substrate, Mo-CZTSe boundary, body of film, film-air boundary and air spots, marked by a circle on Fig. 4.20 (a). Raman mapping was obtained from a cleaved edge square including this illuminated line with 0.147 mW. Four clear peaks were observed: two CZTSe Raman modes at $\sim 172 \text{ cm}^{-1}$ and $\sim 196 \text{ cm}^{-1}$, MoSe₂ mode at $\sim 242 \text{ cm}^{-1}$ and Cu_xSe_y mode at $\sim 261 \text{ cm}^{-1}$. Intensity mapping results are shown in Fig. 4.20, with Fig. 4.20 (b) for 196 cm^{-1} , Fig. 4.20 (c) for 242 cm^{-1} and Fig. 4.20 (d) for 261 cm^{-1} . By comparing Fig. 4.20 (b) and (c), one can find that CZTSe are most intense from $4 \mu\text{m}$ to $5.5 \mu\text{m}$ in x-axis, whereas MoSe₂ concentrated from $2.5 \mu\text{m}$ to $3.5 \mu\text{m}$. The Raman mapping also demonstrates that the 242 cm^{-1} is Raman mode from MoSe₂ but not CZTSe. In the body of the film, the lowest CZTSe Raman intensity was found around $-1.5 \mu\text{m}$ to $-1 \mu\text{m}$ in y-axis, where the sample was illuminated with a high laser power. Cu_xSe_y (262 cm^{-1} peak) was found rich in small regions highlighted by yellow circles in Fig. 4.20 (d): one above high power illuminated region and the other under the illuminated region, which is also the periphery of the illuminated film site. However, at the illuminated site, the intensity of 262 cm^{-1} is as weak as the background, which is much smaller than what from the yellow circle regions. And in cleaved edge single spot test, no 262 cm^{-1} peak was observed in Fig. 4.18 (a) from either substrate-film boundary or the body of film. One may also notice that almost no 262 cm^{-1} signal could be found in non-illuminated film region, which confirms that the Cu_xSe_y rich regions originally did not exist in the sample.

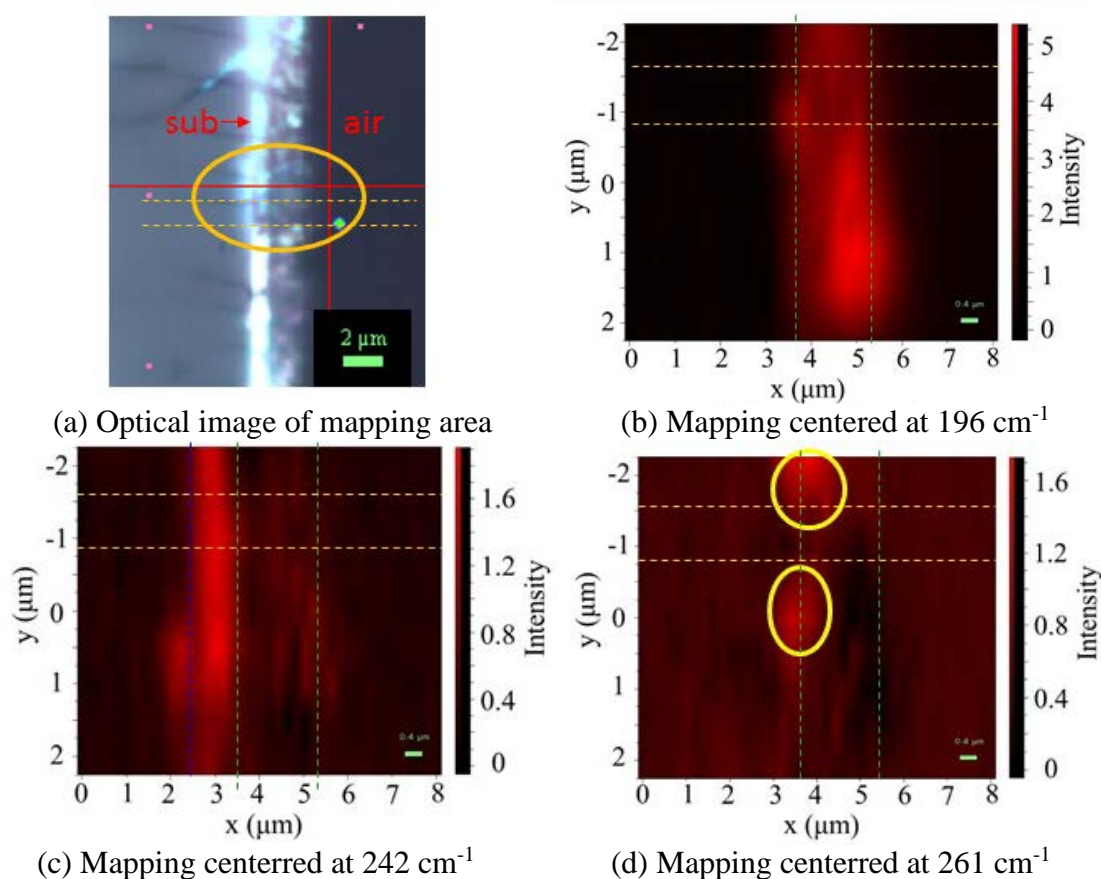
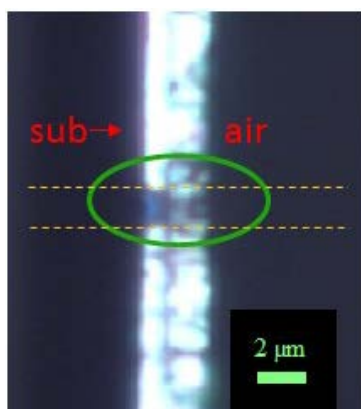


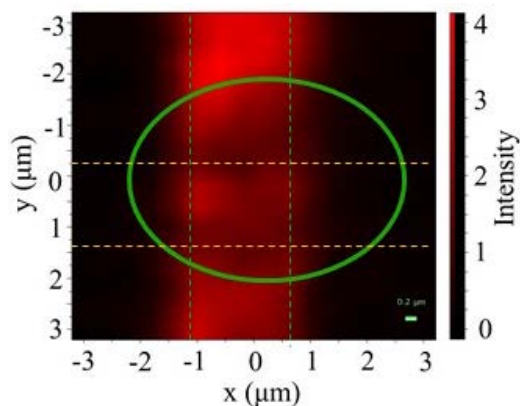
Figure 4.20: Optical image and Raman mapping of CZTSe_97 measured from cleaved edge with one x-line illuminated by $\sim 2.45\text{ mW}$.

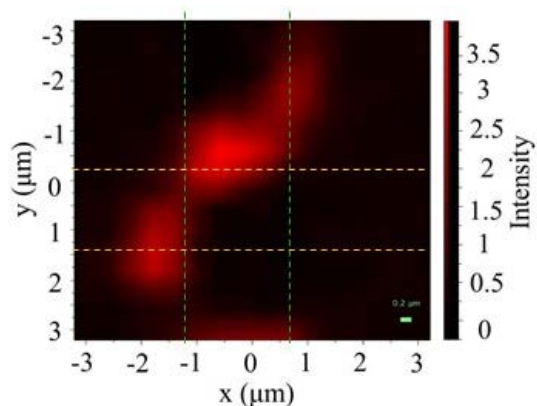
Similar Raman mapping tested were also conducted with M3599_12 and M3602_21. For M3599_12, three main peaks were observed, 172 cm^{-1} , 196 cm^{-1} and 261 cm^{-1} . In Fig. 4.21 (b), the darker region in the body of the film helped to identify easily the region been illuminated by 2.47 mW . Fig. 4.21 (c) shows the distribution of Cu_xSe_y on the cross section. The Cu_xSe_y rich region was found at substrate-film boundary as well as the body of the film, forming a half circle surrounding 2.47 mW illuminated region. Similar with surface mapping result, 261 cm^{-1} was again found strong at the periphery of the illuminated spots, but not the illuminated site. Another Raman mapping was performed at another cleaved edge region of M3599_12 with one horizontal line been illuminated by 4.5 mW . The 261

cm^{-1} peak was also observed in this mapping, but found concentrated at the substrate and film boundary as shown in Fig. 4.22. The two Raman mappings of M3599_12 cleaved edge suggested that due to the material inhomogeneity, the secondary phase Cu_xSe_y may appear only at the substrate and film boundary or surrounding the high laser power illuminated film region in the body of the film. A high laser power Raman mapping (4.5 mW excitation laser power) was performed for M3602_21. In addition to CZTSe Raman modes at 172 cm^{-1} and 196 cm^{-1} , Cu_xSe_y Raman mode at 261 cm^{-1} and CdS mode at 303 cm^{-1} were also observed in this cleaved edge mapping, as shown in Fig. 4.23. By comparing 4.23 (b) and (c), one can easily distinguish the body of the CZTSe film with Cu_xSe_y rich regions. Fig. 4.23(b) shows the CZTSe peak starts to appear at $\sim 0.5 \mu\text{m}$ and became stronger in $x > 0$ direction. On the other hand, in Fig. 4.23(c), the Cu_xSe_y Raman mode is strongest at $x \approx 0.5 \mu\text{m}$ and significantly diminished at $x \approx 1 \mu\text{m}$, which indicating that the Cu_xSe_y are mainly found near the substrate and film boundary, which is consistent to the observation of no Cu_xSe_y signal in the front surface measurement.



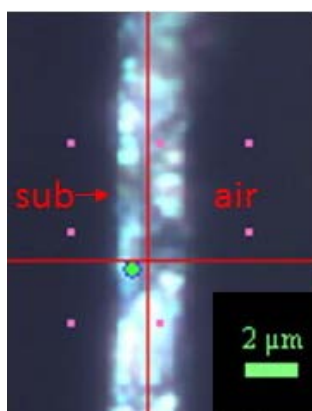
(a) Optical image of mapping area

(b) Raman mapping centered at 196 cm^{-1} .

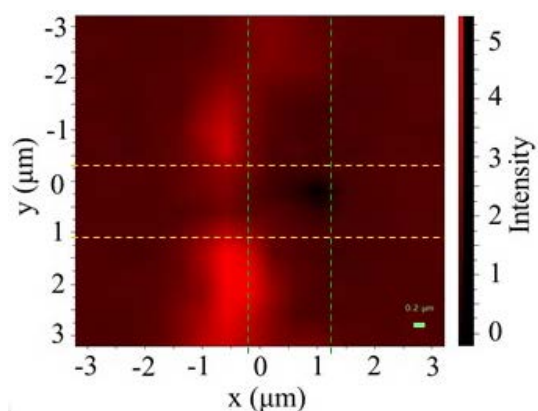


(c) Raman mapping centered at 261 cm^{-1} .

Figure 4.21: Optical image and Raman mapping of M3599_12 measured from cleaved edge with one x-line illuminated by $\sim 2.45\text{ mW}$.

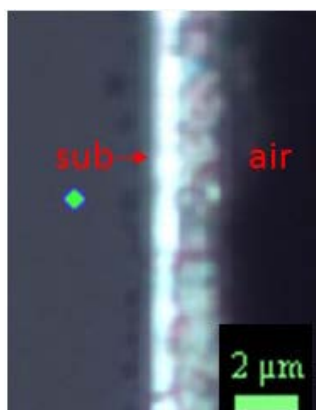


(a) Optical image of mapping area

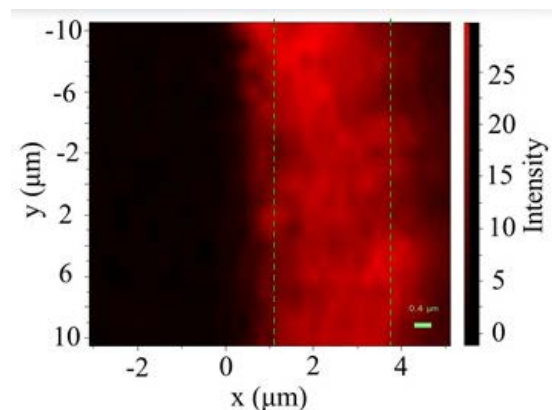


(b) Raman mapping centered at 261 cm^{-1}

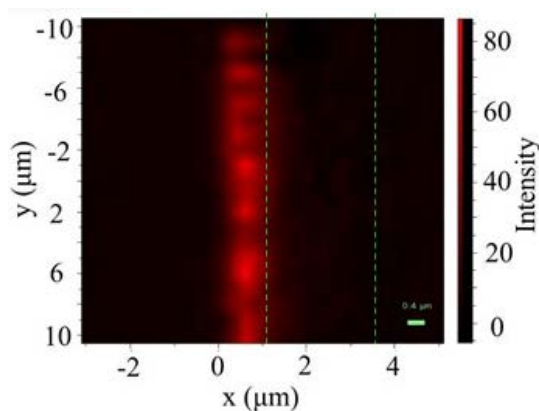
Figure 4.22: Optical image and Raman mapping centered at 261 cm^{-1} of M3599_12 measured from cleaved edge with one x-line illuminated by $\sim 4.5\text{ mW}$.



(a) Optical image of mapping area



(b) Raman mapping centered at 196 cm^{-1} .



(c) Raman mapping centered at 261 cm^{-1} .
 Figure 4.23: Raman mapping of M3602_21 measured from cleaved edge with 4.5 mW.

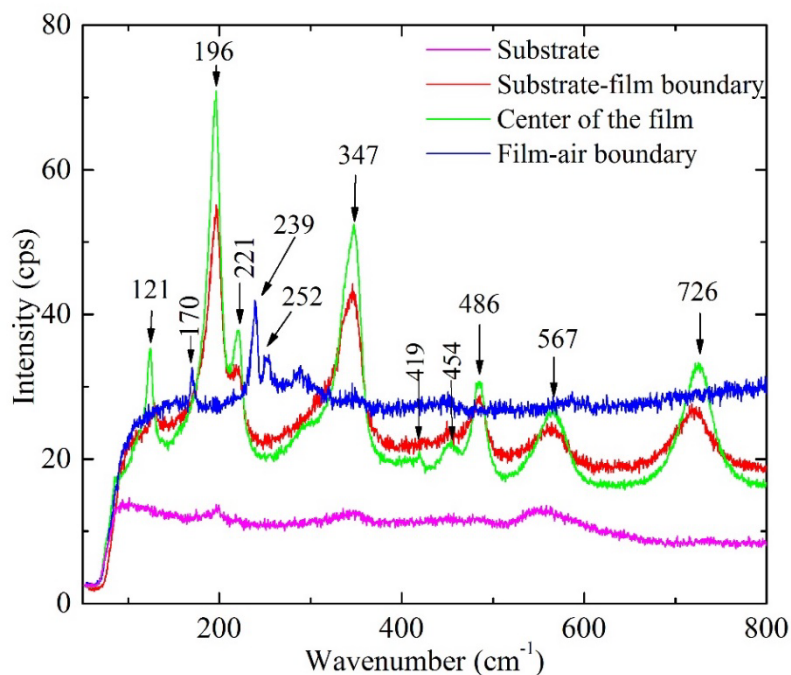


Figure 4.24: Raman spectra from multiple cleaved edge spots of M3602_21 measured with 6.5 mW.

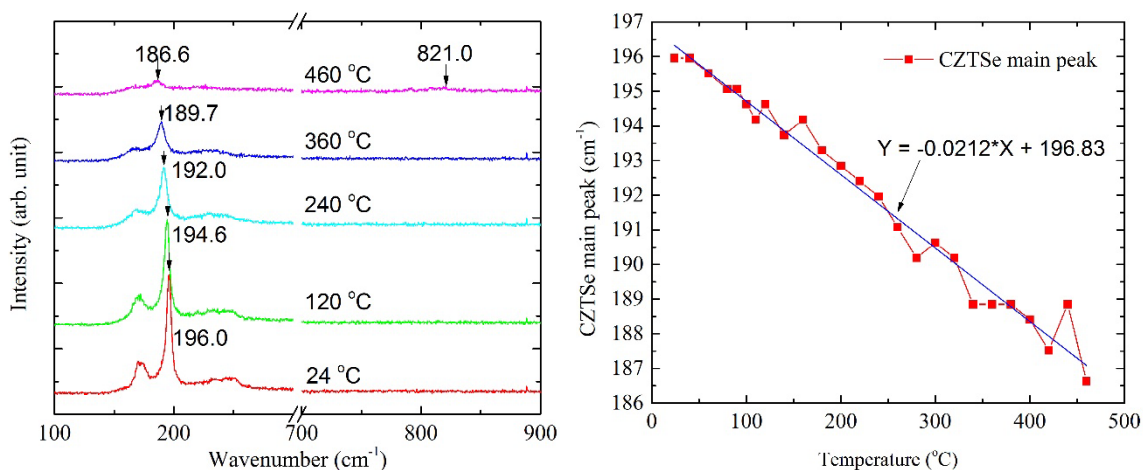
Raman spectroscopy was also obtained from multiple cleaved edge single spots of M3601_21 with 6.5 mW excitation power. Some spectra with unordinary peaks from different depth of the film were plotted in Fig. 4.24. In addition to the 196 cm^{-1} and 170

cm^{-1} peaks close to those observed CZTSe features, ZnSe mode at 121 cm^{-1} and 252 cm^{-1} [169], another CZTSe mode at 221 cm^{-1} , Se at 239 cm^{-1} , 486 cm^{-1} and 726 cm^{-1} , MoO at 347 cm^{-1} and 567 cm^{-1} were found from those spots. There are also peaks at 347 cm^{-1} and 454 cm^{-1} whose origins are yet to be determined. Multiple emerging new peaks indicate complicated phase changes within the cleaved edge films when illuminated by high laser power.

4.4. High Temperature Studies of CZTSe Samples

Raman spectra of a random spot from each sample surface were collected with a step of $20 \text{ }^\circ\text{C}$ starting from room temperature using 0.147 mW laser power with a $50\times$ long working distance lens. Fig. 4. 25 (a) shows Raman spectra of CZTSe_97 at different temperatures. The main CZTSe peak at 196 cm^{-1} started shifting when temperature raised to above $40 \text{ }^\circ\text{C}$, and gradually shifted to lower wavenumbers at a rate about $0.0212 \text{ cm}^{-1}/^\circ\text{C} \pm 0.0007$, which is obtained from the linear fit in Fig. 4. 25 (b). As indicated in Fig. 4.3, at this power level, a small heating is expected for this sample. The residual laser heating could explain why no shift was observed when the whole sample temperature was below $40 \text{ }^\circ\text{C}$, shown in Fig. 4. 25(b). One could estimate the laser induced local heating found in Fig. 4. 3 to be around $20 \text{ }^\circ\text{C}$. One may also estimate that main CZTSe Raman mode at $0 \text{ }^\circ\text{C}$ should be about 196.8 cm^{-1} according to the linear fit. When temperature was raised up to $460 \text{ }^\circ\text{C}$, the CZTSe feature almost disappeared, but a new weak peak at 821 cm^{-1} was observed, which is close to 819 cm^{-1} peak (molly oxide Raman mode) appeared at “substrate-film boundary” region of CZTSe_97 in its cleaved edge test after 4.5 mW illumination. By maintaining its intensity and position, another CZTSe Raman mode at 172 cm^{-1} was not as sensitive as the 196 cm^{-1} mode when temperature was lower than $200 \text{ }^\circ\text{C}$.

At higher temperatures, it experienced red shift about 3 ~ 4 wavenumbers and finally became a weak shoulder in the spectrum at 400 °C. The mesa-like band from 220 cm^{-1} to 250 cm^{-1} became narrower and forming a broad peak centered around 230 cm^{-1} with increasing temperature. Another random spot from the same piece was also tested at 460 °C, which turned out very different from the results of the previously tested spot, as shown in Fig. 4.26. In addition to the 185 cm^{-1} and 220 ~ 250 cm^{-1} band, there were extra weak peaks at ~ 288 cm^{-1} , ~ 661 cm^{-1} , ~ 817 cm^{-1} and so on. Temperature was further increased to 480 °C and Raman spectra from more random spots of this piece were collected. We found that there are mainly two types of Raman spectra that could be observed on the sample surface, as shown in Fig. 4.27. By comparing the two Raman spectra in Fig. 4.27, one can find the anti-correlation between 184 cm^{-1} and 821 cm^{-1} peak. This is reasonable since strong 821 cm^{-1} Raman line indicated the oxidization of Mo layer. In other words, layers above molly at these regions were totally gone.



(a) Raman spectra at different temperature (b) CZTSe main peak shift with temperature
 Figure 4.25: Raman spectra of CZTSe_97 measured from front surface at different temperature and CZTSe main peak shift with temperature.

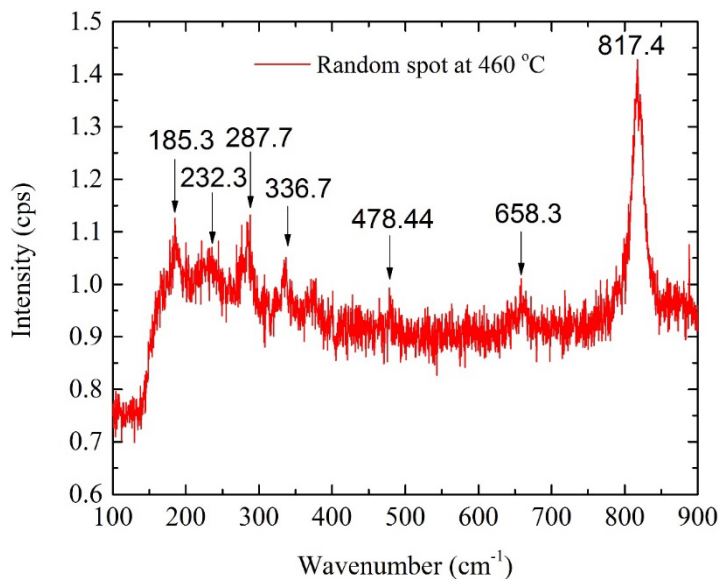


Figure 4.26: Raman spectrum of another random surface spot from CZTSe₉₇ measured at 460 °C.

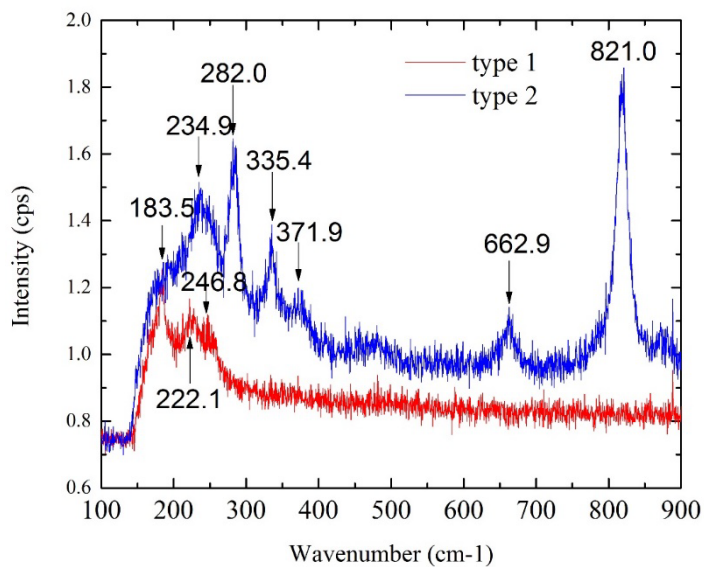


Figure 4.27: Two types of Raman spectrum measured from CZTSe₉₇ surface at 480 °C.

The sample was then completely cooled to room temperature and examined by 100x lens. There are mainly three types of regions on the sample surface: one appears very bright,

one appear dark and the last one looks greyish which could be a transition state between the previous two. Fig. 4.28 illustrates the optical images of such regions on CZTSe_97 surface and Fig. 4.29 are Raman spectra from these spots. The grey spot shows very strong Raman lines at 253 cm^{-1} and 491 cm^{-1} which match the LO and 2LO Raman modes of ZnSe [170]. From the black spot, in addition to ZnSe, Cu_2SnSe_3 at 179.2 cm^{-1} [42] and two other

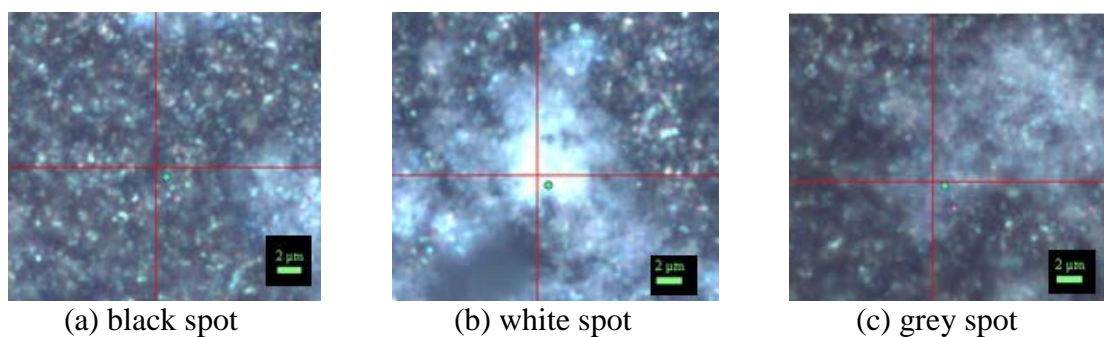


Figure 4.28: Three different types of spots on CZTSe_97 surface when back to room temperature.

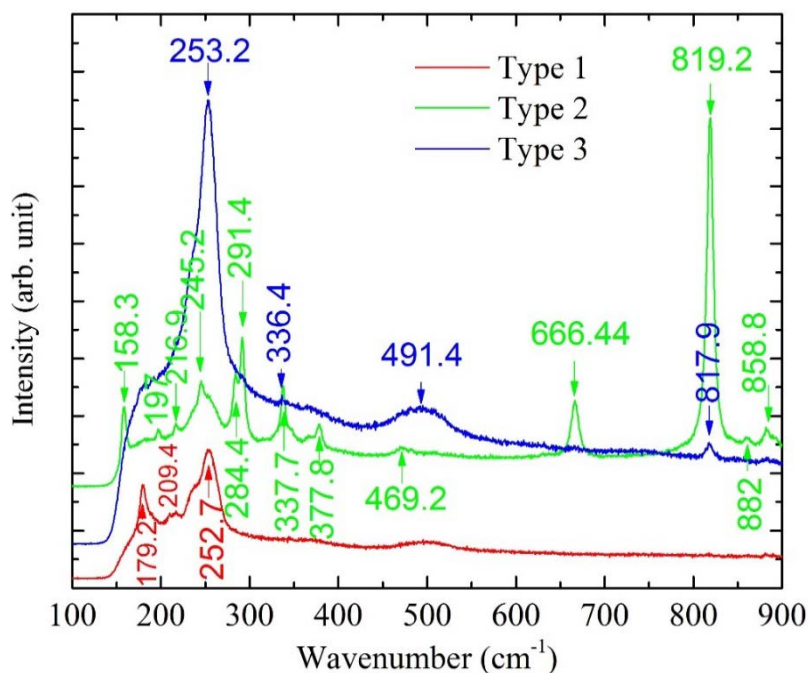
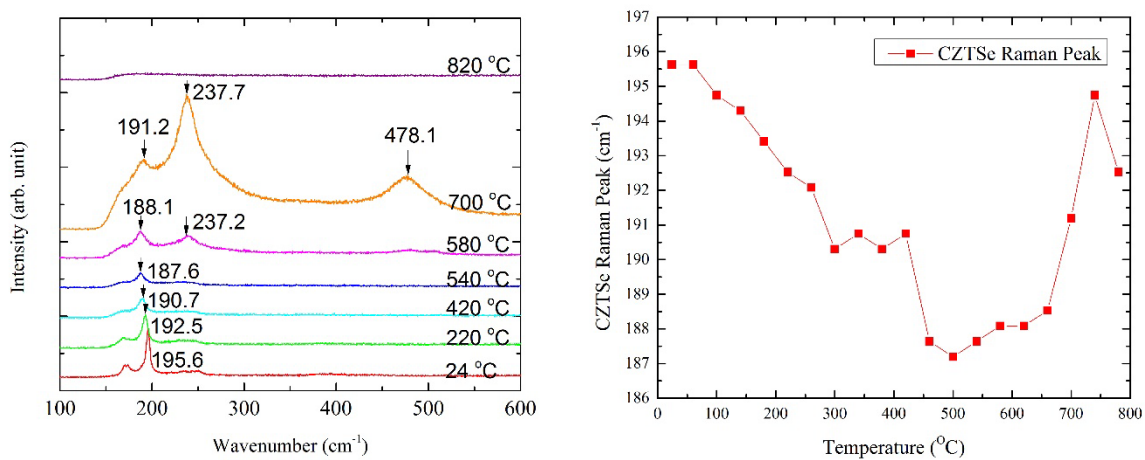


Figure 4.29: Raman spectra of three types of spots from CZTSe_97 surface after high temperature test.

peaks at 209.0 cm^{-1} and 216.9 cm^{-1} were observed. ZnSe and CuSe were both reported generating a Raman line near 209 cm^{-1} [169, 209, 210]. Here, with the coexistence of a strong ZnSe Raman line at 253 cm^{-1} , we assign this 209 cm^{-1} as ZnSe TO Raman mode. In the white spot spectrum, only very weak CZTSe peaks at 197 cm^{-1} was found. The multiple Raman peaks from 245.2 cm^{-1} to 819.2 cm^{-1} observed from the bright white spot are all very close to reported orthorhombic MoO_3 Raman bands at 247, 284, 292, 339, 367, 380, 469, 667 and 822 cm^{-1} [207]. There are also Raman peaks at 158.3 cm^{-1} , 858.8 cm^{-1} and 882 cm^{-1} from the white spot whose origins are unclear. By examining the CZTS_97 piece after high temperature, we can conclude that almost all CZTSe absorber has decomposed after being heated to $480\text{ }^\circ\text{C}$. In most cases, reaction $\text{Cu}_2\text{ZnSnSe}_4 \rightarrow \text{Cu}_2\text{SnSe}_3 + \text{ZnSe}$ took place and the surface turned darker than its original color. There are also regions leaving only ZnSe as the greyish areas. The bright reflectance of the white spot mainly comes from the Mo substrate which has been oxidized to MoO_3 .

Another piece of from CZTSe_97 was also examine and was heated up to $860\text{ }^\circ\text{C}$ by increasing the temperature at a step of $40\text{ }^\circ\text{C}$. The spectra are shown in Fig. 4.30 for selected temperature. When temperature was lower than $540\text{ }^\circ\text{C}$, the main changes in the CZTSe Raman mode such as intensity drop and linewidth broadening were similar with the results of the first piece shown in Fig. 4.25. As temperature was further increased, the band from 220 cm^{-1} to 250 cm^{-1} starts to become narrower and sharper, finally forms a sharp and strong peak centered at $\sim 237\text{ cm}^{-1}$ at $580\text{ }^\circ\text{C}$, together with the appearance of its second order mode at 478 cm^{-1} . These two peaks reach its maximum intensity at around $700\text{ }^\circ\text{C}$ and gradually diminish at higher temperature. As described in the M3602_21 high laser power illumination test, the strong peak at $\sim 237\text{ cm}^{-1}$ and 478 cm^{-1} are t-Se modes

[185]. Interestingly, Fig. 4.30 (b) shows that the main CZTSe peak experienced the largest red shift in the temperature range of 500 ~ 600 °C. When 238 cm⁻¹ started to show, i. e., when temperature was higher than 580 °C, the ~ 186 cm⁻¹ peak shifted to higher wavenumbers with increasing temperature. We note that the Raman peak observed at temperature above > 500 °C might not be CZTSe related but likely from a secondary phase Cu₂SnSe₃ or ZnSe, since the CZTSe peak was not observed when the sample was brought back to room temperature, as shown in Fig. 4.31, with multiple new Raman peaks that did not exist before the heating. Among them, 346, 565 and 732 cm⁻¹ are from molybdenum oxide. The origin of the rest peaks are not clear. However, the CZTSe related Raman mode were totally gone.



(a) Raman spectra at different temperature (b) CZTSe main peak shift with temperature
 Figure 4.30: Second test of Raman spectra of CZTSe_97 measured from front surface at different temperature and CZTSe main peak shift with temperature.

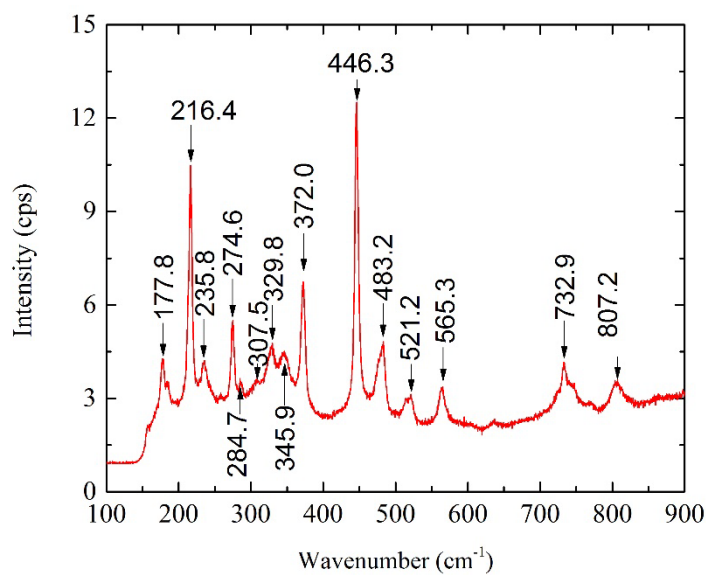
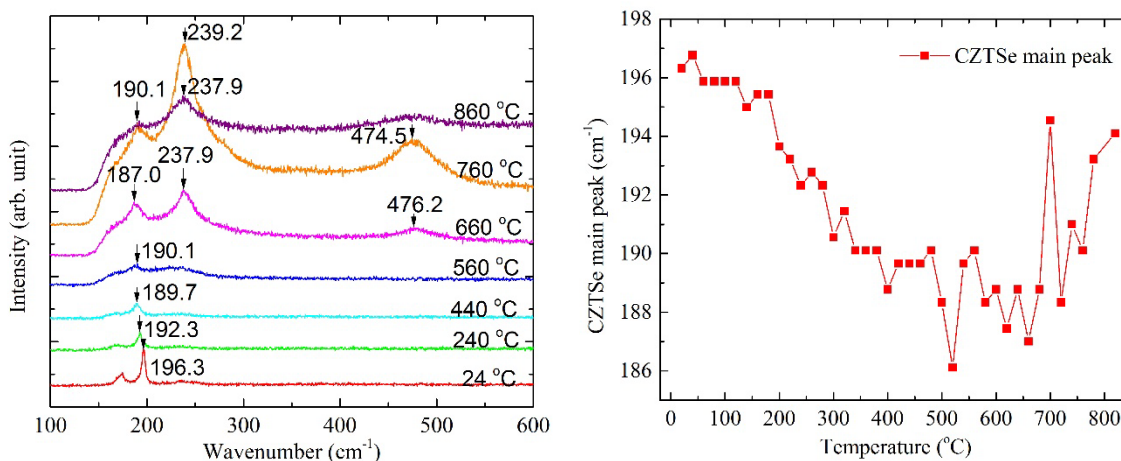


Figure 4.31: Raman spectra from CZTSe_97 surface after second high temperature test.

A small piece of M3599_12 was also studied at high temperatures with a temperature step of 20 °C. Typical Raman spectra at selected temperatures are shown in Fig. 4.32 (a), and the main CZTSe peak position shift with temperature is plotted in Fig. 4.32 (b). Similar with CZTSe_97, t-Se gradually became the dominant component when temperature was higher than 600 °C, reaching its maximum intensity around 700 °C. At the same time, the 187 cm⁻¹ peaks was shifting to higher wavenumbers. No Raman signals could be detected at 900 °C. When back to room temperature, three typical types of Raman spectra could be observed as shown in Fig.4.33. All peaks in Type 1 spectrum were from MoO₂ [207], whereas Type 3 spectrum composes of Cu₂ZnSe₃ at 180.7 cm⁻¹ [42] and ZnO at 437 cm⁻¹ [211, 212]. Type 3 spectrum contains both MoO₂, ZnO Raman modes as well as another peak from Mo₄O₁₁ at ~305 cm⁻¹ [207].



(a) Raman spectra at different temperature (b) CZTSe main peak shift with temperature
 Figure 4.32: Raman spectra of M3599_12 measured from front surface at different temperature and CZTSe main peak shift with temperature.

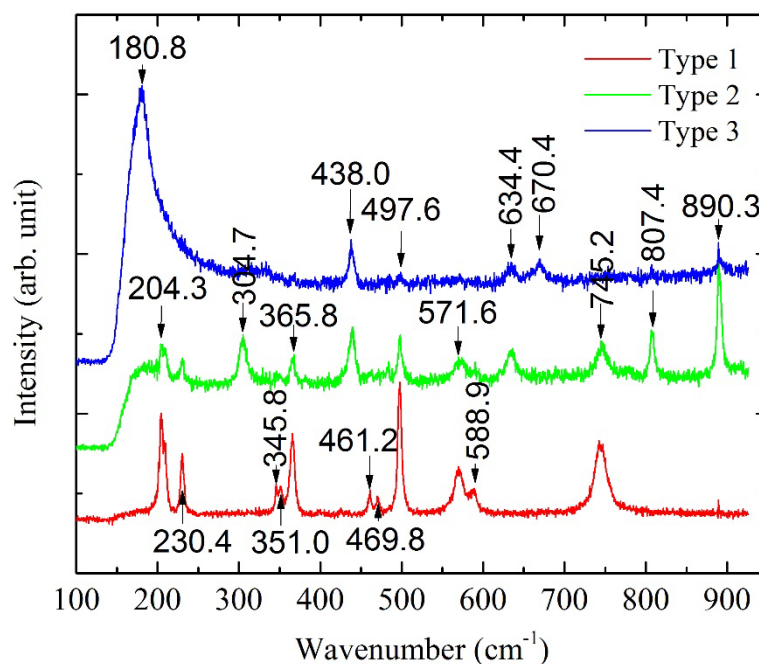
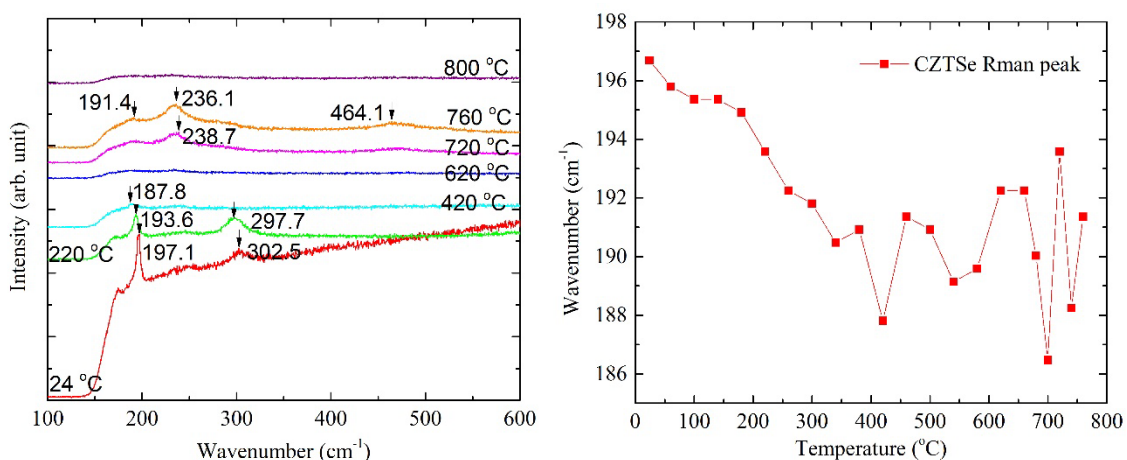


Figure 4.33: Raman spectra of three types of spots from M3599_12 surface after high temperature test.

Now, the t-Se mode could also be observed from both bare CZTSe film samples. It is safe to conclude that ~ 238 and 478 cm⁻¹ peaks in M3602_21 surface Raman after high

power illumination, Fig. 4.6 (c), are not from the extra layers of the CZTSe device, since bare film samples do not have the extra layers beyond the absorber. CZTSe device M3602_21 was also examined at high temperatures with results shown in Fig. 4.34 (a). From 380 °C to 660 °C, the t-Se modes were very weak. It became clear and dominant when temperature is higher than 700 °C and disappeared at around 800 °C. Due to the surface roughness, broad linewidth and low signal intensity at high temperatures, the positions of the main CZTSe peak were not as inaccurately determined, as shown in Fig. 4.34 (b), but in general agreement with the other measurements. Back to room temperature, two types of Raman spectra were found in Fig. 35: One shows only one strong peak of SnSe₂ at 183 cm⁻¹; and other shows Raman peaks from a mixtures of molybdenum oxide and ZnO.



(a) Raman spectra at different temperature (b) CZTSe main peak shift with temperature
 Figure 4.34: Raman spectra of M3602_21 measured from front surface at different temperature and CZTSe main peak shift with temperature.

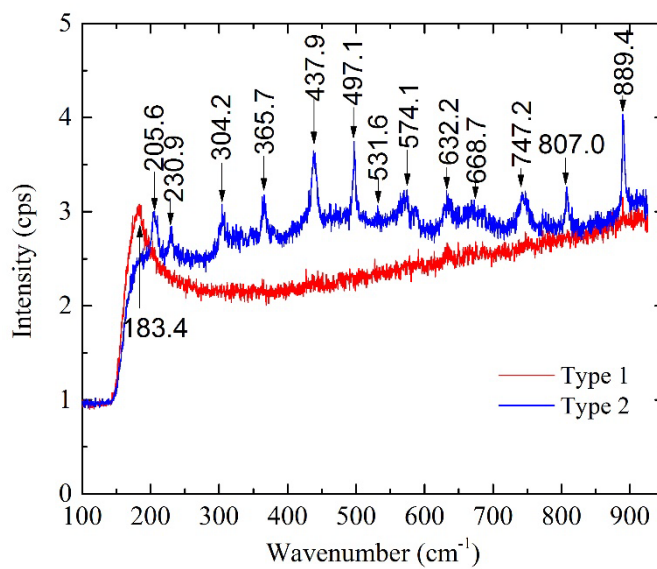


Figure 4.35: Raman spectra of two types of spots from M3602_21 surface after high temperature test.

Another M3602_21 piece was also tested with temperature increased at a step of 20 °C up to 400 °C and then cooled down to room temperature. Most parts of the absorber were found to recover at least 60% of its original intensity in the CZTSe main peak at $\sim 196 \text{ cm}^{-1}$, whereas the CdS mode at $\sim 303 \text{ cm}^{-1}$ could hardly be observed. Some dark spots with bright halo was observed. Fig. 4.36 shows four Raman spectra obtained from spots with different distance away from one such black spot, with its optical image shown as the inset of Fig. 4.36. At the center of the dark spot, resonant t-Se Raman modes were observed at 241, 482 and 717 cm^{-1} together with a shifted CZTSe peak at 192.6 cm^{-1} . The farther away from the black spot center, the smaller were the Se Raman signals. The observation indicates that after the high temperature test, the dark center on this device surface became rich in selenium. The decomposition process at high temperature within the film was not uniform. When M3599_12 was illuminated by high laser power, the mesa-band from 220 to 250 cm^{-1} also became narrower. Besides, suggested by the similarities between

M3599_12 and M3602_21 in their high temperature tests, we predict that t-selenium may also appear when M3599_12 surface was illuminated by high enough laser power. Procedures to make the absorber material a finished device may cause the absorber more sensitive to high laser power illumination.

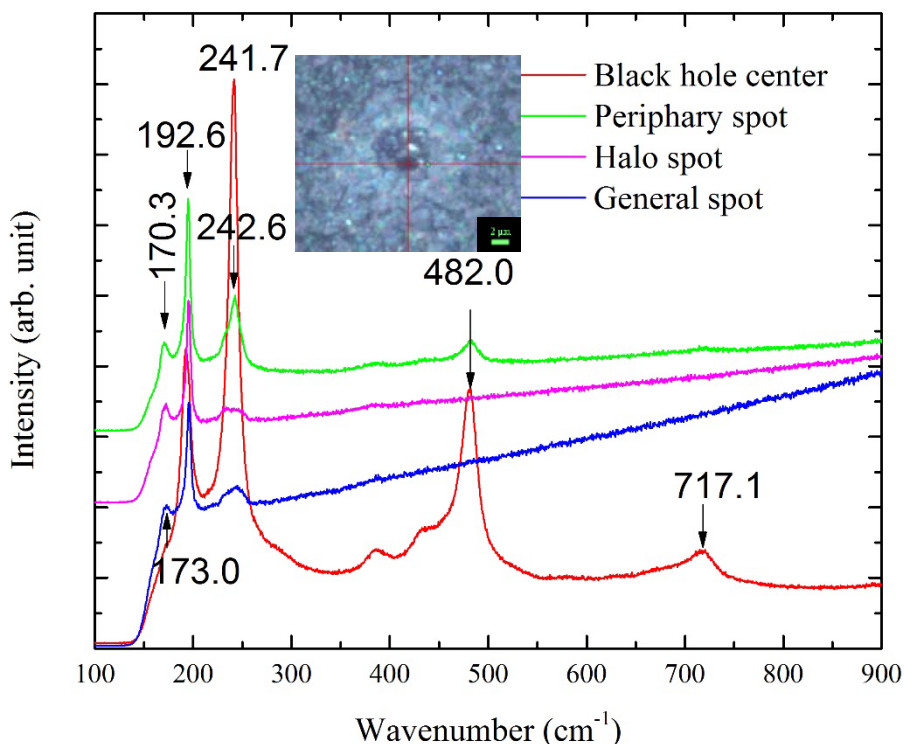


Figure 4.36: Raman spectra of different spots from M3601_21 surface after sample being heated to 400 °C.

Cu_xSe_y as a new phase was often observed after high laser power illumination from either front surface or cleaved edge. However, no Cu_xSe_y mode at 261 cm^{-1} was observed in the high temperature test from any of the three samples. In the high temperature test, the entire sample was heated up uniformly, whereas laser illumination offered highly localized non-uniform heating. Thus, lateral thermal conductivity and stress both play a role in the formation of the Cu_xSe_y peak.

With the help of the temperature induced Raman shift of the main CZTSe Raman peak from the high temperature Raman measurements, we were able to estimate that for the front surface measurement, the local temperature of the illumination site under ~ 2.47 mW illumination reached about ~ 300 °C in CZTSe_97, ~ 240 °C in M3599_12, and ~ 220 °C in M3602_21 surface. Under ~ 4.5 mW illumination, they were about 420 °C in CZTSe_97 and 340 °C in M3599_12. Since the CZTSe main peak of M3602_21 barely shift after 4.5 mW illumination, the temperature with 4.5 mW illumination on M3602_21 surface could not be determined this way.

4.5. High Laser Power Illumination Effect on LBIC Current and Cleaved Edge LBIC Mapping

To study the high laser power illumination effect on CZTSe device performance quantitatively, LBIC from a 5×5 μm square on M3602_21 device was measured with different laser power. Raman mapping was also performed before and after high power illumination to show the correlation between Raman and LBIC. Mapping data were collected with a step size of 0.25 μm . Laser powers of ~ 2 μW , 30 μW and 169 μW were used respectively to generate photo-current, as shown in Fig. 4.37 (a – c). LBIC mapping at 2 μW was re-measured at the same region to examine the effect of 169 μW illumination on the CZTSe device, as in Fig. 4.37 (d). With ~ 2 μW , average EQE of mapping area is around 85% , very close to the macroscopic EQE of a similar device 81% . At ~ 30 μW , the average EQE quickly dropped to 35% , varying from 22.6% to 35.1% . When laser power increased to ~ 169 μW , average EQE dropped a factor of seven from its original EQE at ~ 2 μW , which is consistent with the data obtained from CZTSe device M3599_23 in Chapter 3. LBIC mapping was performed instantly again at the same square after ~ 169

μW illumination to examine whether LBIC would be affected by $\sim 169 \mu\text{W}$ illumination. By comparing Fig. 4.37 (a) and (d), one can find that the lowest and highest EQE values of the two mappings are close. Average EQE of Fig. 4.37 (d) is about 77% of that in Fig. 4.37 (a), which indicates that $\sim 169 \mu\text{W}$ illumination has led to an about 23% reduction in the average photo-current of the device.

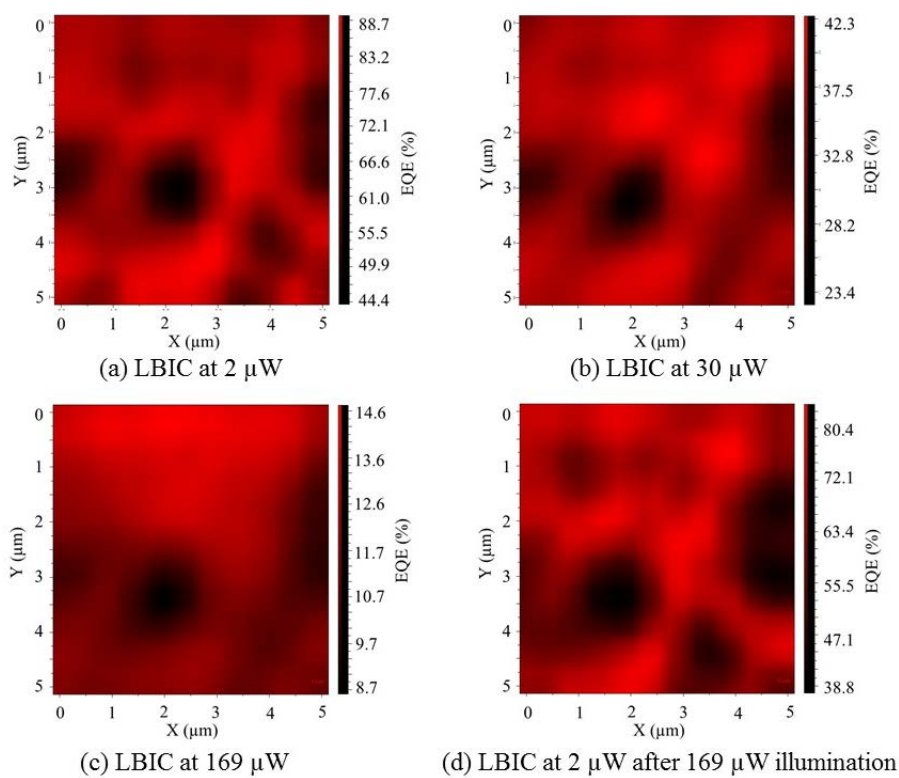


Figure 4.37: LBIC mapping at lower laser power levels.

A Raman mapping at $\sim 169 \mu\text{W}$ was also performed at the same square with a step size $0.25 \mu\text{m}$. Similar with the single spot test in section 4.2, two CZTSe Raman modes at 172 and 196 cm^{-1} , two CdS related modes at 303 and 602 cm^{-1} , and one mesa-like band from 220 to 250 cm^{-1} were observed in the mapping. Fig. 4.38 shows the mapping result centered at the main CZTSe Raman modes 196 cm^{-1} . If we compare the bright regions in the Raman mapping with the dark regions in $\sim 2 \mu\text{W}$ LBIC mapping, it seems that areas

with stronger CZTSe Raman signals generate smaller photo-current than the general area, which suggests that thicker absorber layers may not result in higher currents. Optimum absorber thickness is desired to further improve the solar cell performance.

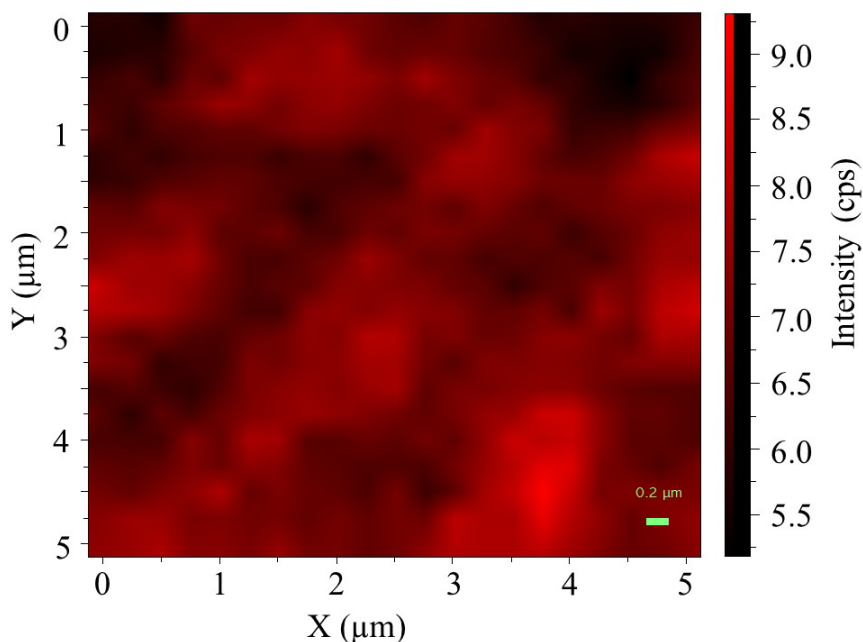
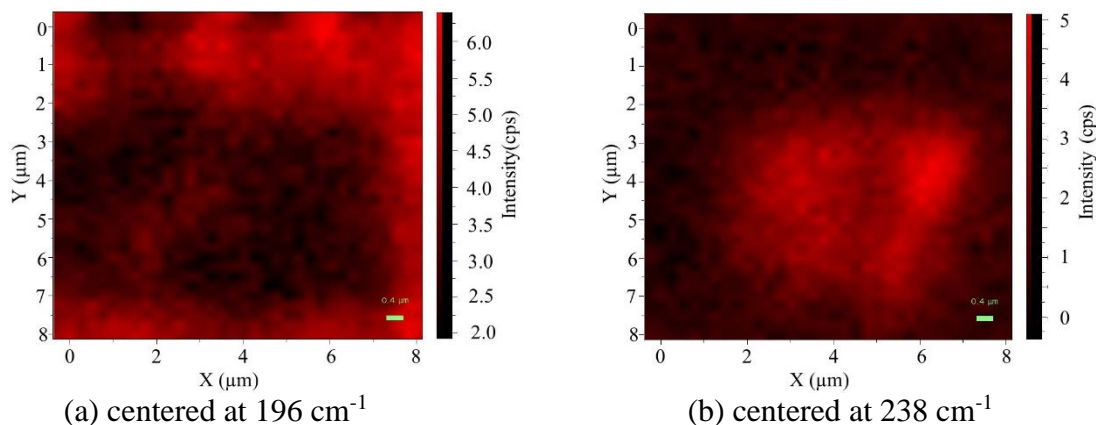
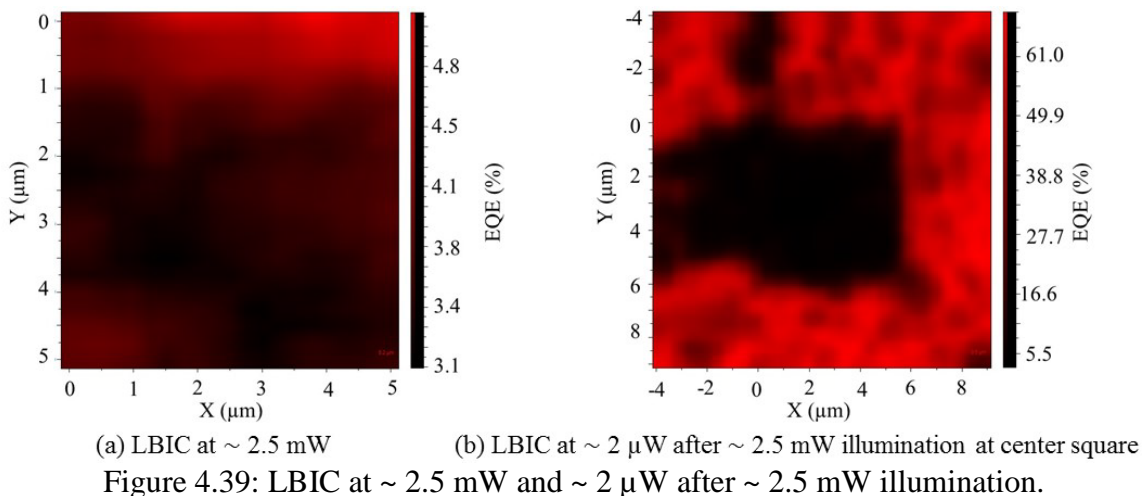


Figure 4.38: Raman mapping at $\sim 169 \mu\text{W}$ centered at 196 cm^{-1} .

Even high power $\sim 2.54 \text{ mW}$ was used to illuminate a $5 \times 5 \mu\text{m}$ square and its LBIC data were collected in Fig. 4.39 (a). Average EQE of this region further drops to 3.6%. To illustrate $\sim 2.54 \text{ mW}$ illumination effect, a $15 \times 15 \mu\text{m}$ square which contains the previous illuminated $5 \times 5 \mu\text{m}$ square was mapped in Fig. 4.39 (b). After being illuminated by $\sim 2.54 \text{ mW}$, the photo-current dropped over a factor of twenty, which led to the dark square in Fig. 4.39 (b). Raman mapping using low power $\sim 169 \mu\text{W}$ suggests the Raman intensity drops in the illuminated square, which is consistent with the previous result in Chapter 4.2. The original mesa-like band started became narrower and stronger forming a band from

216 to 247 cm^{-1} in the ~ 2.54 mW illuminated region, as shown in Fig. 4.40 (b). When laser power was further increased to 4.5 mW, the average EQE of the 5×5 μm was only



2.6%. The LBIC mapping at ~ 2 μW in Fig. 4.41 (b) shows the LBIC contrast between high laser illuminated area and the non-illuminated area. In ~ 169 μW Raman mapping, strong peaks at 238 cm^{-1} was observed, which can also be predicted by surface Raman studies in Chapter 4.2. Fig. 4.42 shows the intensity distribution of 238 cm^{-1} peak at the high laser power illuminated area. As stated before, due to the film inhomogeneity, not all

spots in the high power illuminated area could generate the strong t-Se Raman mode. In this mapping, selenium is concentrated at the left-upper corner of the higher power illuminated area.

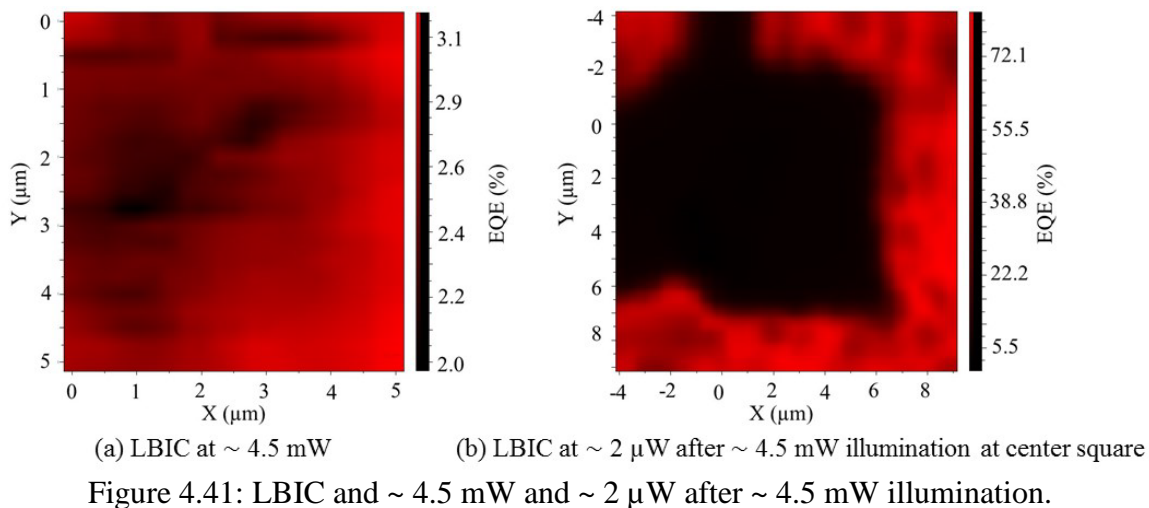


Figure 4.41: LBIC and ~ 4.5 mW and ~ 2 μ W after ~ 4.5 mW illumination.

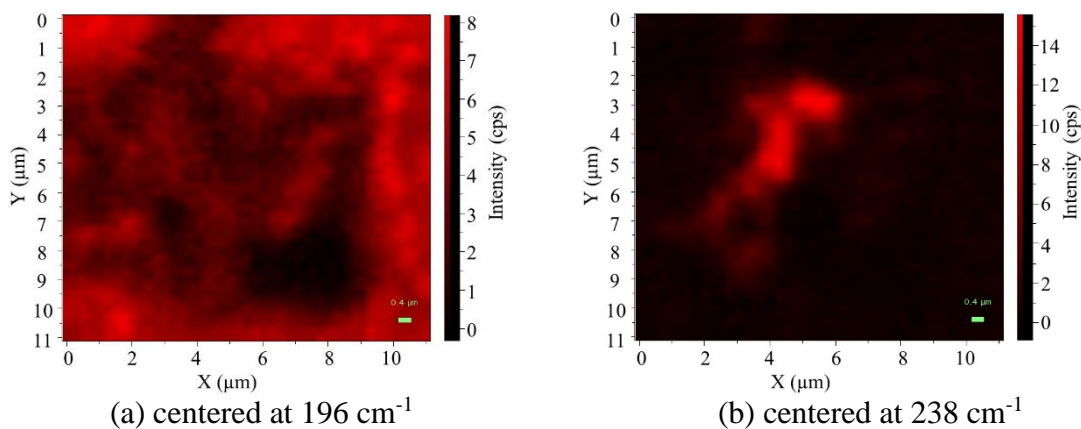


Figure 4.42: Raman mapping at ~ 169 μ W after center square being illuminated by ~ 4.5 mW.

LBIC from random single spots (one CdS rich bright spot, one CdS rich dark spot and two general spots) at different conditions were measured and compared in Fig. 4.43. All LBIC data were collected at ~ 2 μ W. Test 1 data were measured when spots were first

time illuminated by $\sim 2 \mu\text{W}$; In Test 2, same spots were measured again with $\sim 2 \mu\text{W}$ after the spots being illuminated by $\sim 30 \mu\text{W}$ for several seconds; Test 3 and 4 were similar with Test 2 by only changing the illumination laser power to $\sim 169 \mu\text{W}$ and $\sim 2.54 \text{ mW}$. After the spots being illuminated by $\sim 4.5 \text{ mW}$, current could barely be measured when excited by $\sim 2 \mu\text{W}$. One can clearly see how the LBIC signal change after higher power illumination for different types of spots. The CdS rich spots originally yield lower LBIC, which is consistent with the results in Chapter 3. After being illuminated by $\sim 30 \mu\text{W}$ and $\sim 169 \mu\text{W}$, photo-current from all spots drop about 5% \sim 12%. However, after $\sim 2.54 \mu\text{W}$ illumination, currents from general spots experienced over 90% reduction, whereas dark spot only had 77% current loss and 27% for bright spot, which makes the photo-current from bright the largest after being illuminated by $\sim 2.54 \text{ mW}$. Thicker CdS layer not only experiences less EQE droop at higher laser power, but also helps to protect the absorber from heating effect at high power illumination.

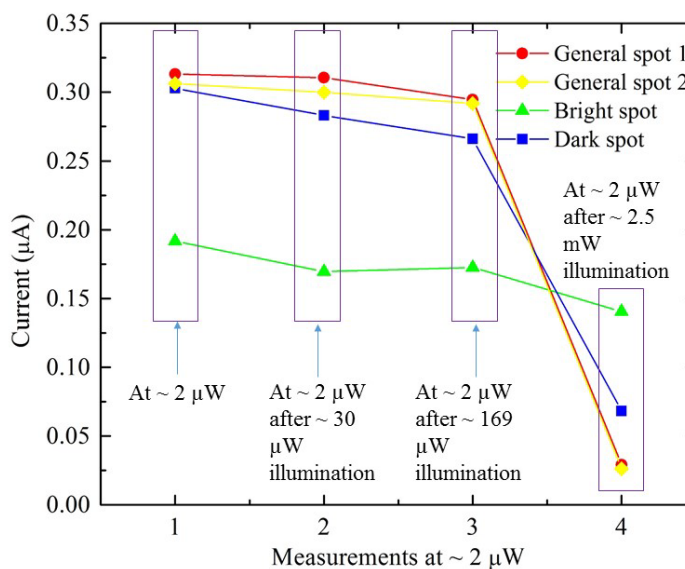
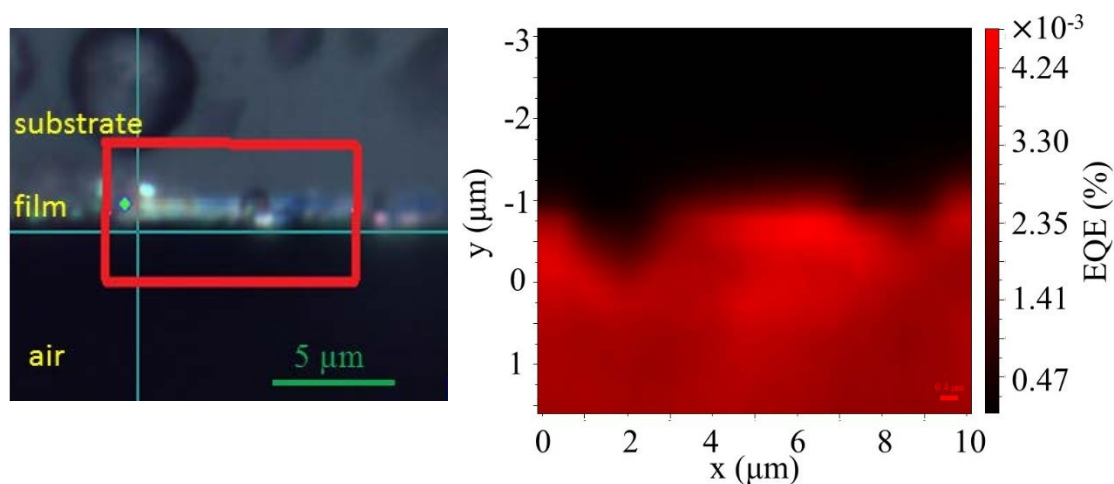


Figure 4.43: Single spot LBIC at $\sim 2 \mu\text{W}$ after different illumination conditions.

LBIC mappings were also performed from cleaved edge. In Fig. 4.44, a $10 \times 4.5 \mu\text{m}$ rectangular area from M3602_21 cleaved edge was mapped with a step size of $0.2 \mu\text{m}$. Due to the weak photo-response from cleaved edge, 2.47 mW was used to obtain stable output from the lock-in amplifier. The front side of the device was fully covered by silver paint to reduce the contribution from the front surface that was illuminated by scattered light. One can clearly see the boundary between substrate and the film body at $y \sim -1 \mu\text{m}$ and the photo-current variance along the cleaved edge in Fig. 4.44 (b), although EQE of the cleaved edge is only $1/1000$ of EQE of the front surface, as indicated in Fig. 4.39(a) and Fig. 4.44(b). This result only serves the purpose to demonstrate the feasibility of cleaved-edge LBIC mapping. Since it has been shown above that that the high illumination power such as that used for this demonstration would lead to material structural changes, the signal to noise ratio should be improved to perform the measurement at lower illumination power.



(a) optical image of mapped cleaved edge. (b) cleaved edge LBIC mapping at 2.47 mW .
Figure 4. 44: LBIC mapping of M3602_21 measured from cleaved edge.

4.6. Summary

High power and high temperature Micro-Raman studies were performed with three CZTSe samples: bare sputtered film (CZTSe_97), bare co-evaporated film (M3599_12), and CZTSe device with co-evaporated absorber (M3602_21). Secondary phases such as Cu_2SnSe_3 and SnSe were found in all three samples. Raman peaks at $\sim 250 \text{ cm}^{-1}$ also indicates possible existence of ZnSe and a-Se in the films. Most CZTSe Raman modes especially the main peak at 196 cm^{-1} experienced red shift and intensity drop after high power illumination. In general, high power illumination brought more change to CZTSe_97 than to M3599_12, not only in the CZTSe Raman peaks but also in the secondary phases, which suggested that films prepared by the sputtering method is structurally less robust than that of films fabricated by the co-evaporation method. And in CZTSe device M3602_21, a strong Raman mode at $\sim 238 \text{ cm}^{-1}$ and secondary mode at $\sim 478 \text{ cm}^{-1}$ from t-Se were introduced by high power illumination. Raman mapping near a high power illuminated spot shows a Cu_xSe_y rich ring enclosing the illuminated spot on the surface of CZTSe_97 and M3599_12. But no Cu_xSe_y was observed from M3602_21 while the illuminated spot generating strong Raman mode at $\sim 238 \text{ cm}^{-1}$ due to the photocrystallization of a-Se originally in the film and t-Se generated by CZTSe decomposition at the illuminated site.

The cleaved edge Raman spectroscopy reveals the depth profile of the film. Dominant MoSe_2 was found at the Mo substrate and film boundary of CZTSe_97, but not in M3599_12 or M3602_21, suggesting that the sputtering method tends to introduce MoSe_2 at the interface of molly and CZTSe film. Moreover, CZTSe film and Mo reacted at their interface, which generates new secondary phases SnSe , ZnSe and Cu_xSe_y , when

illuminated by high laser power in CZTSe_97. Cu_xSe_y was also detected in M3599_12 and M3602_21 after high power illumination. Due to the inhomogeneity of the film, Cu_xSe_y was found concentrated at the substrate-film boundary in some region or existed throughout the film thickness in other regions. When excited by 6.5 mW, new secondary Raman peak such as t-Se and Mo_xO_y could be observed from multiple spot from the cleaved edge of M3602_21.

In high temperature Raman measurements, in addition to red shift, intensity reduction and linewidth broadening of the CZTSe main peak, t-Se Raman mode at $\sim 238 \text{ cm}^{-1}$ together with its second order mode around $\sim 478 \text{ cm}^{-1}$ showed up in all three samples when temperature was higher than $560 \text{ }^\circ\text{C}$. It is reasonable to conclude that t-Se did not originate from the extra layers of the CZTSe device, but from photocrystallized a-Se which existed in the absorber before high laser power illumination and CZTSe decomposition during heat treatment. After heated to above $480 \text{ }^\circ\text{C}$, most CZTSe films disappeared when back to room temperature. Molybdenum oxide, ZnSe and ZnO were left on the sample surface. Due to the film inhomogeneity, scattered regions rich in t-Se were found on M3602_21 surface if only heated to $400 \text{ }^\circ\text{C}$.

Combining LBIC and Raman data obtained from some regions before and after high laser power illumination, we succeed analyzing high laser power effect on photo-current. An optimum absorber thickness is expected, as suggested by correlated Raman and LBIC mapping. Thicker CdS layer was found to offer extra protection to absorber from the damage caused by high laser power illumination.

In summary, in this chapter, we on one hand demonstrate the secondary phases existence in CZTSe films fabricated by different methods, and on the other hand, present

the different behaviors of these CZTSe films when illuminating by high laser power from both front surface and cleaved edge. This study has shown that the combination of high-laser-power and high-temperature Raman study can offer an effective approach to examine the microscopic structural variations of the complex alloys like CZTSe that might otherwise appear to be similar in their simple room temperature Raman spectra and device performance

CHAPTER 5: LBIC STUDY OF CZTSE CELLS WITH DIFFERENT DEVICE STRUCTURE AND ELEMENTAL RATIOS IN ABSORBER

5.1. Introduction

It is well-recognized that elementary ratios of Cu, Zn, Sn, S(Se) within CZTS(Se) absorber layer can have a great impact on the CZTS(Se) solar cell performance. Not only are the formation of secondary phases but also defect densities strongly depend on the elementary ratios. At present, people have not come to a conclusion the best elementary ratio in CZTS(Se) films for PV application. In general, a Cu-poor and Zn-rich composition is expected for better CZTS(Se) properties. Top-performance CZTS(Se) devices are having a Cu/(Zn+Sn) ratio from 0.77 to 0.86 and Zn/Sn ratio around 1.1 to 1.25 [26, 28, 44].

T. Tanaka et al. find that Cu-rich condition is good for better crystallinity and larger grain size, but Cu-rich films show remarkable low resistivity, which is not suitable for solar cell application [213]. Cu_xSe_y , which usually forms in Cu-rich condition, will short solar device with semimetal phases [214]. Moreover, Cu-rich will introduce more Cu_{Zn} intrinsic defects which are also an unfavorable situation in CZTS(Se) solar cells [54], because it is expected to introduce deep acceptors. Theoretically, excess Sn has been predicted to increase Sn_{Zn} antisite defects which has deep level inside the band gap and will act as recombination centers [63]. In Cu-rich and Sn-rich condition, aggregation of Cu_{Zn} and Sn_{Zn} antisite defects leads to high population of $\text{Cu}_{\text{Zn}} + \text{Sn}_{\text{Zn}}$ and $2\text{Cu}_{\text{Zn}} + \text{Sn}_{\text{Zn}}$ defect clusters which are believed to be harmful for PV application [215]. In Ref. [216], optoelectronic properties were experimentally studied from CZTSe films with different Zn/Sn ratio. It was

found Sn rich bulk exhibited n-type conductivity with a very high electron density $> 10^{19}$ cm^{-3} . In Zn rich p-type bulks, carrier concentration would increase with Zn content when $1 < \text{Zn/Sn} < 1.35$. The electrical conductivity would consistently increase with Zn/Sn ratios in Zn-rich bulks.

However, more Zn in the system would at the same time increase the possibility of ZnS or ZnSe formation in the film, which is a possible unfavorable secondary phase for the solar cell performance. Degradation of the electrical performance of CZTSe cell is reported to correlate to ZnS [61]. However, a 8.4% efficiency CZTS cell can still be achieved with large amount of ZnS in Ref. [91]. W. Hsu et al. have compared a set of CZTSe cells which were co-evaporated in same or similar conditions but differed in Zn/Sn ratio. They suggested that ZnSe in different depth within the film may have different impact on the cell performance. ZnSe particles precipitating on the back of the absorber will not affect the device performance, whereas large ZnSe grains on the front of the absorber can lead to a much lower performance. More detailed effects of Zn content on device performance is still unclear.

5.2. I-V Curves of Different CZTSe Solar Cells

Multiple CZTSe devices, M3602_22 with 8% efficiency, M3599_23 (8%), M3690_13 (4%) and M3652_13 (3%) are compared in this study. The absorbers are all deposited by co-evaporation method. Device fabrication details can be found in Ref. [44]. The standard cell structure is similar to Fig. 1.5 in Chapter 1, except for in M3602_22 an extra 150 Å e-beam evaporated NaF precursor between molybdenum back contact and CZTSe absorber. Five studied devices differ from each other in either elementary ratios in

the absorber, or some cell structural variation from the standard stack, or absorber anneal process. Table 2 summarizes the differences between them.

Table 2. Structural and elemental difference between different CZTSe solar cells.

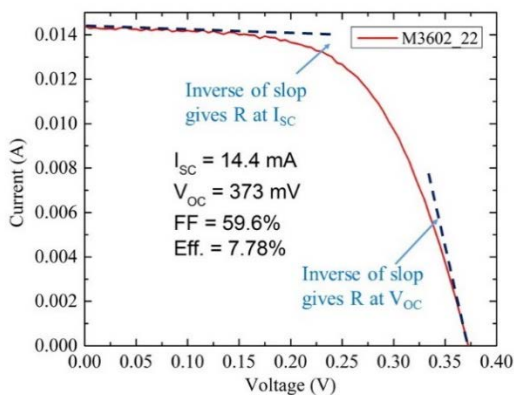
	Efficiency (%)	Absorber thickness (μm)	Zn/Sn	Cu/(Zn+Sn)	Structure
M3602_22	8	1.3	1.28	0.87	Standard structure
M3599_23	8	1.49	1.32	0.82	No i-ZnO layer in the buffer
M3690_13	4	2.09	1.41	0.85	No NaF precursor; 5 min. 200 °C anneal
M3652_13	3	1.54	1.12	0.97	No NaF precursor; 5 min. 200 °C anneal

Macroscopic I-V curves from multiple CZTSe cells were obtained by Keithley 4200 with uniform near 1 sun illumination (985 W/m^2), as shown in Fig. 5.1. Due to the series resistance brought by sharp tungsten probes, the fill factors and efficiencies are slightly lower than their datasheet values provided by Dr. Repins. M3602_22 has a buffer layer with the standard CdS/i-ZnO/ZnO:Al stack, while M3599_23 is a standard sample but without the i-ZnO layer in the stack. In the I-V curves of Figs. 5.1 (a) and (b), I_{SC} from M3599_23 is about 1 mA larger than that of M3602_22, but V_{OC} of M3599_23 is 25 mV smaller. By omitting i-ZnO in the buffer layer, one can benefit in current collection at the cost of voltage. Low V_{OC} of CZTS(Se) cell is the primary issue limiting its performance compared to its parent CIGS cell. Lower V_{OC} in the CZTS(Se) device is believed to mainly due to the effect of defects that resulted in increased reverse saturation current [63]. An optimized window and front interface are also expected to minimize recombination, and resistive losses.

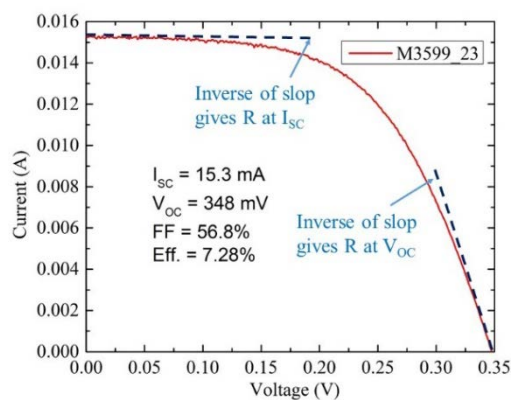
M3690_13 differs from the standard structure in the back contact. It was made without the NaF precursor and the bare CZTSe absorber was treated with 5 minute, 200 °C annealing to oxidize the excess Zn. I_{SC} , V_{OC} and efficiency of M3690_13 are all smaller than those of M3599_23 and M3602_21. Among them, V_{OC} experienced the largest drop, about 30% less than V_{OC} of M3602_22. NaF precursor layer is widely used in CIGS cell and well-known as helpful in enhancing V_{OC} , FF and I_{SC} of the device. For CZTS(Se) devices, sodium is also proved to help improve the performance, yet the mechanism of such enhancement is still not fully understood. Some studies show sodium plays an important role in increasing grain size [217, 218]; some propose that higher carrier concentration and/or mobility can be achieved with sodium [219, 220], and some believe it can passivate deep defects since sodium has been shown mainly increase V_{OC} and fill factors of devices, which are both strongly sensitive to defects and traps [221, 222]. Although all the CZTSe devices in this study are deposited on soda lime glass, a thin layer of NaF in M3602_22 in conjunction with the soda lime glass might increase the out-diffusion of Na thus leading to higher V_{OC} , I_{SC} , FF and efficiency. The absorber thickness of M3690_13 is over 30% thicker than the others. People have been observing higher series resistance with thicker CZTS(Se) absorbers [223, 224]. Inverse of the slope at V_{OC} can help to estimate the series resistance in the device. In Fig. 5.1 (c), the smaller slope of the dash line at V_{OC} suggests a higher series in M3690_13. And the increased series resistance caused by increased absorber thickness may also lead to a reduction in the conversion efficiency, fill factor and short circuit current.

Same with M3690_13, M3652_13 was directly deposited on the substrate without the NaF precursor, and the absorber was treated with 5 minute, 200 °C annealing. One apparent

difference between M3690_13 and M3652_13 is the higher Cu/(Zn+Sn) and lower Zn/Sn ratios in M3652_13 CZTSe film. Cu-poor and Zn-rich is often required for better device performance, though more detailed effects on the CZTSe absorber properties are still unclear. By comparing the I-V curves between the four devices, one can find that the I_{SC} of M3652_13 is substantially reduced by higher Cu/(Zn+Sn) and lower Zn/Sn ratio, only about 66% of the I_{SC} of M36022_22 and 71% of M3690_13. As discussed in Chapter 2, shunt resistance R_{SH} is represented by the inverse slope of the curve at I_{SC} . It is quite obvious in Fig. 5.1 that with a steep slope at I_{SC} , R_{SH} of M3652_13 is much smaller than those of the other cells, thus leading to a lower fill factor and open circuit voltage. Shunt resistance is typically due to manufacturing defects rather than poor solar cell design. In other words, the small shunt resistance of M3652_12 could be largely caused by the defects within the device, and the higher Cu and lower Zn content could be one possible reason that introduce more defects and some other parasitic issues which may be adverse for the cell performance.



(a) M3602_22



(b) M3599_23

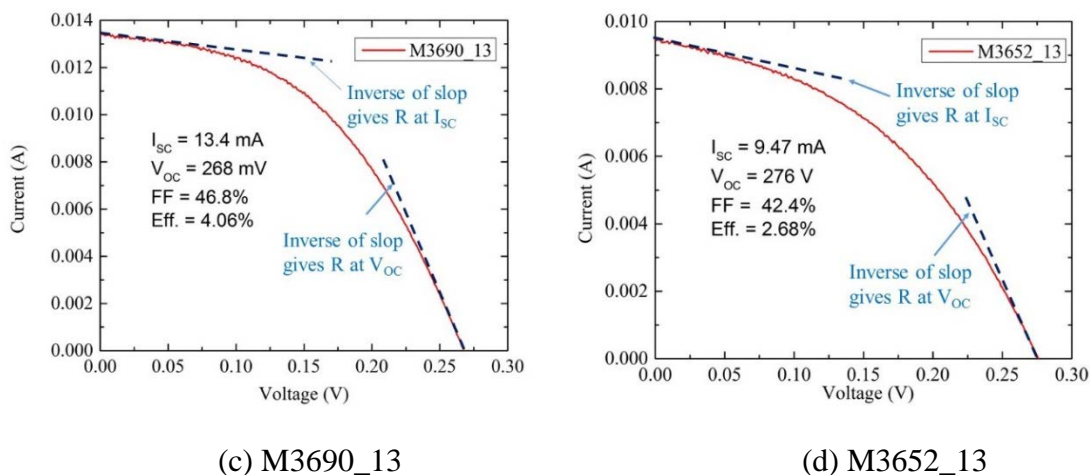


Figure 5.1: Macroscopic I-V curves from different CZTSe solar cells.

5.3. LBIC Comparison of Different CZTSe Solar Cells

Micro-LBIC mappings were performed for the CZTSe solar cell devices M 3602_22, M3599_23, M3690_13 and M3652_13. 532 nm laser at both low ($\sim 2 \mu\text{W}$) and high power ($\sim 179 \mu\text{W}$) levels were used to examine the photo-response in different illumination conditions. Similar with the LBIC mapping results discussed in Chapter 3, at lower power level, all the CZTSe cell generate average EQEs comparable to those of the macroscopic probe.

For M3602_22 with 7.8% efficiency, the average EQE at $\sim 2 \mu\text{W}$ is $84.4\% \pm 0.3\%$. Histogram of the LBIC mapping in Fig. 5.2 (c) shows that the majority part of the mapped region exhibits high EQEs from 80% to 90%. The scattered dark spots with low EQEs in Fig. 5.2 (a) are mostly CdS rich spots. A CdS rich spot highlighted with yellow circle in the low power level LBIC mapping leads to LBIC contrast reversal in the high power level mapping in Fig. 5. 2 (b). The spot position shift was due to sample movement between the

two mappings. Similar with M3599_23 in Chapter 3, M3602_22 also experienced drastically, about 84% EQE droop at high power level illumination.

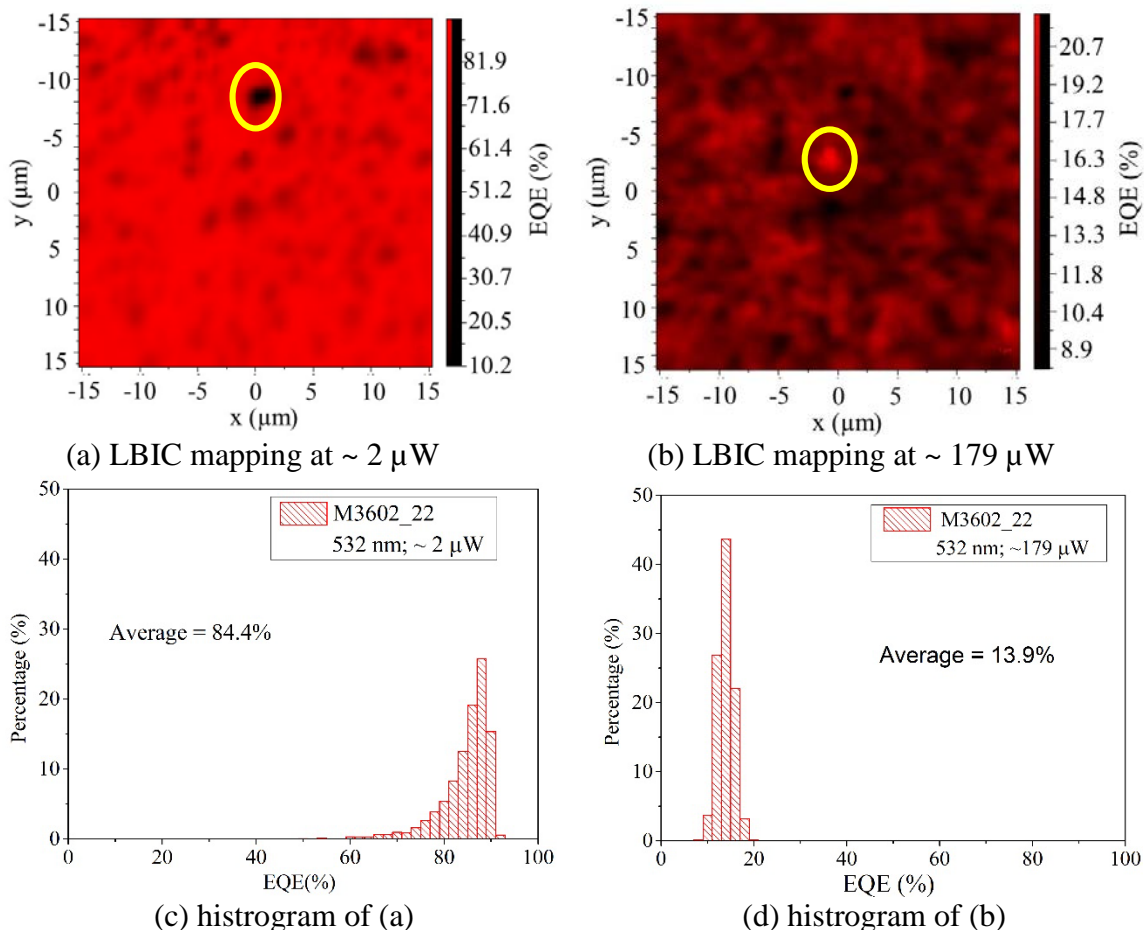


Figure 5.2: M3602_22 LBIC mapping with 532 nm laser at low and high power levels.

In Fig. 5.3, LBIC mappings of M3599_23 were obtained from a region containing only one roughly $2 \mu\text{m}$ -size bright CdS rich spot, and the average EQE from this region is $90.1 \% \pm 0.3\%$ which is 25% larger than the average EQE obtained in Fig. 3.8. Although LBIC mappings in Figs 5.3 and 3.8 were collected from different sub-cells from M3599_23, the two sub-cells shares almost same characteristics such as I_{sc} , V_{oc} , FF and efficiency. With only one very small CdS rich region, the average EQE (90.1%) is very close to the

maximum EQE (92.7%) in Fig. 5.3 (a). Apparently, the mapped region of Fig. 5.3 is overall much more uniform than that of Fig. 3.8. As aforementioned in Chapter 3, an increased energy conversion efficiency is expected without the CdS rich regions when operated under low illumination condition. At high power level illumination, the average EQE of M3599_23 experienced a 72% reduction and the CdS rich spot also led to a LBIC contrast reversal in Fig. 5.3 (b).

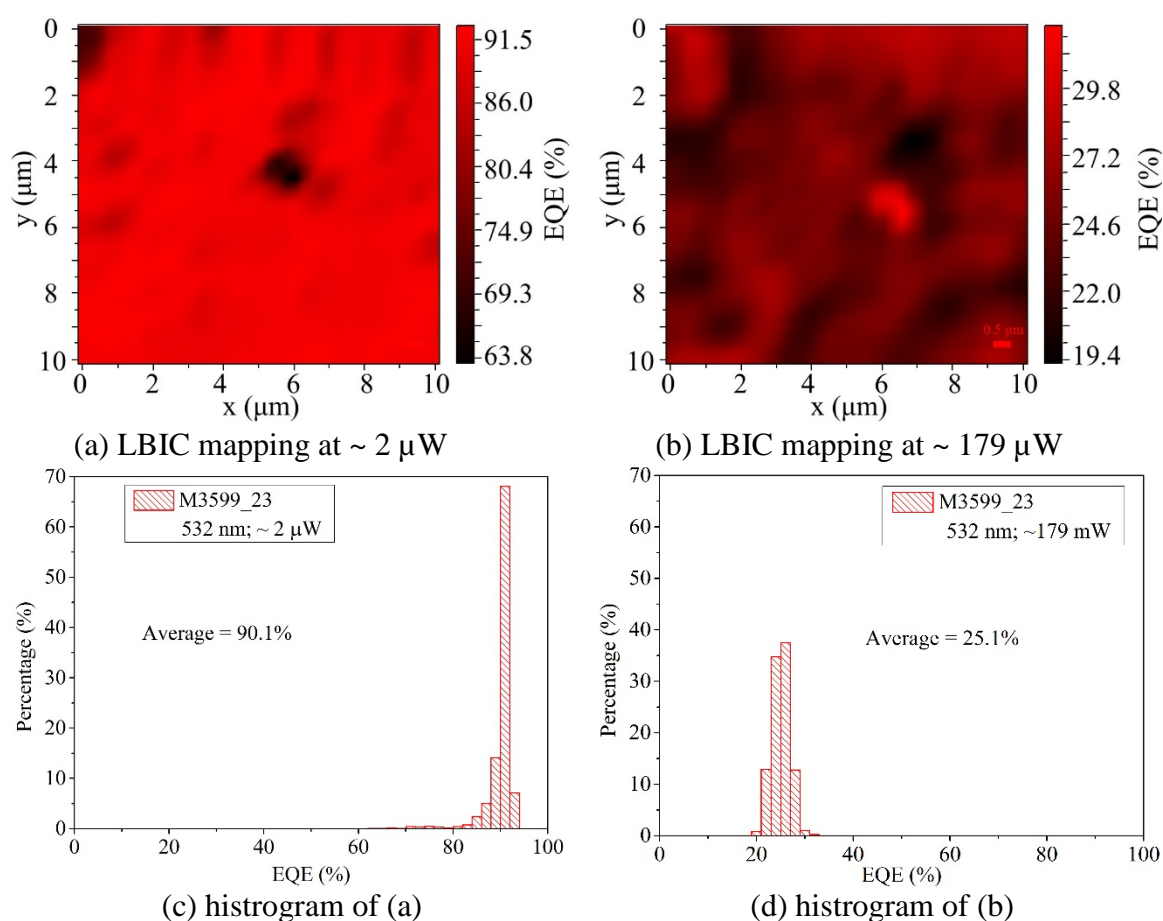


Figure 5.3: M3599_23 LBIC mapping with 532 nm laser at low and high power levels.

Fig. 5.4 shows the LBIC mapping data for M3690_13. M3690_13 has yielded a relatively low EQE at low power level with 532 nm laser. One might notice that the histogram in Fig. 5.4 (c) has a different distribution pattern with those of other samples

tested at low power level: one being more symmetric with respect to the average value, and the others tend to skew left. With a maximum EQE at 74.9%, most regions are generating EQE ranging from 40% to 60%. However, for other CZTSe devices, over 90% of spots could yield EQEs very close to the maximum EQE. When illumination power was increased to $179 \mu\text{W}$, almost all spots of M3690_13 have EQEs from 7% to 8%, while other cells would still have some spread in the histogram. The large spread of EQEs at low laser power illumination indicates huge non uniformity within the film. However, under high power illumination condition, such uniformity effect does not affect the EQE of the device as much as high illumination density, which leads to an almost uniform current distribution in M3690_13.

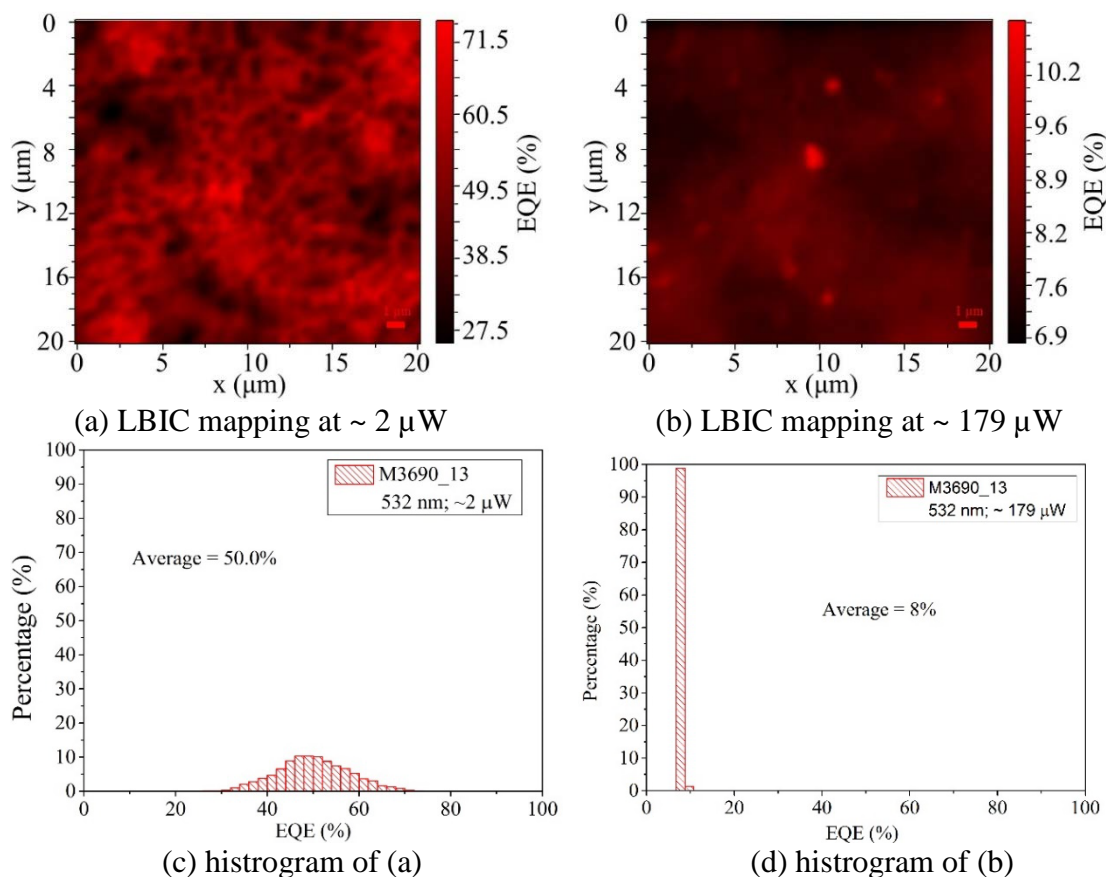


Figure 5.4: M3690_13 LBIC mapping with 532 nm laser at low and high power levels.

With only $\sim 3\%$ cell efficiency, the average EQE of M3652_13 is 58.4%, much smaller than those of M3602_22 and M3599_23 which have higher energy conversion efficiencies. The interesting result comes from the EQEs of M3652_13 at high power level illumination condition. As shown in Fig. 5.5(b), unlike the other cells, at $\sim 179 \mu\text{W}$, the average EQE of M3652_13 is 55.7%, and there is almost no EQE droop compared with the low power level illumination. Different from the phenomenon observed in Chapter 3, no LBIC contrast reversal was observed in Fig. 5.4, when no bright CdS rich region was optically found within the mapped region from M3652_13. Shape of the histogram in Fig. 5.5 (d) at high power is similar with that of the histogram when illuminated at low power level.

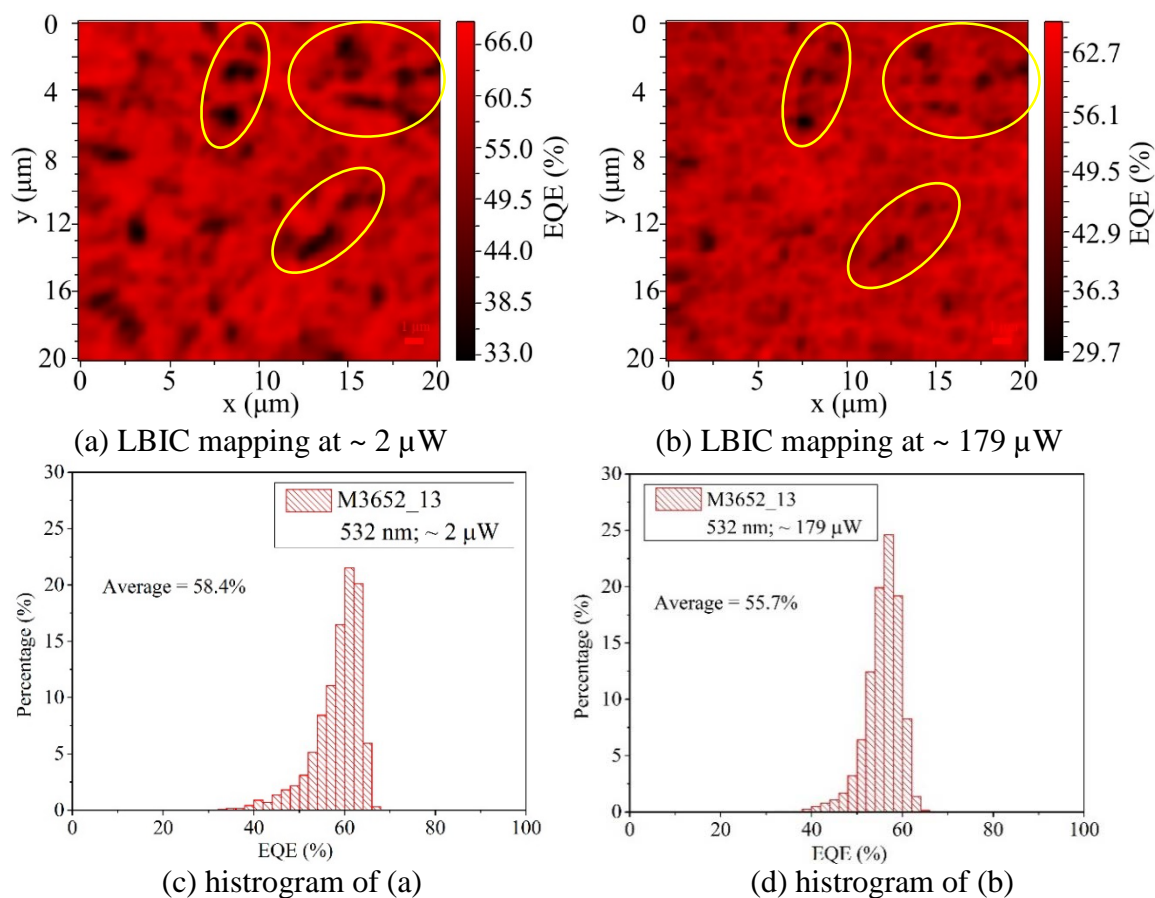


Figure 5.5: M3652_13 LBIC mapping with 532 nm laser at low and high power levels.

Raman spectra of these four CZTSe devices are compared in Fig. 5.6, all obtained from randomly selected general spots with 532 nm laser at $\sim 179 \mu\text{W}$. Main peaks in all spectra are 172 cm^{-1} and 196 cm^{-1} from CZTSe and 303 cm^{-1} from CdS. The peak intensities among the four CZTSe sample are quite similar, although M3602_22 shows the strongest CdS peak. It indicates that there is no significant difference in the CdS layer thickness of the four devices. In other words, it is not the variation in CdS layer thickness that leads to the different EQE droops when illuminated at high power level. One obvious difference between M3652_13 and other CZTSe device is the Cu/(Zn+Sn) and Zn/Sn ratios in the absorber. The differences in the elemental ratios are likely to be the main reason that results in the different illumination density dependence between the devices, because the structure of M3652_13 is similar to the other CZTSe devices in this study and films of the devices were also deposited in a similar way. It has been found empirically that lower Cu/(Zn+Sn) ratio and higher Zn/Sn ratio off the stoichiometric values tend to give rise to better device performance [26, 28, 44, 223]. The theoretical explanation of this empirical observation has been that the Zn-rich and Sn (Cu) poor condition could avoid the formation of Sn_{Zn} and related defect complexes which are expected to be detrimental to the solar cell performance [215]. For M3652_13, lower short circuit current, efficiency and EQE were indeed observed from its macroscopic I-V curve as well as low power illumination LBIC mapping. Therefore, with a higher Cu/(Zn+Sn) ratio and a lower Zn/Sn ratio in M3652_13, one might naturally consider that the low energy conversion efficiency of M3652_13 could be mainly caused by the defect problems associated with the unfavorable high Sn (Cu) and low Zn condition, if one only considers the low illumination density results. However, if we take into account the illumination power density dependence, the answer cannot be so

simple! One normally expects that the adverse effect of the point defects, e.g., Sn_{Zn} , will be at least partially eliminated at high excitation density, because the point defects are relatively easy to be saturated. [177]

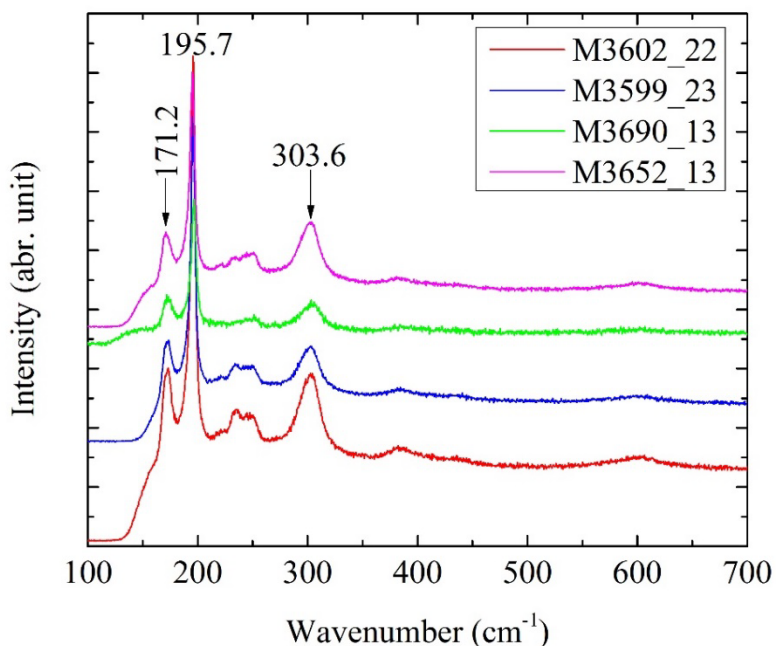


Figure 5.6: Raman spectra of random general spots from multiple CZTSe device surface.

Detailed mechanism for the fast EQE droop in low $\text{Cu}/(\text{Zn}+\text{Sn})$ and high Zn/Sn ratio absorber, but relative stable EQE in high $\text{Cu}/(\text{Zn}+\text{Sn})$ and low Zn/Sn absorber is of great interest, but likely requires major effort to find out. Besides the possible defect mitigation effect invoked in the literature, our finding seems to suggest that changing $\text{Cu}/(\text{Zn}+\text{Sn})$ and Zn/Sn ratios could have another important effect on the device performance, that is, affecting the band alignment of the CZT(S,Se)/CdS heterostructure. CdS/CZTSe is mostly found to have the “spike” like alignment, in which the CBM of CdS is higher than that of CZTSe. As discussed in Chapter 3, type I alignment benefits in V_{OC} but becomes a barrier for carriers moving across the heterojunction. Increasing Zn/Sn ratio is expected to increase

the CBM of CZTSe, which is beneficial for the carrier collection. Thus CZTSe devices with higher Zn/Sn and lower Cu/(Zn+Sn) ratios usually yield better photo-response. However, when illuminated with high power density, raising of the electron Fermi level might lower the electron barrier at the back contact, thus, allowing electrons to leak out through the back contact. Thus, materials with higher Cu and lower Zn content, expected to have higher back electron blocking barrier, could still generate a relatively high EQE at high power illumination, although the initial I_{SC} was lower at low illumination density, because of unfavorable band alignment between CZTSe and CdS.

At the same mapping region, when illuminated with 633 nm laser, the average EQE of M3652_13 is 60.4% at $\sim 0.75 \mu\text{W}$ illumination, and dropped to 40.6% at $\sim 40 \mu\text{W}$. Yellow circles in Fig. 5.7 (a) and (b) compare the same low EQE regions at low power level and at high power level. LBIC contrast reversal was not observed with 633 nm laser, either. Comparing the histograms of LBIC mappings at different laser power levels, one may find that Fig. 5.7 (c) and (d) have similar statistic distributions, and the majority of the spots consistently experienced about 20% EQE drop in absolute value. The EQE droop of M3652_13 at high power level illumination is still much smaller than those of other CZTSe cells, for example, M3599_23 in Fig. 3.9 and M3690_13 in Fig. 5.8.

Even though the average EQE of M3690_13 (8.3%) is smaller than that of M3652_13 (40.6%) at high power level illumination condition at 633 nm, an average EQE 66.1% of M3690_13, exceeds 60.4% of M3652_13 at low power illumination, which is consistent with the results reported in Ref. [25]. It is suggested that a thicker absorber is helpful in effectively absorbing the solar spectrum and reduce recombination at the back contact [20, 34]. But thicker absorber will also cause higher series resistance in the cell, thus an optimal

thickness of the absorber is desired for the best energy production. Again, M3690_13 generates EQEs mostly from 7% to 10% resulting in relatively uniform EQE distribution at high power illumination level.

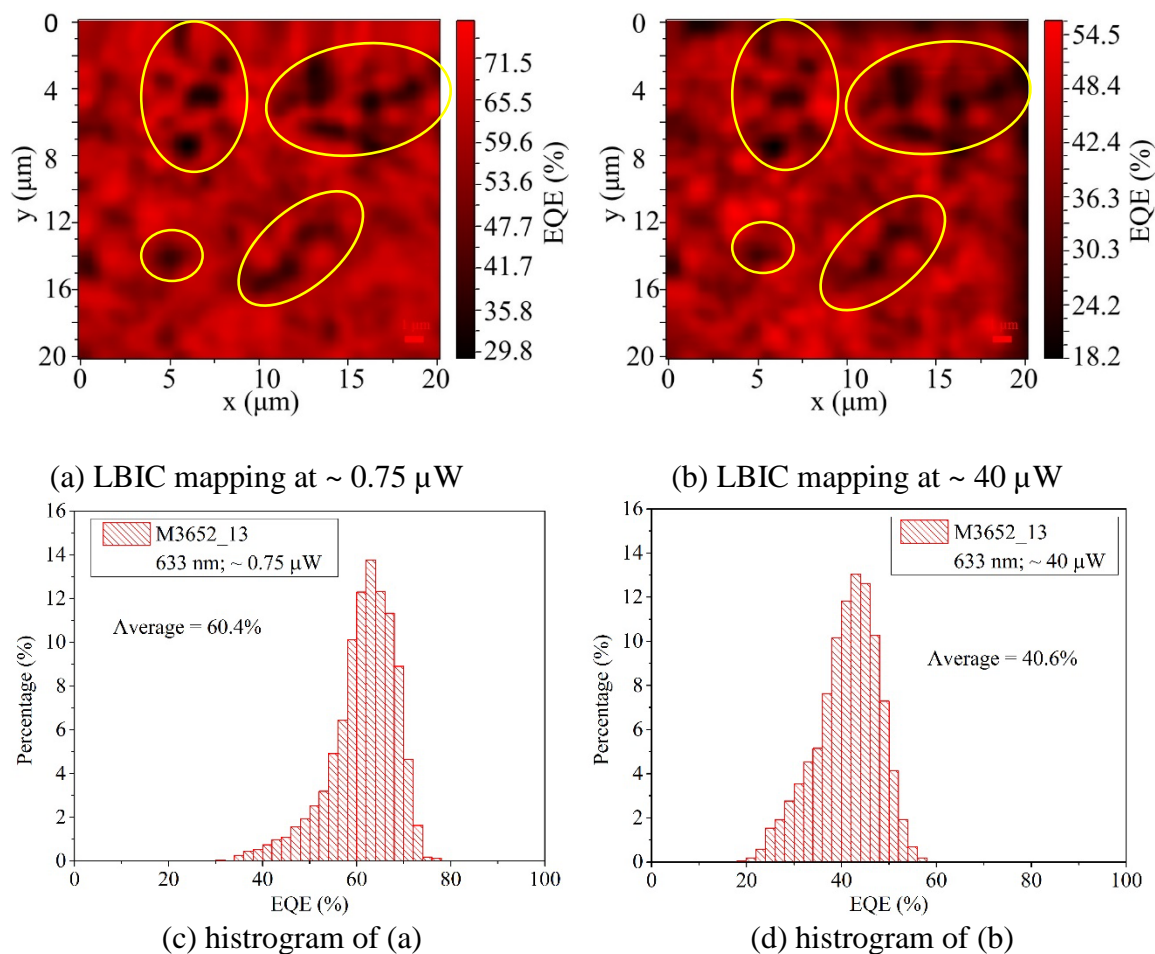


Figure 5.7: M3652_13 LBIC mapping with 633 nm laser at low and high power levels.

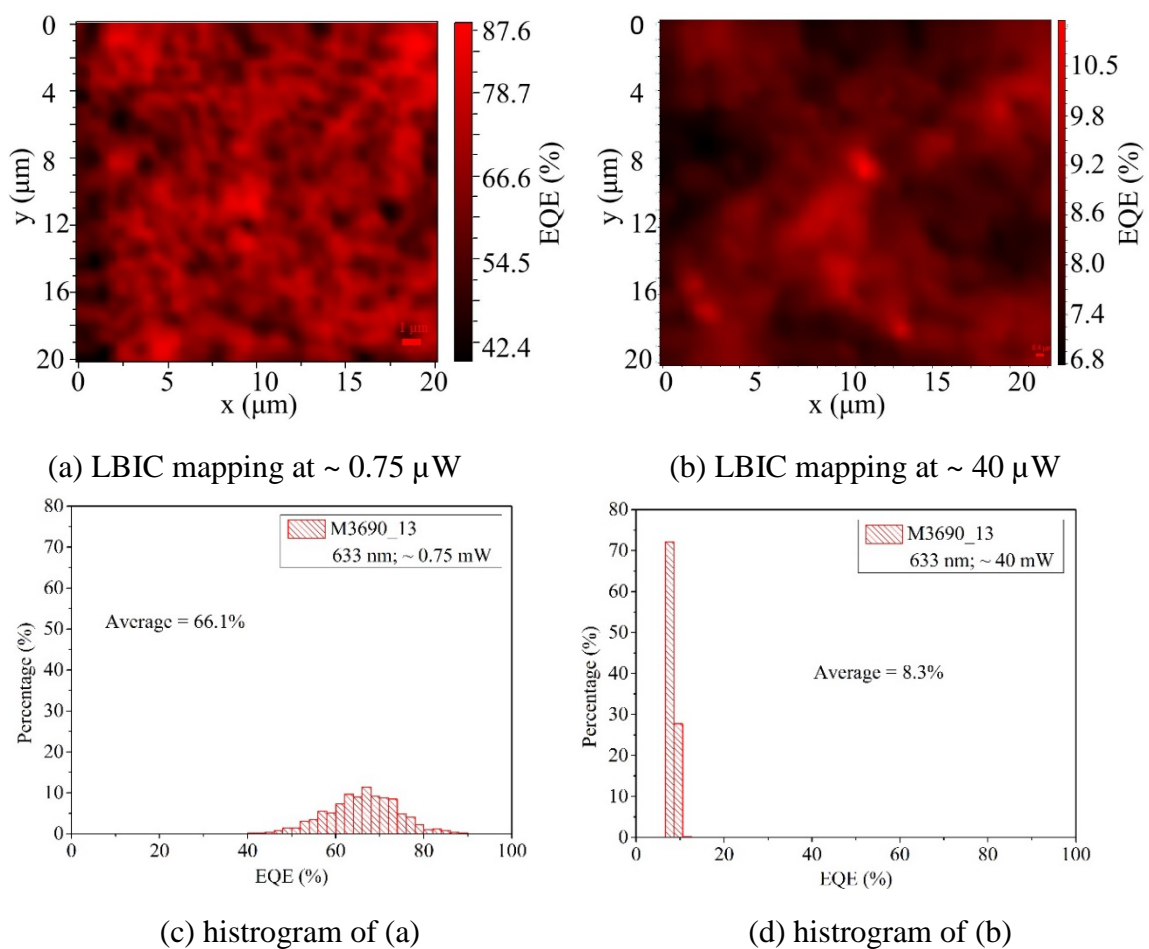
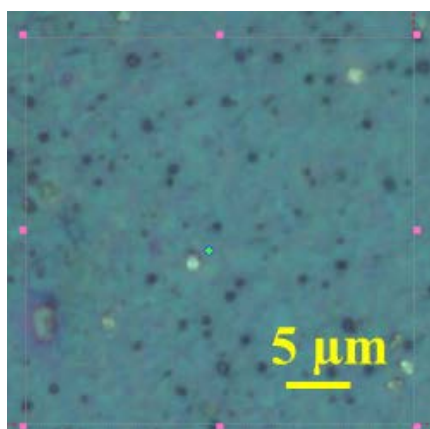


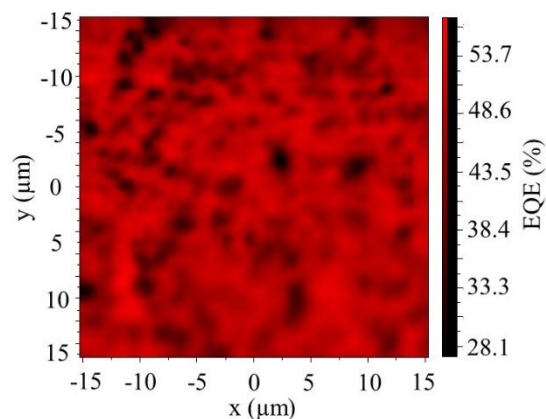
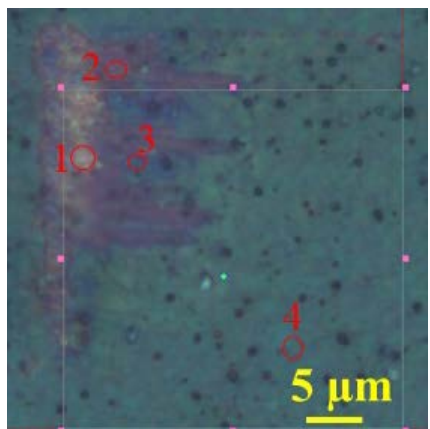
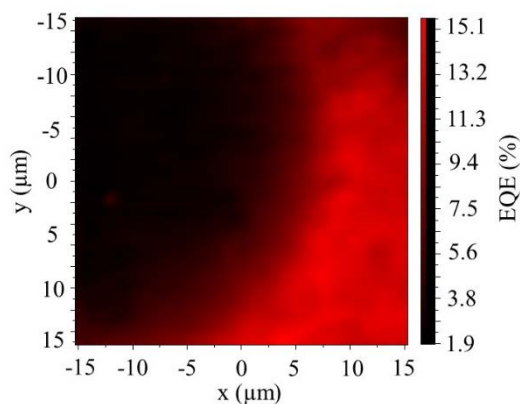
Figure 5.8: M3690_13 LBIC mapping with 633 nm laser at low and high power levels.

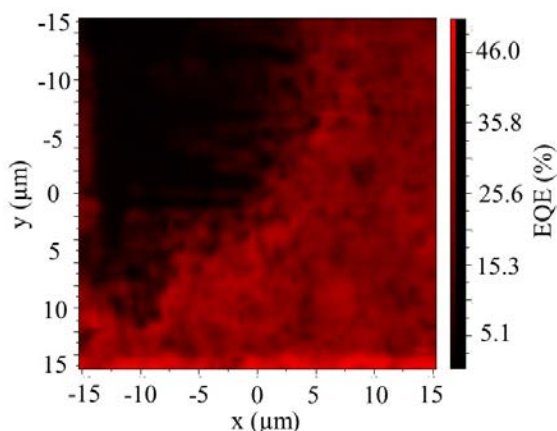
In Fig. 5.9, LBIC mappings from another random region (Fig. 5. 9(a)) of M3652_13 was first illuminated with $\sim 2 \mu\text{W}$ at 532 nm, then with high power $\sim 2.47 \text{ mW}$ at step size of $0.5 \mu\text{m}$. At $\sim 2 \mu\text{W}$, the average EQE is also very low, around 47%. At $\sim 2.47 \text{ mW}$, LBIC mapping of M3652_13 showed large inhomogeneity in Fig. 5.9 (d), with an average of 6.9% and a maximum EQE of 15.6% and minimum of 1.8%. An optical image taken after the 2.47 mW LBIC mapping is shown as Fig. 5.9 (c), where one area (upper left) exhibits apparent color change with the shape and position of the region matching the lower EQE region in Fig. 5. 9 (d). $\sim 2 \mu\text{W}$ LBIC mapping was performed again at the same region,

as shown in Fig. 5.9 (e). The upper left part of the mapping area yields EQE as small as 1%. However, the lower right part still generates EQEs which are comparable to the EQEs of the first $\sim 2 \mu\text{W}$ LBIC mapping. Thus, this part of the absorber was slightly or not affected by the rather high power $\sim 2.47 \text{ mW}$ illumination, while the properties of the left part film was severely changed due to the high power illumination. In Section 4.5, similar LBIC mapping was performed with M3602_21. At $\sim 2.45 \text{ mW}$ illumination, EQE of M3602_21 dropped almost a factor of twenty, and the entire illuminated region could not recover when illuminated by $\sim 2 \mu\text{W}$ again. This comparison suggests that areas similar to the lower right region in Fig. 5.9 (d) on M3652_13 are much more immune to very high illumination density than absorber of M3602_21.



(a) optical image before mapping

(b) LBIC mapping at $\sim 2 \mu\text{W}$ (c) optical image after $\sim 2.47 \text{ mW}$ mapping(d) LBIC mapping at $\sim 2.47 \text{ mW}$



(e) LBIC mapping at $\sim 2 \mu\text{W}$ after 2.47 mW mapping

Figure 5.9: Optical image and LBIC mapping of M3652_12 at $\sim 2 \mu\text{W}$ and $\sim 2.47 \text{ mW}$.

Raman spectroscopy was performed at different spots from the mapping region of M3652_13 to analyze the composition difference between the spots with different colors. Raman spectra at $179 \mu\text{W}$ were collected from four different spots numbered and circled on Fig. 5.9 (c) and one random spot which was not illuminated at laser power higher than $179 \mu\text{W}$ from M365_13 surface. In Fig. 5.10, Raman spectrum from the random spot of M3652_13 is similar to the spectra of other CZTSe cells showed in Chapter 3 and 4. CZTSe peaks are observed around $\sim 172 \text{ cm}^{-1}$, 196 cm^{-1} and 233 cm^{-1} . For a finished device, CdS Raman modes at 303 and 602 cm^{-1} are also observed. Secondary phases are found around $\sim 251 \text{ cm}^{-1}$. However, the spot 1 in Fig. 5.10, which has a color lighter than its original, showed very strong t-Se modes at 238 cm^{-1} , and second and third resonant modes at 477 and 714 cm^{-1} , respectively. The dominant Raman component within spots like spot 1 has become t-Se, which suggests degradation of CZTSe after $\sim 2.47 \text{ mW}$ illumination. For M3602_21, such degradation was observed when CZTSe was illuminated at $\sim 4.5 \text{ mW}$ in Fig. 4.5 (c). For the spot 2, the most significant change was the redshifts of the CZTSe and CdS main peak, line width broadening, and intensity drop caused by heating effect. And

for the spot 3, the mesa like band from 220 to 250 cm^{-1} has become narrower and become a band centered near 238 cm^{-1} , which is similar with what observed from M3602_21 in Fig. 4.4 (c). All the three types of spot experienced EQE droop after ~ 2.45 mW illumination. However, other spots like the spot 4, still yields EQE around 30% to 40% after ~ 2.47 mW illumination. And the Raman spectrum of the spot 4 is very similar with that of the random spot, indicating no structural or compositional change after ~ 2.45 mW illumination. Such different behavior of these spots after ~ 2.47 mW illumination may indicate the large inhomogeneity of thermal conductivity within the film. If the entire device area can be manufactured the same with the regions which are relatively more immune to high power illumination, CZTSe may have a potential in concentrated PV application.

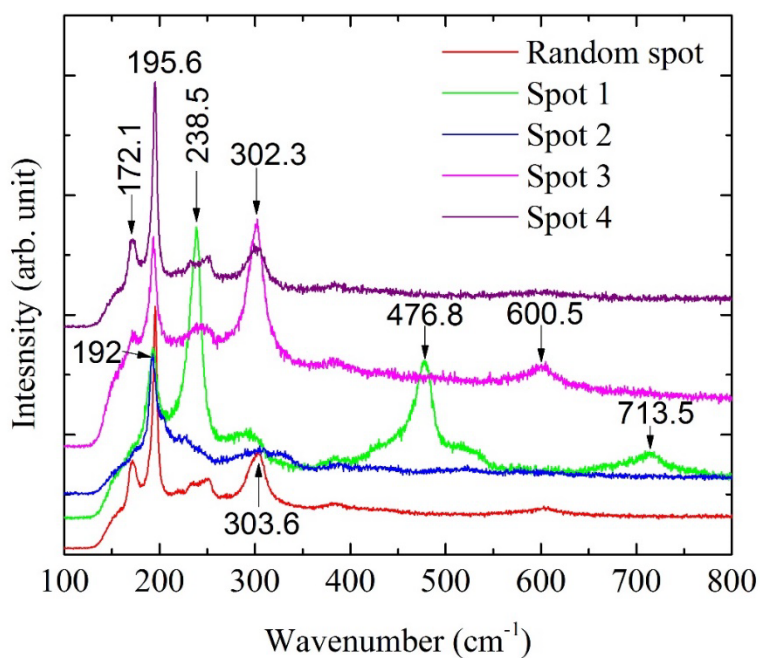


Figure 5.10: Raman spectra comparison of different spots from M3652_13 surface after 2.47 mW LBIC mapping.

5.4. Summary

In this Chapter, the properties of multiple CZTSe solar cell devices with different elemental ratios and device structures are compared. By omitting the i-ZnO layer in the standard CdS/i-ZnO/ZnO:Al buffer stack, one cell can collect more current, but at the cost of lower open circuit voltage. NaF precursor between the substrate and CZTSe absorber is found beneficial for CZTSe cell performance. When deposited CZTSe film directly to SLG/Mo substrate, V_{OC} of the cells are substantially lowered by about 28%. The role that NaF plays in CZTSe solar cell still remains an open question. One possible reason could be that it helps to passivate the defects, thus low V_{OC} is observed without the NaF precursor. With a thicker absorber, M3690_13 also shows a higher series resistance in the device. Together with the missing NaF layer, this cell yields very low V_{OC} , fill factor and efficiency. On the other hand, the absorber layer should be thick enough to effectively absorb the long wavelength lights. M3690_13 is found to generate much higher EQE at 633 nm than at 532 nm. So a balanced absorber layer thickness is expected for excellent device performance.

Elemental ratios within CZTSe film is found to strongly affect the device properties. In general, a Sn/Cu-poor and Zn-rich condition is required for high quality CZTSe solar cells. With a higher Sn/Cu and lower Zn ratio, M3652_12 generates the lowest short circuit current and efficiency. Besides, shunt resistance became a severe issue in this cell which is probably also caused by the higher copper content, since higher Cu may lead to the formation of Cu_xSe_y , which is detrimental for the operation of the solar cell. More research is needed to understand the effect of Sn, Cu and Zn ratios on CZTSe devices. Unlike the other CZTSe cells examined in this study, at high power level illumination, M3652_13 can

still yield EQEs comparable to EQEs at low power level. The EQE droop in M3652_12 is much slower than other cells. Although it generates lower initial EQEs than the other cells, the average EQE exceeds the others when illuminated at high power level. Such phenomenon is different from the CdS thickness effect. Macroscopic thickness of the CdS layer is similar among all the CZTSe cells as deposited. Raman spectra from random general spots reveal close CdS peak intensity from all four CZTSe device. EQEs from different spots change consistently with the illumination condition. The most apparent difference between M3652_13 and other CZTSe cells is in the elemental ratios. Band alignment between CdS and CZTSe also depends on the elemental ratios in the absorber. At lower power level, a lower spike barrier between CdS and CZTSe could be achieved with low Sn/Cn and high Zn content, which is beneficial for current collection. However, at high power level, the increased Fermi level could lead to lowering the electron barrier at the back contact, which makes electron easy to leak out through the back contact. M3652_13 film also exhibits inhomogeneous thermal conductivity, resulting in a non-uniform EQE distribution after high laser power illumination.

CHAPTER 6. CONCLUSIONS AND OUTLOOK

In this work, we emphasize on the integration and correlation of multiple non-destructive spatially resolved techniques to study the optoelectronic properties of thin film solar cell material CZTS(Se). μ -Raman spectroscopy, reviewing the “fingerprints” of the material structures and compositions, was used to analyze the chemistry in CZTS(Se) films. μ -PL was used to estimate the band gap of CZTS(Se) and detect possible defects within the film. μ -LBIC was used to probe the photo-response of CZTS(Se) solar cells in different illumination densities conditions, and to visualize the structural defects and the impact of micro-scale film inhomogeneity at the same time. μ -reflectance offers an more accurate method to estimate the reflectance loss of a rough sample surface, especially to compare the general CZTS(Se) area with the non-uniform regions. Macroscopic I-V curves were plotted to compare the important electrical parameters of different cells as an entire device. And microscopic I-V curves were obtained to compare the photo-response of individual spots. SEM and AFM were used to characterize the surface morphology. Successfully integrating and correlating these techniques was first demonstrated during the course of this work in our laboratory, and this level of integration and correlation has been rare in the field of PV research.

In Chapter 3, an array of such correlated techniques was applied to study the impact of the microscopic-scale thickness inhomogeneity of CdS layer in a CZTSe thin film solar cell. Strong resonant LO and 2LO CdS Raman modes at 303 and 602 cm^{-1} and broad PL

band at 1.73 eV revealed the highest CdS layer concentration at the spots which appear bright in optical image. SEM and AFM images confirmed the surface morphology fluctuation due to CdS layer thickness variation. Thicker CdS regions are found to be substantially more reflective than the general areas thus yield lower EQEs and energy conversion efficiencies than the general area. More interesting results come from the laser power dependence of the LBIC mappings. For both 532 and 633 nm lasers, at low power level, CdS rich regions showed about 50% EQE of the general area. However, at high power level, CdS rich regions are more immune to the EQE droop than the general area, leading to the reversal of LBIC contrast between CdS rich region and general area. Microscopic I-V curves also demonstrated I_{SC} , V_{OC} and efficiency of a CdS rich spot exceeding that of a general spot. These findings on one hand point out the possibility to increase the entire device efficiency by improving the microscopic uniformity of CdS layer, and on the other hand, suggest the potential to fabricate CZTSe and related thin-film solar cells or photo-diodes for concentrated PV and photo-detection. The μ -Raman/PL/reflectance/LBIC in conjunction with SEM and AFM was demonstrated a very useful tool set to examine the effect of inhomogeneity, and to predict the potential for device performance.

In Chapter 4, bare CZTSe film deposited by sputtering, bare CZTSe film and finished CZTSe device deposited by co-evaporation were studied and compared by Raman spectroscopy. CZTSe Raman modes at 172, 196 and 232 cm^{-1} were observed from all three samples, together with secondary phases such as ZnSe, Cu_2SnSe_3 , SnSe and a-Se, which are harmful for PV application of CZTSe films. Structural changes in CZTSe films were observed by high-laser-power Raman spectroscopy. In general, high laser power

illumination brought more changes to sputtered bare film than to the co-evaporated bare film, not only in CZTSe Raman peaks but also in secondary phases, suggesting that the sputtered film is structurally less robust than the co-evaporated film. Strong t-Se Raman lines at ~ 238 and 478 cm^{-1} from the CZTSe device after high power illumination indicates the a-Se existence in the as deposited film and CZTSe decomposition to Se. Surface Raman mappings reveal larger spatial extension of laser heating effect on sputtered film than on co-evaporated ones. These nominally similar films had different responses in structural change to high laser power illumination induced local heating, which suggests different thermal conductivities between films fabricated by different techniques. Least spatial extension was observed in CZTSe device. Extra layers above the absorber might help to improve the thermal conductivity of the structure as a whole.

The cleaved edge Raman spectroscopy reveals the depth profile of the film. Sputtering method tends to form MoSe_2 at the boundaries between substrate and CZTSe absorber. In addition, Mo was found to react with CZTSe at the interface when high laser power is used, generating secondary phases SnSe , ZnSe , Cu_xSe_y and MoSe_2 , whereas Cu_xSe_y , which distributes non-uniformly from the substrate throughout the film thickness, was the dominant secondary phases observed from the cleaved edge of co-evaporated bare film and device. All CZTSe films starts to show decomposition to t-Se at temperature higher than $560 \text{ }^\circ\text{C}$, which confirms that the t-Se is from photo-crystallization of surplus a-Se in the CZTSe layer and CZTSe decomposition caused by heat. When heated to $480 \text{ }^\circ\text{C}$, most CZTSe decomposed, leaving molybdenum oxide, ZnSe and ZnO on the sample surface after returning to room temperature. If heated only to $400 \text{ }^\circ\text{C}$, scattered regions rich in t-Se were found on CZTSe device surface, and other regions can still recover when return to

room temperature. Combination of high-laser-power and high-temperature Raman spectroscopy is shown as a powerful approach to examine the microscopic structural variations of the complex alloys like CZTSe that might otherwise appear to be similar in their simple room temperature Raman spectra and device performance.

In Chapter 5, by analyzing the I-V characteristics of CZTSe cells with different device structures, we were able to evaluate the impact of each layer on solar cell performance. Omitting i-ZnO layer in the window layer stack can benefit in current collection, but at a cost of V_{OC} . An optimized window layer stack is expected to minimize recombination and resistive losses. NaF precursor was found crucial in large V_{OC} of the CZTSe cells. A detailed description of sodium effect on thin film solar cell performance is needed to help better design of sodium content in the device. Thicker absorber layer will result in high series resistance in the solar device, but on the other hand helps to increase the long wavelength absorption. To achieve better efficiency and higher current, a balanced absorber thickness is necessary. Elemental ratios of the CZTSe film can also strongly affect the device photo-response. In general, devices with lower Sn/Cu and higher Zn yield much higher I_{SC} and efficiency than device containing more tin/copper and less zinc. According to the I-V curve, shunt resistance, which is largely caused by defects, became a serious issue in the cell with higher $Cu/(Zn+Sn)$ and lower Zn/Sn ratios. However, the high illumination density induced EQE droop of this cell is much slower than the other cells, and it also showed better thermal conductivity. Elemental ratio may be a possible reason that leads to different EQE droop at high illumination density. Higher Zn/Sn ratio helps to increase the CBM of CZTSe so that the spike at CdS and CZTSe interface may be mitigated. And a lower barrier between CdS and CZTSe is beneficial for carrier collection. However,

when illuminated with high power density, the raised electron Fermi level might lower the electron barrier at the back contact and allow the electrons to leak out through the back contact. Thus devices with higher Zn/Sn ratio experiences faster EQE droop with increasing illumination density. With relatively high EQE at high illumination density and good thermal conductivity, CZTSe films with proper elemental ratios may have the potential to be engineered for the concentrated PV application. Before that, the roles played by each element in film properties such as band gap and defect formation need to be more carefully studied both theoretically and experimentally.

To conclude, because of the achieved high spatial resolution, correlated spatially-resolved techniques, including micro-Raman/PL/LBIC/reflectance/I-V are used to examine the spatial variation of a thin absorber film in terms of chemical composition, photo-response, deposition method, elemental ratio, and device structure dependence. Successfully integrating and correlating these techniques helps to achieve a better understanding of the optical and electrical properties of CZTS(Se)₄. This effort is significant not only for this particular material but also for a wide range of research topics. Applying this approach, in conjunction with high-excitation-power and high-temperature Raman spectroscopy, we have been able to reveal the microscopic scale variations among samples and devices that appeared to be very similar from macroscopic material and device characterizations, and thus serve as a very powerful tool to understand the underlying microscopic material structures and predict the potential of improvement in device performance.

REFERENCES

- [1] C. Wadia, A. P. Alivisatos, and D. M. Kammen, "Materials availability expands the opportunity for large-scale photovoltaics deployment," *Environmental Science & Technology*, vol. 43, pp. 2072-2077, 2009.
- [2] J. P. Holdren, "Science and technology for sustainable well-being," *Science*, vol. 319, pp. 424-434, 2008.
- [3] Wikipedia. Solar Cell. Available: https://en.wikipedia.org/wiki/Solar_cell#History
- [4] M. A. Green, "Thin-film solar cells: review of materials, technologies and commercial status," *Journal of Materials Science: Materials in Electronics*, vol. 18, pp. 15-19, 2007.
- [5] I. Fraunhofer, "Photovoltaics report," Fraunhofer Institute for Solar Energy Systems, www.ise.fraunhofer.de/mwginernal/de5fs23hu73ds/progress, 2013.
- [6] S. K. a. K. Emery. (August 2015). Conversion efficiencies of best research solar cells worldwide from 1976 through 2015 for various photovoltaic technologies. Efficiencies determined by certified agencies/laboratories. Available: [https://commons.wikimedia.org/wiki/File:PVeff\(rev150806\).jpg](https://commons.wikimedia.org/wiki/File:PVeff(rev150806).jpg)
- [7] D. E. Carlson and C. Wronski, "Amorphous silicon solar cell," *Applied Physics Letters*, vol. 28, pp. 671-673, 1976.
- [8] D. Staebler and C. R. Wronski, "Optically induced conductivity changes in discharge-produced hydrogenated amorphous silicon," *Journal of Applied Physics*, vol. 51, pp. 3262-3268, 1980.
- [9] R. G. Dhere, Y. Zhang, M. Romero, S. Asher, M. Young, B. To, et al., "Investigation of junction properties of CdS/CdTe solar cells and their correlation to device properties," in *Photovoltaic Specialists Conference, 2008. PVSC'08. 33rd IEEE*, 2008, pp. 1-5.
- [10] M. Raugei, S. Bargigli, and S. Ulgiati, "Life cycle assessment and energy pay-back time of advanced photovoltaic modules: CdTe and CIS compared to poly-Si," *Energy*, vol. 32, pp. 1310-1318, 2007.
- [11] V. M. Fthenakis, "Life cycle impact analysis of cadmium in CdTe PV production," *Renewable and Sustainable Energy Reviews*, vol. 8, pp. 303-334, 2004.
- [12] J. H. Werner, R. Zapf-Gottwick, M. Koch, and K. Fischer, "Toxic substances in photovoltaic modules," in *Proceedings of the 21st International Photovoltaic Science and Engineering Conference, Fukuoka, Japan, 2011*.

- [13] B. J. Stanbery, "Copper indium selenides and related materials for photovoltaic devices," *Critical reviews in solid state and materials sciences*, vol. 27, pp. 73-117, 2002.
- [14] A. Romeo, M. Terheggen, D. Abou-Ras, D. Batzner, F. Haug, M. Kalin, et al., "Development of thin-film Cu(In,Ga)Se₂ and CdTe solar cells," *Progress in photovoltaics*, vol. 12, pp. 93-112, 2004.
- [15] N. Naghavi, S. Spiering, M. Powalla, B. Cavana, and D. Lincot, "High-efficiency copper indium gallium diselenide (CIGS) solar cells with indium sulfide buffer layers deposited by atomic layer chemical vapor deposition (ALCVD)," *Progress in Photovoltaics: Research and Applications*, vol. 11, pp. 437-443, 2003.
- [16] T. Nakada, M. Mizutani, Y. Hagiwara, and A. Kunioka, "High-efficiency Cu(In, Ga)Se₂ thin-film solar cells with a CBD-ZnS buffer layer," *Solar energy materials and solar cells*, vol. 67, pp. 255-260, 2001.
- [17] C. Platzer-Björkman, T. Törndahl, D. Abou-Ras, J. Malmström, J. Kessler, and L. Stolt, "Zn (O, S) buffer layers by atomic layer deposition in Cu(In,Ga)Se₂ based thin film solar cells: Band alignment and sulfur gradient," *Journal of Applied Physics*, vol. 100, p. 4506, 2006.
- [18] "Rare Earth Elements - Critical Resources for High Technology."
- [19] R. Nitsche, D. Sargent, and P. Wild, "Crystal growth of quaternary 1 2 246 4 chalcogenides by iodine vapor transport," *Journal of Crystal Growth*, vol. 1, pp. 52-53, 1967.
- [20] K. Ito and T. Nakazawa, "Electrical and optical properties of stannite-type quaternary semiconductor thin films," *Japanese Journal of Applied Physics*, vol. 27, p. 2094, 1988.
- [21] W. Shockley and H. J. Queisser, "Detailed balance limit of efficiency of p-n junction solar cells," *Journal of applied physics*, vol. 32, pp. 510-519, 1961.
- [22] H. Katagiri, N. Sasaguchi, S. Hando, S. Hoshino, J. Ohashi, and T. Yokota, "Preparation and evaluation of Cu₂ZnSnS₄ thin films by sulfurization of E-B evaporated precursors," *Solar Energy Materials and Solar Cells*, vol. 49, pp. 407-414, 1997.
- [23] T. M. Friedlmeier, N. Wieser, T. Walter, H. Dittrich, and H. Schock, "Heterojunctions based on Cu₂ZnSnS₄ and Cu₂ZnSnSe₄ thin films," in *14th European PVSEC*, 1997.
- [24] H. Katagiri, K. Jimbo, S. Yamada, T. Kamimura, W. S. Maw, T. Fukano, et al., "Enhanced conversion efficiencies of Cu₂ZnSnS₄-based thin film solar cells by

- using preferential etching technique," *Applied physics express*, vol. 1, p. 041201, 2008.
- [25] Q. Guo, G. M. Ford, W.-C. Yang, B. C. Walker, E. A. Stach, H. W. Hillhouse, et al., "Fabrication of 7.2% efficient CZTSSe solar cells using CZTS nanocrystals," *Journal of the American Chemical Society*, vol. 132, pp. 17384-17386, 2010.
- [26] T. K. Todorov, K. B. Reuter, and D. B. Mitzi, "High-Efficiency Solar Cell with Earth-Abundant Liquid-Processed Absorber," *Advanced materials*, vol. 22, pp. E156-E159, 2010.
- [27] D. A. R. Barkhouse, O. Gunawan, T. Gokmen, T. K. Todorov, and D. B. Mitzi, "Device characteristics of a 10.1% hydrazine-processed $\text{Cu}_2\text{ZnSn}(\text{Se},\text{S})_4$ solar cell," *Progress in Photovoltaics: Research and Applications*, vol. 20, pp. 6-11, 2012.
- [28] W. Wang, M. T. Winkler, O. Gunawan, T. Gokmen, T. K. Todorov, Y. Zhu, et al., "Device Characteristics of CZTSSe Thin-Film Solar Cells with 12.6% Efficiency," *Advanced Energy Materials*, vol. 4, 2014.
- [29] S. Chen, X. Gong, A. Walsh, and S.-H. Wei, "Crystal and electronic band structure of $\text{Cu}_2\text{ZnSnX}_4$ (X= S and Se) photovoltaic absorbers: first-principles insights," *Applied Physics Letters*, vol. 94, p. 41903, 2009.
- [30] J. Paier, R. Asahi, A. Nagoya, and G. Kresse, " $\text{Cu}_2\text{ZnSnS}_4$ as a potential photovoltaic material: a hybrid Hartree-Fock density functional theory study," *Physical Review B*, vol. 79, p. 115126, 2009.
- [31] A. Nagoya, R. Asahi, R. Wahl, and G. Kresse, "Defect formation and phase stability of $\text{Cu}_2\text{ZnSnS}_4$ photovoltaic material," *Physical Review B*, vol. 81, p. 113202, 2010.
- [32] S. Schorr, H.-J. Hoebler, and M. Tovar, "A neutron diffraction study of the stannite-kesterite solid solution series," *European Journal of Mineralogy*, vol. 19, pp. 65-73, 2007.
- [33] S. Schorr, "Structural aspects of adamantine like multinary chalcogenides," *Thin Solid Films*, vol. 515, pp. 5985-5991, 2007.
- [34] J.-S. Seol, S.-Y. Lee, J.-C. Lee, H.-D. Nam, and K.-H. Kim, "Electrical and optical properties of $\text{Cu}_2\text{ZnSnS}_4$ thin films prepared by rf magnetron sputtering process," *Solar Energy Materials and Solar Cells*, vol. 75, pp. 155-162, 2003.
- [35] S. Ahmed, K. B. Reuter, O. Gunawan, L. Guo, L. T. Romankiw, and H. Deligianni, "A high efficiency electrodeposited $\text{Cu}_2\text{ZnSnS}_4$ solar cell," *Advanced Energy Materials*, vol. 2, pp. 253-259, 2012.

- [36] K. Jimbo, R. Kimura, T. Kamimura, S. Yamada, W. S. Maw, H. Araki, et al., "Cu₂ZnSnS₄-type thin film solar cells using abundant materials," *Thin Solid Films*, vol. 515, pp. 5997-5999, 2007.
- [37] S. Pawar, B. Pawar, A. Moholkar, D. Choi, J. Yun, J. Moon, et al., "Single step electrosynthesis of Cu₂ZnSnS₄ (CZTS) thin films for solar cell application," *Electrochimica Acta*, vol. 55, pp. 4057-4061, 2010.
- [38] N. Shinde, D. Dubal, D. Dhawale, C. Lokhande, J. Kim, and J. Moon, "Room temperature novel chemical synthesis of Cu₂ZnSnS₄ (CZTS) absorbing layer for photovoltaic application," *Materials Research Bulletin*, vol. 47, pp. 302-307, 2012.
- [39] G. S. Babu, Y. K. Kumar, P. U. Bhaskar, and S. R. Vanjari, "Effect of Cu/(Zn+ Sn) ratio on the properties of co-evaporated Cu₂ZnSnSe₄ thin films," *Solar Energy Materials and Solar Cells*, vol. 94, pp. 221-226, 2010.
- [40] C. Malerba, F. Biccari, C. L. A. Ricardo, M. Valentini, R. Chierchia, M. Müller, et al., "CZTS stoichiometry effects on the band gap energy," *Journal of Alloys and Compounds*, vol. 582, pp. 528-534, 2014.
- [41] S. W. Shin, S. Pawar, C. Y. Park, J. H. Yun, J.-H. Moon, J. H. Kim, et al., "Studies on Cu₂ZnSnS₄ (CZTS) absorber layer using different stacking orders in precursor thin films," *Solar Energy Materials and Solar Cells*, vol. 95, pp. 3202-3206, 2011.
- [42] M. Altosaar, J. Raudoja, K. Timmo, M. Danilson, M. Grossberg, J. Krustok, et al., "Cu₂Zn_{1-x}Cd_xSn(Se_{1-y}S_y)₄ solid solutions as absorber materials for solar cells," *physica status solidi (a)*, vol. 205, pp. 167-170, 2008.
- [43] M. Grossberg, J. Krustok, K. Timmo, and M. Altosaar, "Radiative recombination in Cu₂ZnSnSe₄ monograins studied by photoluminescence spectroscopy," *Thin Solid Films*, vol. 517, pp. 2489-2492, 2009.
- [44] I. Repins, C. Beall, N. Vora, C. DeHart, D. Kuciauskas, P. Dippo, et al., "Co-evaporated Cu₂ZnSnSe₄ films and devices," *Solar Energy Materials and Solar Cells*, vol. 101, pp. 154-159, 2012.
- [45] F. Luckert, D. Hamilton, M. Yakushev, N. Beattie, G. Zoppi, M. Moynihan, et al., "Optical properties of high quality Cu₂ZnSnSe₄ thin films," *Applied Physics Letters*, vol. 99, p. 062104, 2011.
- [46] H. Matsushita, T. Maeda, A. Katsui, and T. Takizawa, "Thermal analysis and synthesis from the melts of Cu-based quaternary compounds Cu-III-IV-VI₄ and Cu₂-II-IV-VI₄ (II= Zn, Cd; III= Ga, In; IV= Ge, Sn; VI= Se)," *Journal of Crystal Growth*, vol. 208, pp. 416-422, 2000.
- [47] R. A. Wibowo, W. S. Kim, E. S. Lee, B. Munir, and K. H. Kim, "Single step preparation of quaternary Cu₂ZnSnSe₄ thin films by RF magnetron sputtering from

- binary chalcogenide targets," *Journal of Physics and Chemistry of Solids*, vol. 68, pp. 1908-1913, 2007.
- [48] G. S. Babu, Y. K. Kumar, P. U. Bhaskar, and V. S. Raja, "Growth and characterization of co-evaporated $\text{Cu}_2\text{ZnSnSe}_4$ thin films for photovoltaic applications," *Journal of Physics D: Applied Physics*, vol. 41, p. 205305, 2008.
- [49] S. Ahn, S. Jung, J. Gwak, A. Cho, K. Shin, K. Yoon, et al., "Determination of band gap energy (E_g) of $\text{Cu}_2\text{ZnSnSe}_4$ thin films: On the discrepancies of reported band gap values," *Applied Physics Letters*, vol. 97, p. 021905, 2010.
- [50] S. Chen, A. Walsh, J.-H. Yang, X. Gong, L. Sun, P.-X. Yang, et al., "Compositional dependence of structural and electronic properties of $\text{Cu}_2\text{ZnSn}(\text{S}, \text{Se})_4$ alloys for thin film solar cells," *Physical Review B*, vol. 83, p. 125201, 2011.
- [51] J. He, L. Sun, S. Chen, Y. Chen, P. Yang, and J. Chu, "Composition dependence of structure and optical properties of $\text{Cu}_2\text{ZnSn}(\text{S}, \text{Se})_4$ solid solutions: an experimental study," *Journal of Alloys and Compounds*, vol. 511, pp. 129-132, 2012.
- [52] S. W. Shin, J. H. Han, Y. C. Park, G. Agawane, C. H. Jeong, J. H. Yun, et al., "A facile and low-cost synthesis of promising absorber materials on $\text{Cu}_2\text{ZnSn}(\text{S}_x, \text{Se}_{1-x})_4$ nanocrystals consisting of earth abundant elements with tunable band gap characteristics," *Journal of Materials Chemistry*, vol. 22, pp. 21727-21732, 2012.
- [53] M. Grossberg, J. Krustok, J. Raudoja, K. Timmo, M. Altosaar, and T. Raadik, "Photoluminescence and Raman study of $\text{Cu}_2\text{ZnSn}(\text{Se}_x\text{S}_{1-x})_4$ monograins for photovoltaic applications," *Thin Solid Films*, vol. 519, pp. 7403-7406, 2011.
- [54] S. Chen, X. Gong, A. Walsh, and S.-H. Wei, "Defect physics of the kesterite thin-film solar cell absorber $\text{Cu}_2\text{ZnSnS}_4$," *Applied Physics Letters*, vol. 96, p. 021902, 2010.
- [55] A. Walsh, S. Chen, S. H. Wei, and X. G. Gong, "Kesterite Thin-Film Solar Cells: Advances in Materials Modelling of $\text{Cu}_2\text{ZnSnS}_4$," *Advanced Energy Materials*, vol. 2, pp. 400-409, 2012.
- [56] S. Chen, J.-H. Yang, X. Gong, A. Walsh, and S.-H. Wei, "Intrinsic point defects and complexes in the quaternary kesterite semiconductor $\text{Cu}_2\text{ZnSnS}_4$," *Physical Review B*, vol. 81, p. 245204, 2010.
- [57] I. Olekseyuk, I. Dudchak, and L. Piskach, "Phase equilibria in the $\text{Cu}_2\text{S}-\text{ZnS}-\text{SnS}_2$ system," *Journal of alloys and compounds*, vol. 368, pp. 135-143, 2004.
- [58] T. Tanaka, T. Sueishi, K. Saito, Q. Guo, M. Nishio, M. Y. Kin, et al., "Existence and removal of Cu_2Se second phase in coevaporated $\text{Cu}_2\text{ZnSnSe}_4$ thin films," *Journal of Applied Physics*, vol. 111, p. 053522, 2012.

- [59] X. Fontané, L. Calvo-Barrio, V. Izquierdo-Roca, E. Saucedo, A. Pérez-Rodríguez, J. Morante, et al., "In-depth resolved Raman scattering analysis for the identification of secondary phases: characterization of $\text{Cu}_2\text{ZnSnS}_4$ layers for solar cell applications," *Applied Physics Letters*, vol. 98, p. 181905, 2011.
- [60] P. Fernandes, P. Salomé, and A. Da Cunha, "Growth and Raman scattering characterization of $\text{Cu}_2\text{ZnSnS}_4$ thin films," *Thin solid films*, vol. 517, pp. 2519-2523, 2009.
- [61] J. Just, D. Lützenkirchen-Hecht, R. Frahm, S. Schorr, and T. Unold, "Determination of secondary phases in kesterite $\text{Cu}_2\text{ZnSnS}_4$ thin films by x-ray absorption near edge structure analysis," *Applied physics letters*, vol. 99, p. 262105, 2011.
- [62] A. Redinger, K. Hönes, X. Fontané, V. Izquierdo-Roca, E. Saucedo, N. Valle, et al., "Detection of a ZnSe secondary phase in coevaporated $\text{Cu}_2\text{ZnSnSe}_4$ thin films," *Applied Physics Letters*, vol. 98, p. 101907, 2011.
- [63] A. Polizzotti, I. L. Repins, R. Noufi, S.-H. Wei, and D. B. Mitzi, "The state and future prospects of kesterite photovoltaics," *Energy & Environmental Science*, vol. 6, pp. 3171-3182, 2013.
- [64] H. Nozaki, K. Shibata, and N. Ohhashi, "Metallic hole conduction in CuS," *Journal of solid state chemistry*, vol. 91, pp. 306-311, 1991.
- [65] Y. Wu, C. Wadia, W. Ma, B. Sadtler, and A. P. Alivisatos, "Synthesis and photovoltaic application of copper (I) sulfide nanocrystals," *Nano letters*, vol. 8, pp. 2551-2555, 2008.
- [66] A. Sanchez-Juarez and A. Ortiz, "Effects of precursor concentration on the optical and electrical properties of Sn_xS_y thin films prepared by plasma-enhanced chemical vapour deposition," *Semiconductor science and technology*, vol. 17, p. 931, 2002.
- [67] N. Deshpande, A. Sagade, Y. Gudage, C. Lokhande, and R. Sharma, "Growth and characterization of tin disulfide (SnS_2) thin film deposited by successive ionic layer adsorption and reaction (SILAR) technique," *Journal of alloys and compounds*, vol. 436, pp. 421-426, 2007.
- [68] M. Calixto-Rodríguez, H. Martínez, A. Sanchez-Juarez, J. Campos-Alvarez, A. Tiburcio-Silver, and M. Calixto, "Structural, optical, and electrical properties of tin sulfide thin films grown by spray pyrolysis," *Thin Solid Films*, vol. 517, pp. 2497-2499, 2009.
- [69] H. Flammersberger, "Experimental study of $\text{Cu}_2\text{ZnSnS}_4$ thin films for solar cells," 2010.

- [70] D. Denzler, M. Olschewski, and K. Sattler, "Luminescence studies of localized gap states in colloidal ZnS nanocrystals," *Journal of applied physics*, vol. 84, pp. 2841-2845, 1998.
- [71] J. J. Scragg, *Copper Zinc Tin Sulfide Thin Films for Photovoltaics: Synthesis and Characterisation by Electrochemical Methods*: Springer Science & Business Media, 2011.
- [72] J. Hedström, H. Ohlsén, M. Bodegård, A. Kylner, L. Stolt, D. Hariskos, et al., "ZnO/CdS/Cu(In, Ga)Se₂ thin film solar cells with improved performance," in *Photovoltaic Specialists Conference, 1993., Conference Record of the Twenty Third IEEE, 1993*, pp. 364-371.
- [73] Y. Kamikawa-Shimizu, S. Shimada, M. Watanabe, A. Yamada, K. Sakurai, S. Ishizuka, et al., "Effects of Mo back contact thickness on the properties of CIGS solar cells," *physica status solidi (a)*, vol. 206, pp. 1063-1066, 2009.
- [74] L. Assmann, J. Bernede, A. Drici, C. Amory, E. Halgand, and M. Morsli, "Study of the Mo thin films and Mo/CIGS interface properties," *Applied Surface Science*, vol. 246, pp. 159-166, 2005.
- [75] N. Kohara, S. Nishiwaki, Y. Hashimoto, T. Negami, and T. Wada, "Electrical properties of the Cu(In, Ga)Se₂/MoSe₂/Mo structure," *Solar Energy Materials and Solar Cells*, vol. 67, pp. 209-215, 2001.
- [76] D. Abou-Ras, G. Kostorz, D. Bremaud, M. Kälin, F. Kurdesau, A. Tiwari, et al., "Formation and characterisation of MoSe₂ for Cu(In, Ga)Se₂ based solar cells," *Thin Solid Films*, vol. 480, pp. 433-438, 2005.
- [77] J. J. Scragg, J. T. Watjen, M. Edoff, T. Ericson, T. Kubart, and C. Platzer-Björkman, "A detrimental reaction at the molybdenum back contact in Cu₂ZnSn (S, Se)₄ thin-film solar cells," *Journal of the American Chemical Society*, vol. 134, pp. 19330-19333, 2012.
- [78] S. López-Marino, M. Placidi, A. Pérez-Tomás, J. Llobet, V. Izquierdo-Roca, X. Fontané, et al., "Inhibiting the absorber/Mo-back contact decomposition reaction in Cu₂ZnSnSe₄ solar cells: the role of a ZnO intermediate nanolayer," *Journal of Materials Chemistry A*, vol. 1, pp. 8338-8343, 2013.
- [79] J. J. Scragg, T. Kubart, J. T. Wätjen, T. Ericson, M. K. Linnarsson, and C. Platzer-Björkman, "Effects of back contact instability on Cu₂ZnSnS₄ devices and processes," *Chemistry of Materials*, vol. 25, pp. 3162-3171, 2013.
- [80] F. Liu, K. Sun, W. Li, C. Yan, H. Cui, L. Jiang, et al., "Enhancing the Cu₂ZnSnS₄ solar cell efficiency by back contact modification: Inserting a thin TiB₂ intermediate layer at Cu₂ZnSnS₄/Mo interface," *Applied Physics Letters*, vol. 104, p. 051105, 2014.

- [81] D. A. R. Barkhouse, R. Haight, N. Sakai, H. Hiroi, H. Sugimoto, and D. B. Mitzi, "Cd-free buffer layer materials on $\text{Cu}_2\text{ZnSn}(\text{S}_x\text{Se}_{1-x})_4$: Band alignments with ZnO , ZnS , and In_2S_3 ," *Applied Physics Letters*, vol. 100, p. 193904, 2012.
- [82] V. Rajeshmon, N. Poornima, C. S. Kartha, and K. Vijayakumar, "Modification of the optoelectronic properties of sprayed In_2S_3 thin films by indium diffusion for application as buffer layer in CZTS based solar cell," *Journal of Alloys and Compounds*, vol. 553, pp. 239-244, 2013.
- [83] N. Sakai, H. Hiroi, and H. Sugimoto, "Development of Cd-free buffer layer for $\text{Cu}_2\text{ZnSnS}_4$ thin-film solar cells," in *Photovoltaic Specialists Conference (PVSC)*, 2011 37th IEEE, 2011, pp. 003654-003657.
- [84] M. T. Htay, Y. Hashimoto, N. Momose, K. Sasaki, H. Ishiguchi, S. Igarashi, et al., "A cadmium-free $\text{Cu}_2\text{ZnSnS}_4/\text{ZnO}$ heterojunction solar cell prepared by practicable processes," *Japanese Journal of Applied Physics*, vol. 50, p. 032301, 2011.
- [85] Available:
https://en.wikipedia.org/wiki/Copper_indium_gallium_selenide_solar_cells
- [86] K. Ito, *Copper Zinc Tin Sulfide-Based Thin Film Solar Cells*: John Wiley & Sons, 2015.
- [87] H. Katagiri, " $\text{Cu}_2\text{ZnSnS}_4$ thin film solar cells," *Thin Solid Films*, vol. 480, pp. 426-432, 2005.
- [88] T. Kobayashi, K. Jimbo, K. Tsuchida, S. Shinoda, T. Oyanagi, and H. Katagiri, "Investigation of $\text{Cu}_2\text{ZnSnS}_4$ -based thin film solar cells using abundant materials," *Japanese journal of applied physics*, vol. 44, p. 783, 2005.
- [89] H. Araki, Y. Kubo, A. Mikaduki, K. Jimbo, W. S. Maw, H. Katagiri, et al., "Preparation of $\text{Cu}_2\text{ZnSnS}_4$ thin films by sulfurizing electroplated precursors," *Solar Energy Materials and Solar Cells*, vol. 93, pp. 996-999, 2009.
- [90] T. Tanaka, D. Kawasaki, M. Nishio, Q. Guo, and H. Ogawa, "Fabrication of $\text{Cu}_2\text{ZnSnS}_4$ thin films by co-evaporation," *physica status solidi (c)*, vol. 3, pp. 2844-2847, 2006.
- [91] B. Shin, O. Gunawan, Y. Zhu, N. A. Bojarczuk, S. J. Chey, and S. Guha, "Thin film solar cell with 8.4% power conversion efficiency using an earth-abundant $\text{Cu}_2\text{ZnSnS}_4$ absorber," *Progress in Photovoltaics: Research and Applications*, vol. 21, pp. 72-76, 2013.
- [92] W. Xinkun, L. Wei, C. Shuying, L. Yunfeng, and J. Hongjie, "Photoelectric properties of $\text{Cu}_2\text{ZnSnS}_4$ thin films deposited by thermal evaporation," *Journal of Semiconductors*, vol. 33, p. 022002, 2012.

- [93] B. A. Schubert, B. Marsen, S. Cinque, T. Unold, R. Klenk, S. Schorr, et al., "Cu₂ZnSnS₄ thin film solar cells by fast coevaporation," *Progress in Photovoltaics: Research and Applications*, vol. 19, pp. 93-96, 2011.
- [94] A. Weber, H. Krauth, S. Perlt, B. Schubert, I. Kötschau, S. Schorr, et al., "Multi-stage evaporation of Cu₂ZnSnS₄ thin films," *Thin Solid Films*, vol. 517, pp. 2524-2526, 2009.
- [95] T. Tanaka, T. Nagatomo, D. Kawasaki, M. Nishio, Q. Guo, A. Wakahara, et al., "Preparation of Cu₂ZnSnS₄ thin films by hybrid sputtering," *Journal of Physics and Chemistry of Solids*, vol. 66, pp. 1978-1981, 2005.
- [96] J. ZHANG, S. Lexi, F. Yujun, and X. Erqing, "Cu₂ZnSnS₄ thin films prepared by sulfurization of ion beam sputtered precursor and their electrical and optical properties," *Rare Metals*, vol. 25, pp. 315-319, 2006.
- [97] P. Fernandes, P. Salomé, A. Da Cunha, and B.-A. Schubert, "Cu₂ZnSnS₄ solar cells prepared with sulphurized dc-sputtered stacked metallic precursors," *Thin Solid Films*, vol. 519, pp. 7382-7385, 2011.
- [98] F. Liu, Y. Li, K. Zhang, B. Wang, C. Yan, Y. Lai, et al., "In situ growth of Cu₂ZnSnS₄ thin films by reactive magnetron co-sputtering," *Solar Energy Materials and Solar Cells*, vol. 94, pp. 2431-2434, 2010.
- [99] Wikipedia. Available: https://en.wikipedia.org/wiki/Pulsed_laser_deposition
- [100] K. Sekiguchi, K. Tanaka, K. Moriya, and H. Uchiki, "Epitaxial growth of Cu₂ZnSnS₄ thin films by pulsed laser deposition," *physica status solidi (c)*, vol. 3, pp. 2618-2621, 2006.
- [101] A. Moholkar, S. Shinde, G. Agawane, S. Jo, K. Rajpure, P. Patil, et al., "Studies of compositional dependent CZTS thin film solar cells by pulsed laser deposition technique: An attempt to improve the efficiency," *Journal of Alloys and Compounds*, vol. 544, pp. 145-151, 2012.
- [102] A. Moholkar, S. Shinde, A. Babar, K.-U. Sim, H. K. Lee, K. Rajpure, et al., "Synthesis and characterization of Cu₂ZnSnS₄ thin films grown by PLD: solar cells," *Journal of Alloys and Compounds*, vol. 509, pp. 7439-7446, 2011.
- [103] A. Moholkar, S. Shinde, A. Babar, K.-U. Sim, Y.-b. Kwon, K. Rajpure, et al., "Development of CZTS thin films solar cells by pulsed laser deposition: Influence of pulse repetition rate," *Solar Energy*, vol. 85, pp. 1354-1363, 2011.
- [104] J. He, L. Sun, N. Ding, H. Kong, S. Zuo, S. Chen, et al., "Single-step preparation and characterization of Cu₂ZnSn(S_xSe_{1-x})₄ thin films deposited by pulsed laser deposition method," *Journal of Alloys and Compounds*, vol. 529, pp. 34-37, 2012.

- [105] A. Nandur and B. White, "Growth of $\text{Cu}_2\text{ZnSnS}_4$ (CZTS) by Pulsed Laser Deposition for Thin film Photovoltaic Absorber Material," in APS Meeting Abstracts, 2014, p. 24003.
- [106] S. C. Riha, B. A. Parkinson, and A. L. Prieto, "Solution-based synthesis and characterization of $\text{Cu}_2\text{ZnSnS}_4$ nanocrystals," *Journal of the American Chemical Society*, vol. 131, pp. 12054-12055, 2009.
- [107] C. Steinhagen, M. G. Panthani, V. Akhavan, B. Goodfellow, B. Koo, and B. A. Korgel, "Synthesis of $\text{Cu}_2\text{ZnSnS}_4$ nanocrystals for use in low-cost photovoltaics," *Journal of the American Chemical Society*, vol. 131, pp. 12554-12555, 2009.
- [108] Y. Cao, M. S. Denny Jr, J. V. Caspar, W. E. Farneth, Q. Guo, A. S. Ionkin, et al., "High-efficiency solution-processed $\text{Cu}_2\text{ZnSn}(\text{S}, \text{Se})_4$ thin-film solar cells prepared from binary and ternary nanoparticles," *Journal of the American Chemical Society*, vol. 134, pp. 15644-15647, 2012.
- [109] C. K. Miskin, W. C. Yang, C. J. Hages, N. J. Carter, C. S. Joglekar, E. A. Stach, et al., "9.0% efficient $\text{Cu}_2\text{ZnSn}(\text{S}, \text{Se})_4$ solar cells from selenized nanoparticle inks," *Progress in Photovoltaics: Research and Applications*, vol. 23, pp. 654-659, 2015.
- [110] N. Nakayama and K. Ito, "Sprayed films of stannite $\text{Cu}_2\text{ZnSnS}_4$," *Applied Surface Science*, vol. 92, pp. 171-175, 1996.
- [111] G. Larramona, S. Bourdais, A. Jacob, C. Choné, T. Muto, Y. Cuccaro, et al., "8.6% Efficient CZTSSe Solar Cells Sprayed from Water-Ethanol CZTS Colloidal Solutions," *The Journal of Physical Chemistry Letters*, vol. 5, pp. 3763-3767, 2014.
- [112] H. T. Kim, D. Kim, and C. Park, "Temperature Effects on $\text{Cu}_2\text{ZnSnS}_4$ (CZTS) Films Deposited by Spraying Method," *Molecular Crystals and Liquid Crystals*, vol. 564, pp. 155-161, 2012.
- [113] S. Kim and J. Kim, "Effect of selenization on sprayed $\text{Cu}_2\text{ZnSnSe}_4$ thin film solar cell," *Thin Solid Films*, vol. 547, pp. 178-180, 2013.
- [114] V. Rajeshmon, C. S. Kartha, K. Vijayakumar, C. Sanjeeviraja, T. Abe, and Y. Kashiwaba, "Role of precursor solution in controlling the opto-electronic properties of spray pyrolysed $\text{Cu}_2\text{ZnSnS}_4$ thin films," *Solar Energy*, vol. 85, pp. 249-255, 2011.
- [115] Y. Kumar, G. S. Babu, P. U. Bhaskar, and V. S. Raja, "Effect of starting-solution pH on the growth of $\text{Cu}_2\text{ZnSnS}_4$ thin films deposited by spray pyrolysis," *physica status solidi (a)*, vol. 206, pp. 1525-1530, 2009.
- [116] Y. Kumar, P. U. Bhaskar, G. S. Babu, and V. S. Raja, "Effect of copper salt and thiourea concentrations on the formation of $\text{Cu}_2\text{ZnSnS}_4$ thin films by spray pyrolysis," *physica status solidi (a)*, vol. 207, pp. 149-156, 2010.

- [117] V. Rajeshmon and K. Vijayakumar, "Prospects of sprayed CZTS thin film solar cells from the perspective of material characterization and device performance," Cochin University Of Science And Technology, 2013.
- [118] K. Tanaka, N. Moritake, and H. Uchiki, "Preparation of $\text{Cu}_2\text{ZnSnS}_4$ thin films by sulfurizing sol-gel deposited precursors," *Solar Energy Materials and Solar Cells*, vol. 91, pp. 1199-1201, 2007.
- [119] M. Y. Yeh, C. C. Lee, and D. S. Wu, "Influences of synthesizing temperatures on the properties of $\text{Cu}_2\text{ZnSnS}_4$ prepared by sol-gel spin-coated deposition," *Journal of sol-gel science and technology*, vol. 52, pp. 65-68, 2009.
- [120] K. Tanaka, Y. Fukui, N. Moritake, and H. Uchiki, "Chemical composition dependence of morphological and optical properties of $\text{Cu}_2\text{ZnSnS}_4$ thin films deposited by sol-gel sulfurization and $\text{Cu}_2\text{ZnSnS}_4$ thin film solar cell efficiency," *Solar Energy Materials and Solar Cells*, vol. 95, pp. 838-842, 2011.
- [121] K. Maeda, K. Tanaka, Y. Fukui, and H. Uchiki, "Dependence on Annealing Temperature of Properties of $\text{Cu}_2\text{ZnSnS}_4$ Thin Films Prepared by Sol-Gel Sulfurization Method," *Japanese Journal of Applied Physics*, vol. 50, p. 01BE10, 2011.
- [122] S. Kahraman, S. Çetinkaya, M. Podlogar, S. Bernik, H. Çetinkara, and H. Güder, "Effects of the sulfurization temperature on sol gel-processed $\text{Cu}_2\text{ZnSnS}_4$ thin films," *Ceramics International*, vol. 39, pp. 9285-9292, 2013.
- [123] K. Maeda, K. Tanaka, Y. Nakano, and H. Uchiki, "Annealing temperature dependence of properties of $\text{Cu}_2\text{ZnSnS}_4$ thin films prepared by sol-gel sulfurization method," *Japanese Journal of Applied Physics*, vol. 50, p. 05FB08, 2011.
- [124] K. Maeda, K. Tanaka, Y. Fukui, and H. Uchiki, "Influence of H_2S concentration on the properties of $\text{Cu}_2\text{ZnSnS}_4$ thin films and solar cells prepared by sol-gel sulfurization," *Solar Energy Materials and Solar Cells*, vol. 95, pp. 2855-2860, 2011.
- [125] J. J. Scragg, P. J. Dale, and L. M. Peter, "Towards sustainable materials for solar energy conversion: preparation and photoelectrochemical characterization of $\text{Cu}_2\text{ZnSnS}_4$," *Electrochemistry Communications*, vol. 10, pp. 639-642, 2008.
- [126] C. Chan, H. Lam, and C. Surya, "Preparation of $\text{Cu}_2\text{ZnSnS}_4$ films by electrodeposition using ionic liquids," *Solar Energy Materials and Solar Cells*, vol. 94, pp. 207-211, 2010.
- [127] J. O. Jeon, K. D. Lee, L. Seul Oh, S. W. Seo, D. K. Lee, H. Kim, et al., "Highly efficient copper-zinc-tin-selenide (CZTSe) solar cells by electrodeposition," *ChemSusChem*, vol. 7, pp. 1073-1077, 2014.

- [128] W. Liu, B. Guo, C. Mak, A. Li, X. Wu, and F. Zhang, "Facile synthesis of ultrafine $\text{Cu}_2\text{ZnSnS}_4$ nanocrystals by hydrothermal method for use in solar cells," *Thin Solid Films*, vol. 535, pp. 39-43, 2013.
- [129] Z. Zhou, Y. Wang, D. Xu, and Y. Zhang, "Fabrication of $\text{Cu}_2\text{ZnSnS}_4$ screen printed layers for solar cells," *Solar Energy Materials and Solar Cells*, vol. 94, pp. 2042-2045, 2010.
- [130] A. Redinger, D. M. Berg, P. J. Dale, R. Djemour, L. Gütay, T. Eisenbarth, et al., "Route Toward High-Efficiency Single-Phase $\text{Cu}_2\text{ZnSn}(\text{S}, \text{Se})_4$ Thin-Film Solar Cells: Model Experiments and Literature Review," *Photovoltaics, IEEE Journal of*, vol. 1, pp. 200-206, 2011.
- [131] J. J. Scragg, T. Ericson, X. Fontané, V. Izquierdo-Roca, A. Pérez-Rodríguez, T. Kubart, et al., "Rapid annealing of reactively sputtered precursors for $\text{Cu}_2\text{ZnSnS}_4$ solar cells," *Progress in Photovoltaics: Research and Applications*, vol. 22, pp. 10-17, 2014.
- [132] A. Redinger, M. Mousel, R. Djemour, L. Gütay, N. Valle, and S. Siebentritt, " $\text{Cu}_2\text{ZnSnSe}_4$ thin film solar cells produced via co-evaporation and annealing including a SnSe_2 capping layer," *Progress in Photovoltaics: Research and Applications*, vol. 22, pp. 51-57, 2014.
- [133] N. Vora, J. Blackburn, I. Repins, C. Beall, B. To, J. Pankow, et al., "Phase identification and control of thin films deposited by co-evaporation of elemental Cu, Zn, Sn, and Se," *Journal of Vacuum Science & Technology A*, vol. 30, p. 051201, 2012.
- [134] Y. Peter and M. Cardona, *Fundamentals of semiconductors: physics and materials properties*: Springer Science & Business Media, 2010.
- [135] S. R. Systems. Model SR570 Low-Noise Current Preamplifier [Online]. Available: <http://www.thinksrs.com/downloads/PDFs/Manuals/SR570m.pdf>
- [136] Wikidpedia. External Quantum Efficiency. Available: https://en.wikipedia.org/wiki/Quantum_efficiency
- [137] PVEducation. Available: <http://pveducation.org/pvcdrom/solar-cell-operation/quantum-efficiency>
- [138] N. I. Coroperation. Photovoltaic Cell I-V Characterization Theory and LabVIEW Analysis Code. Available: <http://www.ni.com/white-paper/7230/en/>
- [139] Q. Chen and Y. Zhang, "The reversal of the laser-beam-induced-current contrast with varying illumination density in a $\text{Cu}_2\text{ZnSnSe}_4$ thin-film solar cell," *Applied Physics Letters*, vol. 103, p. 242104, 2013.

- [140] R. Naciri, H. Bihri, A. Mzerd, A. Rahioui, M. Abd-Lefdil, and C. Messaoudi, "The role of the CdS buffer layer in the CuInS₂ Thin film solar cell," *Revue des Energies Reneouvelables CER*, vol. 7, pp. 165-168, 2007.
- [141] D. Gal, G. Hodes, D. Hariskos, D. Braunger, and H.-W. Schock, "Size-quantized CdS films in thin film CuInS₂ solar cells," *Applied physics letters*, vol. 73, pp. 3135-3137, 1998.
- [142] R. Caballero, C. A. Kaufmann, M. Cwil, C. Kelch, D. Schweigert, T. Unold, et al., "The role of the CdS buffer layer in CuGaSe₂-based solar cells," *Journal of Physics: Condensed Matter*, vol. 19, p. 356222, 2007.
- [143] K. Nakamura, M. Gotoh, T. Fujihara, T. Toyama, and H. Okamoto, "Influence of CdS window layer on 2- μ m thick CdS/CdTe thin film solar cells," *Solar energy materials and solar cells*, vol. 75, pp. 185-192, 2003.
- [144] B. Korevaar, A. Halverson, J. Cao, J. Choi, C. Collazo-Davila, and W. Huber, "High efficiency CdTe cells using manufacturable window layers and CdTe thickness," *Thin Solid Films*, vol. 535, pp. 229-232, 2013.
- [145] K. Orgassa, U. Rau, Q. Nguyen, H. Werner Schock, and J. H. Werner, "Role of the CdS buffer layer as an active optical element in Cu(In,Ga)Se₂ thin-film solar cells," *Progress in Photovoltaics: Research and Applications*, vol. 10, pp. 457-463, 2002.
- [146] M. Neuschitzer, Y. Sanchez, S. López-Marino, H. Xie, A. Fairbrother, M. Placidi, et al., "Optimization of CdS buffer layer for high-performance Cu₂ZnSnSe₄ solar cells and the effects of light soaking: elimination of crossover and red kink," *Progress in Photovoltaics: Research and Applications*, 2015.
- [147] X. Wu, "High-efficiency polycrystalline CdTe thin-film solar cells," *Solar energy*, vol. 77, pp. 803-814, 2004.
- [148] X. Wu, R. Dhere, Y. Yan, M. Romero, Y. Zhang, J. Zhou, et al., "High-efficiency polycrystalline CdTe thin-film solar cells with an oxygenated amorphous CdS (a-CdS: O) window layer," in *Photovoltaic Specialists Conference, 2002. Conference Record of the Twenty-Ninth IEEE*, 2002, pp. 531-534.
- [149] B. McCandless and S. Hegedus, "Influence of CdS window layers on thin film CdS/CdTe solar cell performance," in *Photovoltaic Specialists Conference, 1991., Conference Record of the Twenty Second IEEE*, 1991, pp. 967-972.
- [150] T. Minemoto, T. Matsui, H. Takakura, Y. Hamakawa, T. Negami, Y. Hashimoto, et al., "Theoretical analysis of the effect of conduction band offset of window/CIS layers on performance of CIS solar cells using device simulation," *Solar Energy Materials and Solar Cells*, vol. 67, pp. 83-88, 2001.

- [151] M. Bär, B.-A. Schubert, B. Marsen, R. G. Wilks, S. Pookpanratana, M. Blum, et al., "Cliff-like conduction band offset and KCN-induced recombination barrier enhancement at the CdS/Cu₂ZnSnS₄ thin-film solar cell heterojunction," *Applied Physics Letters*, vol. 99, p. 222105, 2011.
- [152] S. Zhang, S.-H. Wei, A. Zunger, and H. Katayama-Yoshida, "Defect physics of the CuInSe₂ chalcopyrite semiconductor," *Physical Review B*, vol. 57, p. 9642, 1998.
- [153] T. Kato, H. Hiroi, N. Sakai, H. Sugimoto, E. S. B. Center, and S. S. S. KK, "Buffer/absorber interface study on Cu₂ZnSnS₄ and Cu₂ZnSnSe₄ based solar cells: band alignment and its impact on the solar cell performance," in *Proc. 28th European Solar Energy Conf. and Exhibition*, 2013, p. 2125.
- [154] R. Haight, A. Barkhouse, O. Gunawan, B. Shin, M. Copel, M. Hopstaken, et al., "Band alignment at the Cu₂ZnSn(S_xSe_{1-x})₄/CdS interface," *Applied Physics Letters*, vol. 98, p. 253502, 2011.
- [155] J. Li, M. Wei, Q. Du, W. Liu, G. Jiang, and C. Zhu, "The band alignment at CdS/Cu₂ZnSnSe₄ heterojunction interface," *Surface and Interface Analysis*, vol. 45, pp. 682-684, 2013.
- [156] B. Bob, J. V. Li, C. Beall, J. Carapella, C. DeHart, Y. Yang, et al., "Junction formation and interface effects in CZTSe solar cells," in *Photovoltaic Specialist Conference (PVSC), 2014 IEEE 40th*, 2014, pp. 2299-2303.
- [157] G. Dresselhaus, "Optical Absorption Band Edge in Anisotropic Crystals," *Physical Review*, vol. 105, p. 135, 1957.
- [158] N. Shinde, C. Lokhande, J. Kim, and J. Moon, "Low cost and large area novel chemical synthesis of Cu₂ZnSnS₄ (CZTS) thin films," *Journal of Photochemistry and Photobiology A: Chemistry*, vol. 235, pp. 14-20, 2012.
- [159] J. Leitão, N. Santos, P. Fernandes, P. Salomé, A. da Cunha, J. González, et al., "Study of optical and structural properties of Cu₂ZnSnS₄ thin films," *Thin Solid Films*, vol. 519, pp. 7390-7393, 2011.
- [160] H. Wei, W. Guo, Y. Sun, Z. Yang, and Y. Zhang, "Hot-injection synthesis and characterization of quaternary Cu₂ZnSnSe₄ nanocrystals," *Materials letters*, vol. 64, pp. 1424-1426, 2010.
- [161] Y. Zhang, B. Fluegel, M. Hanna, J. Geisz, L. W. Wang, and A. Mascarenhas, "Effects of heavy nitrogen doping in III-V semiconductors—How well does the conventional wisdom hold for the dilute nitrogen “III-V-N alloys”?," *physica status solidi (b)*, vol. 240, pp. 396-403, 2003.

- [162] M. Himmrich and H. Haeuseler, "Far infrared studies on stannite and wurtzstannite type compounds," *Spectrochimica Acta Part A: Molecular Spectroscopy*, vol. 47, pp. 933-942, 1991.
- [163] M. Dimitrievska, A. Fairbrother, X. Fontané, T. Jawhari, V. Izquierdo-Roca, E. Saucedo, et al., "Multiwavelength excitation Raman scattering study of polycrystalline kesterite $\text{Cu}_2\text{ZnSnS}_4$ thin films," *Applied Physics Letters*, vol. 104, p. 021901, 2014.
- [164] A. Khare, B. Himmetoglu, M. Johnson, D. J. Norris, M. Cococcioni, and E. S. Aydil, "Calculation of the lattice dynamics and Raman spectra of copper zinc tin chalcogenides and comparison to experiments," *Journal of Applied Physics*, vol. 111, p. 083707, 2012.
- [165] G. Surgina, A. Zenkevich, I. Sipaylo, V. Nevolin, W. Drube, P. Teterin, et al., "Reactive pulsed laser deposition of $\text{Cu}_2\text{ZnSnS}_4$ thin films in H_2S ," *Thin Solid Films*, vol. 535, pp. 44-47, 2013.
- [166] R. Caballero, V. Izquierdo-Roca, J. Merino, E. Friedrich, A. Climent-Font, E. Saucedo, et al., " $\text{Cu}_2\text{ZnSnS}_4$ thin films grown by flash evaporation and subsequent annealing in Ar atmosphere," *Thin Solid Films*, vol. 535, pp. 62-66, 2013.
- [167] A. Smith, P. Meek, and W. Liang, "Raman scattering studies of SnS_2 and SnSe_2 ," *Journal of Physics C: Solid State Physics*, vol. 10, p. 1321, 1977.
- [168] I. Klavina, T. Kaljuvee, K. Timmo, J. Raudoja, R. Traksmäa, M. Altosaar, et al., "Study of $\text{Cu}_2\text{ZnSnSe}_4$ monograin formation in molten KI starting from binary chalcogenides," *Thin Solid Films*, vol. 519, pp. 7399-7402, 2011.
- [169] H. Li, B. Wang, and L. Li, "Study on Raman spectra of zinc selenide nanopowders synthesized by hydrothermal method," *Journal of Alloys and Compounds*, vol. 506, pp. 327-330, 2010.
- [170] J. Scott, T. Damen, W. Silfvast, R. Leite, and L. Cheesman, "Resonant Raman scattering in ZnS and ZnSe with the cadmium laser," *Optics Communications*, vol. 1, pp. 397-399, 1970.
- [171] C. Shan, Z. Liu, X. Zhang, C. Wong, and S. Hark, "Wurtzite ZnSe nanowires: growth, photoluminescence, and single-wire Raman properties," *Nanotechnology*, vol. 17, p. 5561, 2006.
- [172] I. Repins, M. A. Contreras, B. Egaas, C. DeHart, J. Scharf, C. L. Perkins, et al., "19.9%-efficient $\text{ZnO}/\text{CdS}/\text{CuInGaSe}_2$ solar cell with 81.2% fill factor," *Progress in Photovoltaics: Research and applications*, vol. 16, pp. 235-239, 2008.
- [173] R. Leite, J. Scott, and T. Damen, "Multiple-phonon resonant Raman scattering in CdS," *Physical Review Letters*, vol. 22, p. 780, 1969.

- [174] J. Aguilar-Hernandez, G. Contreras-Puente, A. Morales-Acevedo, O. Vigil-Galan, F. Cruz-Gandarilla, J. Vidal-Larramendi, et al., "Photoluminescence and structural properties of cadmium sulphide thin films grown by different techniques," *Semiconductor science and technology*, vol. 18, p. 111, 2003.
- [175] A. E. Abken, D. Halliday, and K. Durose, "Photoluminescence study of polycrystalline photovoltaic CdS thin film layers grown by close-spaced sublimation and chemical bath deposition," *Journal of applied physics.*, vol. 105, p. 064515, 2009.
- [176] W.-D. Park, "Photoluminescence of Nanocrystalline CdS Thin Films Prepared by Chemical Bath Deposition," *Transactions on Electrical and Electronic Materials*, vol. 11, pp. 170-173, 2010.
- [177] T. Gfroerer, Y. Zhang, and M. Wanlass, "An extended defect as a sensor for free carrier diffusion in a semiconductor," *Applied Physics Letters*, vol. 102, p. 012114, 2013.
- [178] M. Jiang and X. Yan, *Cu₂ZnSnS₄ thin film solar cells: Present status and future prospects*: INTECH Open Access Publisher, 2013.
- [179] A. Redinger and S. Siebentritt, "Coevaporation of Cu₂ZnSnSe₄ thin films," *Applied Physics Letters*, vol. 97, p. 092111, 2010.
- [180] M. Dimitrievska, A. Fairbrother, E. Saucedo, A. Pérez-Rodríguez, and V. Izquierdo-Roca, "Influence of compositionally induced defects on the vibrational properties of device grade Cu₂ZnSnSe₄ absorbers for kesterite based solar cells," *Applied Physics Letters*, vol. 106, p. 073903, 2015.
- [181] T. Gürel, C. Sevik, and T. Çağın, "Characterization of vibrational and mechanical properties of quaternary compounds Cu₂ZnSnS₄ and Cu₂ZnSnSe₄ in kesterite and stannite structures," *Physical Review B*, vol. 84, p. 205201, 2011.
- [182] N. B. M. Amiri and A. Postnikov, "Electronic structure and lattice dynamics in kesterite-type Cu₂ZnSnSe₄ from first-principles calculations," *Physical Review B*, vol. 82, p. 205204, 2010.
- [183] J. Wang, W. Yao, J. Wang, H. Lu, H. Sun, X. Wang, et al., "Quality of ZnSe/GaAs epilayers studied by spatial correlation model of Raman scattering," *Applied physics letters*, vol. 62, pp. 2845-2847, 1993.
- [184] C.-J. Wang, S.-C. Shei, and S.-J. Chang, "Effect of solvent chelating on crystal growth mechanism of CZTSe nanoink in polyetheramine," 2015.
- [185] V. V. Poborchii, A. V. Kolobov, and K. Tanaka, "An in situ Raman study of polarization-dependent photocrystallization in amorphous selenium films," *Applied physics letters*, vol. 72, p. 1167, 1998.

- [186] K. Yang, Q. Cui, Y. Hou, B. Liu, Q. Zhou, J. Hu, et al., "Pressure-induced crystallization and phase transformation of amorphous selenium: Raman spectroscopy and x-ray diffraction studies," *Journal of Physics: Condensed Matter*, vol. 19, p. 425220, 2007.
- [187] S. Yannopoulos and K. Andrikopoulos, "Raman scattering study on structural and dynamical features of noncrystalline selenium," *The Journal of chemical physics*, vol. 121, pp. 4747-4758, 2004.
- [188] P. Nagels, E. Sleetx, R. Callaerts, and L. Tichy, "Structural and optical properties of amorphous selenium prepared by plasma-enhanced CVD," *Solid state communications*, vol. 94, pp. 49-52, 1995.
- [189] R. Djemour, A. Redinger, M. Mousel, L. Gütay, X. Fontané, V. Izquierdo-Roca, et al., "The three A symmetry Raman modes of kesterite in $\text{Cu}_2\text{ZnSnSe}_4$," *Optics express*, vol. 21, pp. A695-A703, 2013.
- [190] T. Sekine, M. Izumi, T. Nakashizu, K. Uchinokura, and E. Matsuura, "Raman scattering and infrared reflectance in 2H-MoSe_2 ," *Journal of the Physical Society of Japan*, vol. 49, pp. 1069-1077, 1980.
- [191] K.-H. Kim and I. Amal, "Growth of $\text{Cu}_2\text{ZnSnSe}_4$ thin films by selenization of sputtered single-layered Cu-Zn-Sn metallic precursors from a Cu-Zn-Sn alloy target," *Electronic Materials Letters*, vol. 7, pp. 225-230, 2011.
- [192] X. Lin, J. Kavalakkatt, A. Ennaoui, and M. C. Lux-Steiner, " $\text{Cu}_2\text{ZnSn}(\text{S},\text{Se})_4$ thin film absorbers based on ZnS, SnS and Cu_3SnS_4 nanoparticle inks: Enhanced solar cells performance by using a two-step annealing process," *Solar Energy Materials and Solar Cells*, vol. 132, pp. 221-229, 2015.
- [193] M. Ishii, K. Shibata, and H. Nozaki, "Anion Distributions and Phase Transitions in $\text{CuS}_{1-x}\text{Se}_x$ ($x= 0-1$) Studied by Raman Spectroscopy," *Journal of Solid State Chemistry*, vol. 105, pp. 504-511, 1993.
- [194] B. Minceva-Sukarova, M. Najdoski, I. Grozdanov, and C. Chunnillall, "Raman spectra of thin solid films of some metal sulfides," *Journal of Molecular Structure*, vol. 410, pp. 267-270, 1997.
- [195] C. M. Fella, A. R. Uhl, C. Hammond, I. Hermans, Y. E. Romanyuk, and A. N. Tiwari, "Formation mechanism of $\text{Cu}_2\text{ZnSnSe}_4$ absorber layers during selenization of solution deposited metal precursors," *Journal of Alloys and Compounds*, vol. 567, pp. 102-106, 2013.
- [196] V. V. Poborchii, A. V. Kolobov, J. Caro, V. V. Zhuravlev, and K. Tanaka, "Polarized Raman spectra of selenium species confined in nanochannels of AlPO_4 -5 single crystals," *Chemical physics letters*, vol. 280, pp. 17-23, 1997.

- [197] A. Postnikov and N. B. M. Amiri, "Ab initio Phonons in Kesterite and Stannite-Type $\text{Cu}_2\text{ZnSnSe}_4$," *Japanese Journal of Applied Physics*, vol. 50, p. 05FE04, 2011.
- [198] J. van Embden, A. S. Chesman, E. Della Gaspera, N. W. Duffy, S. E. Watkins, and J. J. Jasieniak, " $\text{Cu}_2\text{ZnSnS}_{4x}\text{Se}_{4(1-x)}$ Solar Cells from Polar Nanocrystal Inks," *Journal of the American Chemical Society*, vol. 136, pp. 5237-5240, 2014.
- [199] R. Juškėnas, S. Kanapeckaitė, V. Karpavičienė, Z. Mockus, V. Pakštas, A. Selskienė, et al., "A two-step approach for electrochemical deposition of Cu–Zn–Sn and Se precursors for CZTSe solar cells," *Solar Energy Materials and Solar Cells*, vol. 101, pp. 277-282, 2012.
- [200] D. Mead and J. Irwin, "Raman spectra of SnS_2 and SnSe_2 ," *Solid State Communications*, vol. 20, pp. 885-887, 1976.
- [201] M. Kauk-Kuusik, M. Altosaar, K. Muska, M. Pilvet, J. Raudoja, K. Timmo, et al., "Post-growth annealing effect on the performance of $\text{Cu}_2\text{ZnSnSe}_4$ monograin layer solar cells," *Thin Solid Films*, vol. 535, pp. 18-21, 2013.
- [202] I. Leinemann, W. Zhang, T. Kaljuvee, K. Tõnsuaadu, R. Traksmaa, J. Raudoja, et al., " $\text{Cu}_2\text{ZnSnSe}_4$ formation and reaction enthalpies in molten NaI starting from binary chalcogenides," *Journal of Thermal Analysis and Calorimetry*, vol. 118, pp. 1313-1321, 2014.
- [203] Y. Jiang, X.-M. Meng, W.-C. Yiu, J. Liu, J.-X. Ding, C.-S. Lee, et al., "Zinc selenide nanoribbons and nanowires," *The Journal of Physical Chemistry B*, vol. 108, pp. 2784-2787, 2004.
- [204] B. Geng, Q. Du, X. Liu, J. Ma, X. Wei, and L. Zhang, "One-step synthesis and enhanced blue emission of carbon-encapsulated single-crystalline ZnSe nanoparticles," *Applied physics letters*, vol. 89, p. 033115, 2006.
- [205] G. Perna, M. Lastella, M. Ambrico, and V. Capozzi, "Temperature dependence of the optical properties of ZnSe films deposited on quartz substrate," *Applied Physics A*, vol. 83, pp. 127-130, 2006.
- [206] P. Salomé, P. Fernandes, and A. da Cunha, "Morphological and structural characterization of $\text{Cu}_2\text{ZnSnSe}_4$ thin films grown by selenization of elemental precursor layers," *Thin Solid Films*, vol. 517, pp. 2531-2534, 2009.
- [207] M. Dieterle and G. Mestl, "Raman spectroscopy of molybdenum oxides Part II. Resonance Raman spectroscopic characterization of the molybdenum oxides Mo_4O_{11} and MoO_2 ," *Physical Chemistry Chemical Physics*, vol. 4, pp. 822-826, 2002.

- [208] J. J. Scragg, P. J. Dale, D. Colombara, and L. M. Peter, "Thermodynamic Aspects of the Synthesis of Thin-Film Materials for Solar Cells," *ChemPhysChem*, vol. 13, pp. 3035-3046, 2012.
- [209] S. M. Peiris, T. T. Pearson, and D. L. Heinz, "Compression of klockmannite, CuSe," *The Journal of chemical physics*, vol. 109, pp. 634-636, 1998.
- [210] C. Jiang, W. Zhang, G. Zou, W. Yu, and Y. Qian, "Synthesis and characterization of ZnSe hollow nanospheres via a hydrothermal route," *Nanotechnology*, vol. 16, p. 551, 2005.
- [211] K. A. Alim, V. A. Fonoberov, M. Shamsa, and A. A. Balandin, "Micro-Raman investigation of optical phonons in ZnO nanocrystals," *Journal of Applied Physics*, vol. 97, pp. 124313-124313, 2005.
- [212] T. C. Damen, S. Porto, and B. Tell, "Raman effect in zinc oxide," *Physical Review*, vol. 142, p. 570, 1966.
- [213] T. Tanaka, A. Yoshida, D. Saiki, K. Saito, Q. Guo, M. Nishio, et al., "Influence of composition ratio on properties of Cu₂ZnSnS₄ thin films fabricated by co-evaporation," *Thin Solid Films*, vol. 518, pp. S29-S33, 2010.
- [214] W.-C. Hsu, I. Repins, C. Beall, C. DeHart, G. Teeter, B. To, et al., "The effect of Zn excess on kesterite solar cells," *Solar Energy Materials and Solar Cells*, vol. 113, pp. 160-164, 2013.
- [215] S. Chen, L.-W. Wang, A. Walsh, X. Gong, and S.-H. Wei, "Abundance of CuZn+ SnZn and 2CuZn+ SnZn defect clusters in kesterite solar cells," *Applied Physics Letters*, vol. 101, p. 223901, 2012.
- [216] M. Tsega and D.-H. Kuo, "Defects and its effects on properties of Cu-deficient Cu₂ZnSnSe₄ bulks with different Zn/Sn ratios," *Applied Physics Express*, vol. 5, p. 091201, 2012.
- [217] C. Wrasman, "Investigating the effect of Sodium and Potassium on the formation of Copper Zinc Tin Sulfide Films," 2015.
- [218] W. H. Oo, J. Johnson, A. Bhatia, E. Lund, M. Nowell, and M. Scarpulla, "Grain size and texture of Cu₂ZnSnS₄ thin films synthesized by cosputtering binary sulfides and annealing: effects of processing conditions and sodium," *Journal of electronic materials*, vol. 40, pp. 2214-2221, 2011.
- [219] A. Nagaoka, H. Miyake, T. Taniyama, K. Kakimoto, Y. Nose, M. A. Scarpulla, et al., "Effects of sodium on electrical properties in Cu₂ZnSnS₄ single crystal," *Applied Physics Letters*, vol. 104, p. 152101, 2014.

- [220] T. Prabhakar and N. Jampana, "Effect of sodium diffusion on the structural and electrical properties of $\text{Cu}_2\text{ZnSnS}_4$ thin films," *Solar Energy Materials and Solar Cells*, vol. 95, pp. 1001-1004, 2011.
- [221] T. Gershon, Y. S. Lee, R. Mankad, O. Gunawan, T. Gokmen, D. Bishop, et al., "The impact of sodium on the sub-bandgap states in CZTSe and CZTS," *Applied Physics Letters*, vol. 106, p. 123905, 2015.
- [222] Y.-R. Lin, V. Tunuguntla, S.-Y. Wei, W.-C. Chen, D. Wong, C.-H. Lai, et al., "Bifacial sodium-incorporated treatments: Tailoring deep traps and enhancing carrier transport properties in $\text{Cu}_2\text{ZnSnS}_4$ solar cells," *Nano Energy*, vol. 16, pp. 438-445, 2015.
- [223] H. Katagiri, K. Jimbo, W. S. Maw, K. Oishi, M. Yamazaki, H. Araki, et al., "Development of CZTS-based thin film solar cells," *Thin Solid Films*, vol. 517, pp. 2455-2460, 2009.
- [224] X. Xin, M. He, W. Han, J. Jung, and Z. Lin, "Low-Cost Copper Zinc Tin Sulfide Counter Electrodes for High-Efficiency Dye-Sensitized Solar Cells," *Angewandte Chemie International Edition*, vol. 50, pp. 11739-11742, 2011.